

①

AFIT/GEO/ENG/93M-03
AD-A262 596



Characterization of Laboratory Generated Turbulence

by Optical Phase Measurements

THESIS

Eric Parker Magee
Captain, USAF

AFIT/GEO/ENG/93M-03

S DTIC
ELECTE
APR 05 1993
E D

Reproduced From
Best Available Copy

93-06902
 174p8

Approved for public release; distribution unlimited.

98 4 02 061

20001006136

AFIT/GEO/ENG/93M-03

Characterization of Laboratory Generated Turbulence

by

Optical Phase Measurements

THESIS

Presented to the Faculty of the School of Engineering

of the Air Force Institute of Technology

Air University

In Partial Fulfillment of the

Requirements for the Degree of

Master of Science in Electrical Engineering

Eric Parker Magee, B.S.E

Captain, USAF

23 March 1993

DTIC QUALITY INSPECTED 4

Accession For	
NTIS	CRA&I <input checked="" type="checkbox"/>
DTIC	TAB <input type="checkbox"/>
Unannounced <input type="checkbox"/>	
Justification	
By	
Distribution /	
Availability Codes	
Dist	Avail and / or Special
A-1	

Approved for public release; distribution unlimited.

Acknowledgements

I would like to take this opportunity to thank first of all my wife, Caryn, for her understanding during my thesis research. Knowing that she was there for me after the many long nights was an inspiration. I would also like to thank my advisor, Dr. Byron Welsh, for his guidance, and Mr. Thomas Baudendistel for the time he dedicated to hardware design projects. Finally, a heartfelt thanks to my parents for raising me to believe that anything can be accomplished if you give it your all.

Eric Parker Magee

Table of Contents

	Page
Acknowledgements	ii
List of Figures	viii
List of Tables	xiii
Abstract	xiv
 I. Introduction	 1-1
1.1 Scope	1-4
 II. Background	 2-1
2.1 Current Theory	2-1
2.1.1 Frequency response of imaging systems.	2-1
2.1.2 Atmospheric turbulence.	2-3
2.1.3 Average OTF of the atmosphere.	2-5
2.2 Past work	2-7
2.2.1 Temperature structure function.	2-8
2.2.2 Mean square phase fluctuations.	2-9
2.3 Problem	2-11
 III. Experimental Setup and Procedures	 3-1
3.1 Shearing interferometer	3-2
3.2 Turbulence generator	3-8
3.3 Experimental Setup	3-9
3.4 Experimental Procedures	3-10
3.4.1 Common terms.	3-10
3.4.2 Noise characterization.	3-11
3.4.3 Calculation of the phase structure function.	3-12

	Page
IV. Results	4-1
4.1 Noise characterization results	4-1
4.2 Phase structure function results	4-3
4.2.1 Isotropy.	4-6
4.2.2 Homogeneity.	4-10
4.2.3 Inertial subrange.	4-15
4.2.4 Dependence of \hat{D}_s on temperature and wind speed.	4-17
4.3 Observations	4-18
V. Conclusions	5-1
Appendix A. Shearing Interferometer	A-1
A.1 Introduction to the lateral shearing interferometer	A-1
A.2 Theory of lateral shearing interferometer.	A-3
A.3 Description of the SI used in the experiment	A-6
A.4 Alignment and calibration	A-8
Appendix B. Software Users Manual	B-1
B.1 DATA SECTION	B-2
B.1.1 Mode: (current data mode).	B-2
B.1.2 Group: (current data group).	B-3
B.1.3 Frame	B-3
B.1.4 Back	B-4
B.2 REFERENCE SECTION	B-4
B.2.1 Mode	B-4
B.2.2 Group	B-4
B.2.3 Frame	B-4
B.2.4 Source	B-5
B.3 ACQUIRE SECTION	B-5

	Page
B.3.1 Acquire	B-5
B.3.2 Mode	B-5
B.3.3 Analyze	B-6
B.3.4 Display	B-7
B.4 ANALYZE SECTION	B-7
B.4.1 ANALYZE >	B-7
B.5 ARCHIVE SECTION	B-7
B.5.1 ARCHIVE >	B-7
B.6 CALIBRATE SECTION	B-7
B.6.1 CALIBRATE >	B-7
B.7 DISPLAY SECTION	B-7
B.7.1 DISPLAY >	B-7
B.8 BACKGROUND MENU	B-8
B.8.1 Mode	B-8
B.8.2 Group	B-8
B.8.3 Frame	B-8
B.8.4 Source	B-8
B.8.5 ACQUIRE	B-8
B.8.6 Mode	B-8
B.8.7 Save Data Background	B-9
B.9 ANALYSIS MENU	B-9
B.9.1 DATA SECTION	B-9
B.9.2 Analyze	B-9
B.9.3 Mode	B-9
B.9.4 UnWrap	B-9
B.9.5 Recon	B-10
B.9.6 Repeat	B-10

	Page
B.9.7 Screen	B-10
B.9.8 Gain Source	B-10
B.9.9 Shear Source	B-10
B.9.10 Shift Source	B-11
B.10 ARCHIVE MENU	B-11
B.10.1 Load Tape	B-11
B.10.2 View Tape	B-11
B.10.3 Save Data	B-11
B.10.4 Restore Data	B-11
B.10.5 Delete Disk	B-12
B.10.6 Create Tape	B-12
B.11 CALIBRATION MENU	B-12
B.11.1 ALIGNMENT SECTION	B-12
B.11.2 DATA SECTION	B-13
B.11.3 CAMERA GAIN SECTION	B-13
B.11.4 SHEAR MEASUREMENT SECTION	B-15
B.12 DISPLAY MENU	B-16
B.12.1 DATA SECTION	B-16
B.12.2 REFERENCE SECTION	B-17
B.12.3 SINGLE SECTION	B-17
B.12.4 SINGLE DELTA SECTION	B-18
B.12.5 GROUP SECTION	B-18
B.12.6 GROUP DELTA SECTION	B-19
B.12.7 IMAGES SECTION	B-19
B.12.8 OTHER SECTION	B-20
B.13 SET UP MENU	B-21
B.13.1 REMOVE CURVE FROM PHASE	B-21

	Page
B.13.2 REMOVE CURVE FROM SLOPES	B-21
B.13.3 SHOW BORDERS ON MAPS	B-21
B.13.4 ADD TILT TO INTERFEROGRAMS	B-21
B.13.5 1: X-Tilt:	B-22
B.13.6 1: Y-Tilt:	B-22
B.13.7 2: X-Tilt:	B-22
B.13.8 2: Y-Tilt:	B-22
B.14 EXAMPLE	B-22
B.14.1 Calibration	B-22
B.14.2 Acquisition	B-24
B.14.3 Analysis	B-26
Appendix C. Turbulence Chamber Design Drawings	C-1
Appendix D. Additional Phase Structure Function Plots	D-1
Bibliography	BIB-1
Vita	VITA-1

List of Figures

Figure	Page
2.1. Example OTF Plots.	2-7
2.2. Turbulence generator used by Majumdar.	2-9
2.3. Turbulence generator used by Carnevale	2-10
3.1. Block diagram of the experimental setup used.	3-1
3.2. Shearing Interferometer.	3-2
3.3. Method of producing lateral shear.	3-3
3.4. Overlap fringes in a Shearing Interferometer.	3-3
3.5. Raw interference patterns for focus.	3-5
3.6. Cross sections of Raw interference images.	3-5
3.7. X-Tilt map.	3-6
3.8. Y-Tilt map.	3-6
3.9. Phase map.	3-7
3.10. Interference patterns.	3-7
3.11. Turbulence Generator diagrams.	3-8
3.12. Experimental setup used.	3-9
3.13. Template used to determine number of vectors within the aperture.	3-13
3.14. Functional dependence of D_s for homogeneous and isotropic turbulence	3-15
4.1. Delta phase for 2146, frame 0	4-2
4.2. Delta phase for 2146, frame 234	4-2
4.3. Histogram of the phase variations induced by measurement noise.	4-3
4.4. Delta phase for 2092, frame 0.	4-5
4.5. Delta phase for 2092, frame 234.	4-5
4.6. $\hat{D}_s(r)$ for 2042, location 6	4-8
4.7. $\hat{D}_s(r)$ for 2116, location 6	4-8

Figure	Page
4.8. $\hat{D}_s(r)$ for 2114, location 6	4-9
4.9. $\hat{D}_s(r)$ for 2092, location 6	4-9
4.10. $\hat{D}_s(r)$ for 2092, locations 0 - 5	4-11
4.11. $\hat{D}_s(r)$ for 2092, locations 7 - 12	4-12
4.12. $\hat{D}_s(r)$ for 2042	4-13
4.13. $\hat{D}_s(r)$ for 2116	4-13
4.14. $\hat{D}_s(r)$ for 2114	4-14
4.15. $\hat{D}_s(r)$ for 2092	4-14
4.16. $\hat{D}_s(r)$ for 2042	4-16
4.17. Histogram of the phase variations induced by turbulence for group 2042, location 6	4-17
4.18. Index structure constant, C_n^2 , versus average temperature within the chamber.	4-18
 A.1. Types of Shearing Interferometers.	 A-1
A.2. Overlap fringes in a Shearing Interferometer.	A-3
A.3. Hexflash method.	A-5
A.4. Shearing Interferometer.	A-7
A.5. Method of producing lateral shear.	A-8
A.6. Schematic of camera interfaces.	A-9
 C.1. Part A, Fan Mount.	 C-2
C.2. Part B, Top and Bottom.	C-3
C.3. Part C, End Cover.	C-4
C.4. Part D, Heater Element Mount.	C-5
C.5. Parts E & F, Filter Guides and Front Support.	C-6
C.6. Part G, Side Cover.	C-7
C.7. Turbulence Chamber Front View.	C-8
C.8. Turbulence Chamber Side View.	C-9
 D.1. $\hat{D}_s(r)$ for 2050, location 6	 D-1

Figure	Page
D.2. $\hat{D}_s(r)$ for 2108, location 6	D-2
D.3. $\hat{D}_s(r)$ for 2086, location 6	D-2
D.4. $\hat{D}_s(r)$ for 2100, location 6	D-3
D.5. $\hat{D}_s(r)$ for 2112, location 6	D-3
D.6. $\hat{D}_s(r)$ for 2068, location 6	D-4
D.7. $\hat{D}_s(r)$ for 2080, location 6	D-4
D.8. $\hat{D}_s(r)$ for 2122, location 6	D-5
D.9. $\hat{D}_s(r)$ for 2124, location 6	D-5
D.10. $\hat{D}_s(r)$ for 2128, location 6	D-6
D.11. $\hat{D}_s(r)$ for 2132, location 6	D-6
D.12. $\hat{D}_s(r)$ for 2138, location 6	D-7
D.13. $\hat{D}_s(r)$ for 2042, locations 0 - 5	D-8
D.14. $\hat{D}_s(r)$ for 2042, locations 7 - 12	D-9
D.15. $\hat{D}_s(r)$ for 2050, locations 0 - 5	D-10
D.16. $\hat{D}_s(r)$ for 2050, locations 7 - 12	D-11
D.17. $\hat{D}_s(r)$ for 2114, locations 0 - 5	D-12
D.18. $\hat{D}_s(r)$ for 2114, locations 7 - 12	D-13
D.19. $\hat{D}_s(r)$ for 2108, locations 0 - 5	D-14
D.20. $\hat{D}_s(r)$ for 2108, locations 7 - 12	D-15
D.21. $\hat{D}_s(r)$ for 2086, locations 0 - 5	D-16
D.22. $\hat{D}_s(r)$ for 2086, locations 7 - 12	D-17
D.23. $\hat{D}_s(r)$ for 2100, locations 0 - 5	D-18
D.24. $\hat{D}_s(r)$ for 2100, locations 7 - 12	D-19
D.25. $\hat{D}_s(r)$ for 2116, locations 0 - 5	D-20
D.26. $\hat{D}_s(r)$ for 2116, locations 7 - 12	D-21
D.27. $\hat{D}_s(r)$ for 2112, locations 0 - 5	D-22
D.28. $\hat{D}_s(r)$ for 2112, locations 7 - 12	D-23

Figure	Page
D.29. $\hat{D}_s(r)$ for 2068, locations 0 - 5	D-24
D.30. $\hat{D}_s(r)$ for 2068, locations 7 - 12	D-25
D.31. $\hat{D}_s(r)$ for 2080, locations 0 - 5	D-26
D.32. $\hat{D}_s(r)$ for 2080, locations 7 - 12	D-27
D.33. $\hat{D}_s(r)$ for 2122, locations 0 - 5	D-28
D.34. $\hat{D}_s(r)$ for 2122, locations 7 - 12	D-29
D.35. $\hat{D}_s(r)$ for 2124, locations 0 - 5	D-30
D.36. $\hat{D}_s(r)$ for 2124, locations 7 - 12	D-31
D.37. $\hat{D}_s(r)$ for 2128, locations 0 - 5	D-32
D.38. $\hat{D}_s(r)$ for 2128, locations 7 - 12	D-33
D.39. $\hat{D}_c(r)$ for 2132, locations 0 - 5	D-34
D.40. $\hat{D}_s(r)$ for 2132, locations 7 - 12	D-35
D.41. $\hat{D}_s(r)$ for 2138, locations 0 - 5	D-36
D.42. $\hat{D}_s(r)$ for 2138, locations 7 - 12	D-37
D.43. $\hat{D}_s(r)$ for 2050	D-38
D.44. $\hat{D}_s(r)$ for 2108	D-38
D.45. $\hat{D}_s(r)$ for 2086	D-39
D.46. $\hat{D}_s(r)$ for 2100	D-39
D.47. $\hat{D}_s(r)$ for 2112	D-40
D.48. $\hat{D}_s(r)$ for 2068	D-40
D.49. $\hat{D}_s(r)$ for 2080	D-41
D.50. $\hat{D}_s(r)$ for 2122	D-41
D.51. $\hat{D}_s(r)$ for 2124	D-42
D.52. $\hat{D}_s(r)$ for 2128	D-42
D.53. $\hat{D}_s(r)$ for 2132	D-43
D.54. $\hat{D}_s(r)$ for 2138	D-43
D.55. $\hat{D}_s(r)$ for 2050	D-44

Figure	Page
D.56. $\hat{D}_s(\tau)$ for 2114	D-44
D.57. $\hat{D}_s(\tau)$ for 2108	D-45
D.53. $\hat{D}_s(\tau)$ for 2086	D-45
D.59. $\hat{D}_s(\tau)$ for 2092	D-46
D.60. $\hat{D}_s(\tau)$ for 2100	D-46
D.61. $\hat{D}_s(\tau)$ for 2116	D-47
D.62. $\hat{D}_s(\tau)$ for 2112	D-47
D.63. $\hat{D}_s(\tau)$ for 2068	D-48
D.64. $\hat{D}_s(\tau)$ for 2080	D-48
D.65. $\hat{D}_s(\tau)$ for 2122	D-49
D.66. $\hat{D}_s(\tau)$ for 2124	D-49
D.67. $\hat{D}_s(\tau)$ for 2128	D-50
D.68. $\hat{D}_s(\tau)$ for 2132	D-50
D.69. $\hat{D}_s(\tau)$ for 2138	D-51

List of Tables

Table	Page
4.1. Test Matrix.	4-4
4.2. Test Results	4-16
C.1. Turbulence Chamber Parts List.	C-1

Abstract

The resolution achieved by an optical imaging system in the presence of the random effects of the atmosphere is severely degraded from the theoretical diffraction limit. Techniques exist for recovering near diffraction limited performance of an imaging system in the presence of atmospheric turbulence. These image enhancement techniques include speckle imaging, deconvolution, and adaptive optics. A turbulence generator is needed to test these current, as well as future adaptive optics and image enhancement techniques. Current turbulence generators used to simulate atmospheric turbulence have been characterized by measuring characteristics of the turbulence, such as temperature. The effects of the generated turbulence on optical propagation must then be inferred from the measured characteristics.

As opposed to laboratory testing, testing image enhancement techniques in the Earth's atmosphere imposes many limitations. In the atmosphere there is no control over meteorological conditions. Unfavorable weather conditions could result in the loss of time and money invested in conducting the experiment. With a properly characterized turbulence generator, with statistics that match those of the atmosphere, experimental testing of image enhancement techniques can be conducted in a controlled laboratory environment.

A turbulence chamber has been designed and built for laboratory testing of current and future adaptive optics and image enhancement techniques. The turbulence is produced within a chamber consisting of two small fans and a heating element. A unique method of characterizing the statistics of the turbulence has been developed. The effects of the generated turbulence on optical propagation are directly measured by sensing the perturbed wavefront phase subjected to the turbulence. The wavefront phases are measured using a shearing interferometer. The statistical properties of the turbulence are then characterized by estimating the phase structure function from the wavefront phase measurements. The phase structure function is a measure of the correlation

of the phase between two points in a plane perpendicular to the direction of propagation. It has been found that the estimate of the phase structure function depends only on the magnitude of the separation between the spatially separated points, $r = |\vec{r}_1 - \vec{r}_2|$, and follows the Kolmogorov $r^{5/3}$ power law.

REPORT DOCUMENTATION PAGE			Form Approved OMB No. 0704-0188	
<small>Public reporting burden for this collection of information is estimated to average 1 hour per response, including the time for reviewing instructions, searching existing data sources, gathering and maintaining the data needed, and completing and reviewing the collection of information. Send comments regarding this burden estimate or any other aspect of the collection of information, including suggestions for reducing this burden, to: Washington Headquarters Services, Directorate for Information Operations and Reports, 1215 Jefferson Davis Highway, Suite 1204, Arlington, VA 22202-4302, and to the Office of Management and Budget, Paperwork Reduction Project (0704-0188), Washington, DC 20503.</small>				
1. AGENCY USE ONLY (Leave blank)	2. REPORT DATE March 1993	3. REPORT TYPE AND DATES COVERED Master's Thesis		
4. TITLE AND SUBTITLE CHARACTERIZATION OF LABORATORY GENERATED TURBULENCE BY OPTICAL PHASE MEASUREMENTS		5. FUNDING NUMBERS		
6. AUTHOR(S) Captain Eric P. Magee, USAF				
7. PERFORMING ORGANIZATION NAME(S) AND ADDRESS(ES) Air Force Institute of Technology, WPAFB OH 45433-6583		8. PERFORMING ORGANIZATION REPORT NUMBER AFIT/GEO/ENG/93M-03		
9. SPONSORING / MONITORING AGENCY NAME(S) AND ADDRESS(ES)		10. SPONSORING / MONITORING AGENCY REPORT NUMBER		
11. SUPPLEMENTARY NOTES				
12a. DISTRIBUTION / AVAILABILITY STATEMENT Approved for public release; distribution unlimited		12b. DISTRIBUTION CODE		
13. ABSTRACT (Maximum 200 words) The resolution achieved by an optical imaging system in the presence of the random effects of the atmosphere severely degraded from the theoretical diffraction limit. Techniques exist for recovering near diffraction limit performance of an imaging system in the presence of atmospheric turbulence. As opposed to laboratory testing, testing image enhancement techniques in the Earth's atmosphere imposes many limitations. Unfavorable weather conditions could result in the loss of time and money invested in conducting the experiments. With a properly characterized turbulence generator, with statistics that match those of the atmosphere, experimental testing, image enhancement techniques can be conducted in a controlled laboratory environment. A turbulence chamber has been designed and built for laboratory testing of current and future adaptive optics and image enhancement techniques. The turbulence is produced within a chamber consisting of two small fans and a heating element. A unique method of characterizing the statistics of the turbulence has been developed. The wavefront phase perturbations are measured using a shearing interferometer. The statistical properties of the turbulence are characterized by estimating the phase structure function from the wavefront phase measurements. The phase structure function is a measure of the correlation of the phase between two points in a plane perpendicular to the direction of propagation. It has been found that the estimate of the phase structure function depends only on the magnitude of the separation between the spatially separated points, $r = \vec{r}_1 - \vec{r}_2 $, and follows the Kolmogorov $r^{5/3}$ power law.				
14. SUBJECT TERMS Atmospheric Optics, Adaptive Optics, Atmospheric Turbulence, Laboratory Generated Turbulence, Shearing Interferometer, Phase Structure Function			15. NUMBER OF PAGES 172	
			16. PRICE CODE	
17. SECURITY CLASSIFICATION OF REPORT UNCLASSIFIED	18. SECURITY CLASSIFICATION OF THIS PAGE UNCLASSIFIED	19. SECURITY CLASSIFICATION OF ABSTRACT UNCLASSIFIED	20. LIMITATION OF ABSTRACT UL	

GENERAL INSTRUCTIONS FOR COMPLETING SF 298

The Report Documentation Page (RDP) is used in announcing and cataloging reports. It is important that this information be consistent with the rest of the report, particularly the cover and title page. Instructions for filling in each block of the form follow. It is important to *stay within the lines* to meet optical scanning requirements.

Block 1. Agency Use Only (Leave blank)

Block 2. Report Date. Full publication date including day, month, and year, if available (e.g. 1 Jan 88). Must cite at least the year.

Block 3. Type of Report and Dates Covered. State whether report is interim, final, etc. If applicable, enter inclusive report dates (e.g. 10 Jun 87 - 30 Jun 88).

Block 4. Title and Subtitle. A title is taken from the part of the report that provides the most meaningful and complete information. When a report is prepared in more than one volume, repeat the primary title, add volume number, and include subtitle for the specific volume. On classified documents enter the title classification in parentheses.

Block 5. Funding Numbers. To include contract and grant numbers, may include program element number(s), project number(s), task number(s), and work unit number(s). Use the following labels:

C - Contract	PR - Project
G - Grant	TA - Task
PE - Program Element	WU - Work Unit Accession No

Block 6. Author(s). Name(s) of person(s) responsible for writing the report, performing the research, or credited with the content of the report. If editor or compiler, this should follow the name(s).

Block 7. Performing Organization Name(s) and Address(es). Self-explanatory.

Block 8. Performing Organization Report Number. Enter the unique alphanumeric report number(s) assigned by the organization performing the report.

Block 9. Sponsoring/Monitoring Agency Name(s) and Address(es). Self-explanatory.

Block 10. Sponsoring/Monitoring Agency Report Number. (if known)

Block 11. Supplementary Notes. Enter information not included elsewhere such as: Prepared in cooperation with ; Trans. of ; To be published in . When a report is revised, include a statement whether the new report supersedes or supplements the older report.

Block 12a. Distribution/Availability Statement.

Denotes public availability or limitations. Cite any availability to the public. Enter additional limitations or special markings in all capitals (e.g. NOFORN, REL, ITAR).

DOD - See DoDD 5230.24, "Distribution Statements on Technical Documents."

DOE - See authorities.

NASA - See Handbook NHB 2200.2.

NTIS - Leave blank.

Block 12b. Distribution Code.

DOD - Leave blank.

DOE - Enter DOE distribution categories from the Standard Distribution for Unclassified Scientific and Technical Reports.

NASA - Leave blank.

NTIS - Leave blank.

Block 13. Abstract. Include a brief (*Maximum 200 words*) factual summary of the most significant information contained in the report.

Block 14. Subject Terms. Keywords or phrases identifying major subjects in the report.

Block 15. Number of Pages. Enter the total number of pages.

Block 16. Price Code. Enter appropriate price code (*NTIS only*).

Blocks 17. - 19. Security Classifications. Self-explanatory. Enter U.S. Security Classification in accordance with U.S. Security Regulations (i.e., UNCLASSIFIED). If form contains classified information, stamp classification on the top and bottom of the page.

Block 20. Limitation of Abstract. This block must be completed to assign a limitation to the abstract. Enter either UL (unlimited) or SAR (same as report). An entry in this block is necessary if the abstract is to be limited. If blank, the abstract is assumed to be unlimited.

Characterization of Laboratory Generated Turbulence

by

Optical Phase Measurements

I. Introduction

The resolution achieved by an optical imaging system in the presence of the random effects of the atmosphere is severely degraded from the theoretical diffraction limit. Increasing the size of the largest optical component of the imaging system does not, in all cases, increase the resolution achieved by the system. The characteristics of the atmosphere impose a limit to the amount of resolution achievable regardless of the diffraction limit. Atmospheric turbulence arises from random variations in the temperature and pressure of the air that are induced by the nonuniform heating of the Earth's surface by the sun. The random variations in temperature and pressure cause random fluctuations, both temporal and spatial, in the index of refraction of the air. These refractive index inhomogeneities cause random variations in the phase and amplitude of the wavefront that is propagated through the atmosphere.

The performance of an optical imaging system is often described in terms of its spatial frequency response, the optical transfer function (OTF), which is related to the size of the optics. If the optical imaging system could respond ideally to all spatial frequencies, the image produced by the system would be identical to the object. However, there is a theoretical diffraction limit to the spatial frequency response of imaging systems. Telescopes used for imaging astronomical objects are designed with this theoretical limit in mind—the larger the telescope pupil, the better the spatial frequency response of the system. There is another factor that limits the amount of resolution attainable in astronomical imaging systems—the Earth's atmosphere. In the presence of atmospheric turbulence, the performance of an imaging system can be described only in terms of an average OTF. The average OTF is the product of the diffraction limited OTF and the average OTF

of the atmosphere [19]. The average OTF of the atmosphere is related to a second order statistic of the random phase variations induced by the atmosphere, specifically, the phase structure function, D_s . The phase structure function is a measure of the correlation of the phase between two points in a plane perpendicular to the direction of propagation. If the turbulence is homogeneous, the value of the phase structure function will depend only on the coordinate differences, Δx and Δy , between the two points. If the turbulence is homogeneous and isotropic, D_s will depend only on the magnitude of the separation between the two points, $\sqrt{\Delta x^2 + \Delta y^2}$.

There are currently several methods that attempt to restore diffraction limited imaging performance in the presence of the turbulent atmosphere. Techniques include, but are by no means limited to: speckle imaging [1, 3, 17, 28, 29, 31, 32, 42, 47], deconvolution [5, 40], and adaptive optics [2, 14, 16, 20, 21, 22, 36, 38, 39, 46].

Adaptive optical systems provide real-time control of the optical wavefront phase to improve imaging performance in the presence of atmospheric turbulence. The components of an adaptive optical system are: a wavefront measuring device; a wavefront modifying device, such as a deformable mirror; and an information processing device to provide the proper control signals to the wavefront modifying device. The perturbed wavefront phase is measured by the wavefront sensing device and the data is passed to the information processing device where the control signals for the wavefront modifying device are calculated.

Speckle imaging is a type of post-processing technique used to overcome the effects of atmospheric turbulence on imaging systems. The technique, developed by Labeyrie [29], extracts high spatial frequency information about the object from a series of short exposure images. There are various techniques for extracting the information about the object from the short exposure images.

Another post-processing technique involves the deconvolution of the short exposure image and the associated point spread function. In the spatial frequency domain, this deconvolution

becomes a division of the Fourier transform of the image by the instantaneous optical transfer function (OTF). The deconvolution yields an estimate of the structure of the original object.

A properly characterized turbulence generator with statistics that match those of atmospheric turbulence would allow for testing adaptive optics and image enhancement techniques in a controlled laboratory environment. With such a turbulence generator, the ability to test current techniques, as well as develop new techniques, would be greatly enhanced. Also, the time and money invested in testing image enhancement techniques in the Earth's atmosphere as opposed to laboratory testing would be reduced because the uncertainty of weather conditions would no longer be a factor. It should be noted that the author does not mean to imply that testing these techniques with simulated atmospheric turbulence could totally eliminate the need for testing the techniques in the atmosphere. Laboratory testing would give more careful insight into the operating characteristics of the techniques before deciding to invest the time and money for testing in the Earth's atmosphere. Laboratory generated turbulence has been utilized to simulate the effects of atmospheric turbulence and test the properties of optical propagation in a random media. However, several of these turbulence generators have been developed without thoroughly characterizing the statistical properties of the turbulence [6, 10, 35]. In order to test wavefront compensation techniques, a fully characterized turbulence generator with statistics that match those of the atmosphere is needed.

Applications of a properly characterized turbulence generator are not limited to the testing of image enhancement techniques. Atmospheric turbulence adversely affects the propagation of all electromagnetic waves. Experiments could easily be developed to test the operation of electromagnetic communications—both radar and laser, directed energy weapons, and electro-optic designators, as well as any other application dealing with the propagation of electromagnetic waves in the Earth's atmosphere.

1.1 Scope

A statistically characterized turbulence generator, with statistics that match those of atmospheric turbulence, is needed to test current and future adaptive optics and image enhancement techniques. The scope of this effort is to build a laboratory scaled turbulence generator that can be used to study effects of turbulent media on an optical imaging system. In order to determine the effects of this turbulence on optical imaging, the statistical properties of the generated turbulence must be determined. The random effects of the generated turbulence are characterized by directly measuring the wavefront phase perturbation induced by the turbulence and, from these measurements, estimating the phase structure function. From this estimate of the structure function, homogeneity and isotropy, as well as presence of an inertial subrange, will be determined. No effort will be made to determine how the turbulence is distributed within the cell, because we are concerned only with the overall effect of the turbulence.

Chapter II briefly summarizes the theory involved with imaging in the presence of random media. A widely accepted model of atmospheric turbulence and the effects of atmospheric turbulence on optical imaging are also presented. Examples of past work relating to this project are then discussed. The chapter closes with a statement of the problem addressed by this project. Chapter III describes the operation of the wavefront sensing instrument and the design of the turbulence chamber used in this experiment. The experimental setup and the procedures for characterizing the generated turbulence are also discussed. Chapter IV presents the results of the experiment and Chapter V gives some conclusions about the results.

II. Background

This chapter will introduce some background information needed to understand the problem that is addressed by this research. The theory involved with characterizing the performance of optical imaging systems is outlined. A brief summary of some of the past research relating to the design and characterization of turbulence used for imaging experiments is also discussed. The chapter closes with a problem statement, giving the motivation and purposes of this research project.

2.1 Current Theory

In this section, the foundation for characterizing the performance of an optical imaging system is laid. Introduced first is the primary measure of performance for imaging, the optical transfer function (OTF). The effects of random wavefront phase variations on the OTF are also presented. Next, a widely accepted model of atmospheric turbulence is discussed. Using this model, an OTF for a system subjected to the random effects of the atmosphere is presented.

2.1.1 Frequency response of imaging systems. The spatial frequency response of an incoherent imaging system under quasi-monochromatic conditions is described in terms of the optical transfer function (OTF), $\mathcal{H}_o(\nu_x, \nu_y)$:

$$\mathcal{H}_o(\nu_x, \nu_y) = \frac{\iint_{-\infty}^{\infty} dx dy P(x, y) P^*(x - \bar{\lambda} f \nu_x, y - \bar{\lambda} f \nu_y)}{\iint_{-\infty}^{\infty} dx dy |P(x, y)|^2}, \quad (2.1)$$

where ν_x and ν_y are x - and y -directed spatial frequencies, P is the pupil function, f is the effective focal length of the imaging system, and $\bar{\lambda}$ is the mean wavelength of the quasi-monochromatic light [18]. If we consider a random screen, $t_s(x, y)$, placed at the pupil of the imaging system, the OTF

becomes [19]:

$$\mathcal{H}_o(\nu_x, \nu_y) = \frac{\iint_{-\infty}^{\infty} dx dy \mathbf{P}(x, y) \mathbf{P}^*(x - \bar{\lambda} f \nu_x, y - \bar{\lambda} f \nu_y) \mathbf{t}_s(x, y) \mathbf{t}_s^*(x - \bar{\lambda} f \nu_x, y - \bar{\lambda} f \nu_y)}{\iint_{-\infty}^{\infty} dx dy |\mathbf{P}(x, y)|^2 |\mathbf{t}_s(x, y)|^2}. \quad (2.2)$$

Due to the random nature of $\mathbf{t}_s(x, y)$, a deterministic analysis of the OTF is impossible. The best way to describe the OTF is an average OTF, $\bar{\mathcal{H}}(\nu_x, \nu_y)$. The average OTF is defined as [19]:

$$\bar{\mathcal{H}}(\nu_x, \nu_y) = \frac{E[\text{numerator of the OTF}]}{E[\text{denominator of the OTF}]}, \quad (2.3)$$

where $E[\cdot]$ is the expectation operator. Substituting Equation 2.2 into Equation 2.3 yields an average optical transfer function given by

$$\bar{\mathcal{H}}(\nu_x, \nu_y) = \mathcal{H}_o(\nu_x, \nu_y) \bar{\mathcal{H}}_s(\nu_x, \nu_y), \quad (2.4)$$

where \mathcal{H}_o is the OTF of the optical system in the absence of the screen and $\bar{\mathcal{H}}_s$ is the average OTF of the screen. If the transmittance function $\mathbf{t}_s(x, y)$ is of the form

$$\mathbf{t}_s(x, y) = \exp[j\phi(x, y)], \quad (2.5)$$

then $\mathbf{t}_s(x, y)$ is referred to as a random phase screen. If $\phi(x, y)$ is a Gaussian random process and is at least stationary in first increments, then the average OTF of the screen is given by [19]

$$\bar{\mathcal{H}}_s(\nu_x, \nu_y) = \exp \left[-\frac{1}{2} D_\phi(\bar{\lambda} f \nu_x, \bar{\lambda} f \nu_y) \right], \quad (2.6)$$

where D_s is the phase structure function defined by,

$$D_s(\Delta x, \Delta y) = \langle [\phi(x + \Delta x, y + \Delta y) - \phi(x, y)]^2 \rangle, \quad (2.7)$$

and $\langle \cdot \rangle$ denotes the ensemble average.

These equations lay the basis for how the performance of an imaging system in the presence of random medium is characterized. Under certain assumptions—near field approximations—the effects of the atmosphere can be modeled as a simple phase screen of the form of Equation 2.5 and the average OTF will take on the same form as Equation 2.4 where \bar{H}_s is the average OTF of the atmosphere [19].

2.1.2 Atmospheric turbulence. The atmosphere undergoes random variations in its temperature and pressure that induce random fluctuations, both temporal and spatial, in the index of refraction, n . These refractive index inhomogeneities present in the atmosphere can be modeled as turbulent “eddies,” or packets of air, each with a characteristic refractive index. The quantity and dimensions of these eddies can be characterized by a power spectral density $\Phi_n(\vec{\kappa})$, where $\vec{\kappa} = (\kappa_x, \kappa_y, \kappa_z)$ is called the wavenumber vector, having units of radians per meter. $\Phi_n(\vec{\kappa})$ is a measure of the relative occurrence of eddies with dimensions $L_x = 2\pi/\kappa_x$, $L_y = 2\pi/\kappa_y$, $L_z = 2\pi/\kappa_z$. If the turbulence is homogeneous and isotropic, this power spectrum will depend only on the radial scalar, $\kappa = |\vec{\kappa}|$. For values of κ greater than some critical wavenumber κ_o and less than some critical wavenumber κ_m , called the inertial subrange of the spectrum, the form of Φ_n can be predicted from the physical laws governing turbulent flow and is given by:

$$\Phi_n(\kappa) = 0.033 C_n^2 \kappa^{-11/3} \quad \kappa_o < \kappa < \kappa_m, \quad (2.8)$$

where C_n^2 is called the structure constant of the refractive index fluctuations [19]. C_n^2 serves as a measure of the strength of the index fluctuations, and the critical wavenumbers κ_o and κ_m .

are related to the scale sizes of the turbulent eddies. The scale size $L_o = 2\pi/\kappa_o$ is called the outer scale of the turbulence, corresponding to the largest eddy size, and the scale size $l_o = 2\pi/\kappa_m$ is called the inner scale of the turbulence, corresponding to the smallest eddy size. The value of the structure constant, C_n^2 , depends on the local atmospheric conditions. Typical values range from 10^{-13} meter $^{-2/3}$ for strong turbulence to 10^{-17} meter $^{-2/3}$ for weak turbulence, with 10^{-15} meter $^{-2/3}$ often quoted as the typical "average" value [19].

The effect of these random variations of index on an optical system can often be described using the phase structure function:

$$D_\phi(\vec{r}_1, \vec{r}_2) = \langle [\phi(\vec{r}_1) - \phi(\vec{r}_2)]^2 \rangle, \quad (2.9)$$

where ϕ is a temporal realization of the perturbed wavefront phase, \vec{r} is a position vector in the pupil plane, and $\langle \cdot \rangle$ denotes ensemble. If the random variations in the index of refraction are homogeneous and isotropic, the phase structure function, D_ϕ , will depend only on the magnitude of the separation, $r = |\vec{r}_1 - \vec{r}_2|$, between the two points. When the turbulence is characterized by Kolmogorov statistics, this structure function will be proportional to $r^{5/3}$ for values of r within the inertial subrange [19].

In order to specify a detailed expression for the average OTF of the atmosphere, an expression for the phase structure function must be found. Using the model of the atmosphere as described above (Equation 2.8) and near-field approximations, a detailed expression for the phase structure function, D_ϕ , can be found [19].

$$D_\phi(r) = 2.91 \left(\frac{2\pi}{\lambda} \right)^2 C_n^2 z r^{5/3}, \quad (2.10)$$

where z is the propagation path length within the turbulence. In writing Equation 2.10 as a function only of $r = |\vec{r}_1 - \vec{r}_2|$, it is implied that the turbulence is homogeneous and isotropic.

2.1.3 Average OTF of the atmosphere. Atmospheric turbulence induces random fluctuations in the phase and amplitude of an optical wave that has propagated through the atmosphere. When imaging down through the atmosphere, as is the case when imaging stars and satellites, the atmospheric turbulence exists from the surface of the Earth, where it is strongest, to an altitude of about 20 kilometers [27]. If the observatory is located where the atmospheric "seeing" is good, for example on a mountaintop, a near field approximation can be made. Under these approximations, the turbulence is weak enough that amplitude scintillation effects are not present and only phase effects degrade imaging performance. These phase effects can be integrated along the propagation path and be modeled as a phase screen placed in the pupil of the imaging system. If the phase perturbation is a Gaussian random process and at least stationary in first increments, the average OTF of the atmosphere can be given by:

$$\overline{H}_s(\nu) = \exp \left[-\frac{1}{2} D_s(\lambda f \nu) \right], \quad (2.11)$$

where $\nu = [\nu_x^2 + \nu_y^2]^{1/2}$ and D_s is the phase structure function. Substituting the expression for $D_s(r)$ from Equation 2.10 into Equation 2.11, the expression for the OTF of the atmosphere becomes:

$$\overline{H}_s(\Omega) = \exp \left\{ -57.4 \frac{C_n^2 z}{(\lambda)^{1/3}} \Omega^{5/3} \right\}. \quad (2.12)$$

By expressing \overline{H}_s as a function of Ω , frequency measured in units of cycles per radian of arc, Equation 2.12 is independent of the optical system parameters. The relationship between Ω and ν is $\Omega = f\nu$. Equation 2.12 can then be substituted into Equation 2.4 to obtain the total OTF of the system. It should be noted that up until now it has been assumed that the value of C_n^2 is constant over the propagation path. More generally, the phase structure function, $D_s(r)$, can be written as:

$$D_s(r) = 2.91 \left(\frac{2\pi}{\lambda} \right)^2 r^{5/3} \int_0^r d\xi C_n^2(\xi). \quad (2.13)$$

To simplify Equation 2.13, the atmospheric coherence diameter, r_o , is defined:

$$r_o \equiv 0.185 \left[\frac{(\lambda)^2}{\int_0^\infty d\xi C_n^2(\xi)} \right]^{3/5} \quad (2.14)$$

The atmospheric coherence diameter (also called the Fried seeing-cell size) was first introduced by Fried [12]. Substituting Equation 2.13 into Equation 2.11, the average OTF of the atmosphere can be expressed as:

$$\overline{H}_s(\Omega) = \exp \left\{ -3.44 \left(\frac{\lambda \Omega}{r_o} \right)^{5/3} \right\} \quad (2.15)$$

The atmospheric coherence diameter, r_o , is useful in understanding the effects of atmospheric turbulence on optical imaging systems. The resolution of an imaging system can be increased by increasing the size of the aperture until it reaches approximately r_o . Increasing the size of the aperture beyond r_o does not increase the imaging resolution of the system. In other words, the best resolution achievable by an imaging system in the presence of atmospheric turbulence is equivalent to the resolution achievable by a diffraction limited imaging system with an aperture the size of r_o . Typical values of r_o at a good observatory range from 5 to 20 centimeters, depending on the seeing conditions. A plot of the OTF for a diffraction-limited circular optic with a 4 meter diameter is shown in Figure 2.1. Shown on the same plot, with a dotted line, is the average OTF for the same system in the presence of atmospheric turbulence with $r_o = 10$ centimeters.

The expression for D_s given in Equation 2.9 is a theoretical expression that can be estimated only experimentally. In practice, D_s can be estimated, either in the laboratory or at an actual observatory, by using

$$\hat{D}_s(\vec{r}_1, \vec{r}_2) = \frac{1}{N} \sum_{i=1}^N [\phi_i(\vec{r}_1) - \phi_i(\vec{r}_2)]^2, \quad (2.16)$$

where the $\hat{\cdot}$ denotes an estimate, $\phi_i(\vec{r})$ is the measured value of the phase at point \vec{r} , and N is the number of realizations of the wavefront phase. This expression for the phase structure function is an estimate only due to the finite number of wavefront realizations.

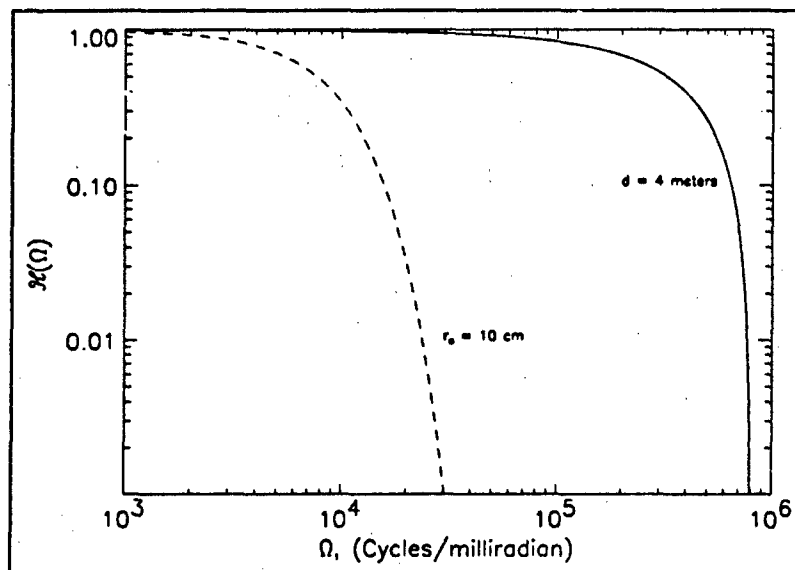


Figure 2.1. Comparison of the average OTF of a system with and without the effects of atmospheric turbulence ($\bar{\lambda} = 0.5$ micrometers). Solid line represents the diffraction limited OTF.

2.2 Past work

Several references address experimental measurement of turbulence effects on optical waves propagated through laboratory generated turbulence. Techniques used for producing turbulence vary from simple hot plates and convection [35] to complex water-filled tanks [7]. The design found to best suit the type of turbulence desired has been built and partially characterized by Majumdar and Gamo [15, 33, 34]. This design utilizes a chamber 2.69 meters long, 0.78 meters wide, and 0.23 meters high. The turbulence is generated by ten heater/blowers mounted on one side of the chamber and is homogenized by a screen of aluminum foil and three layers of aluminum meshes (see Figure 2.2). There are several different techniques used to experimentally characterize the statistical properties of turbulence. The majority of these techniques focus on estimating the second order statistics of some parameter, such as temperature. The effects of the turbulence on imaging performance are then inferred, through existing relationships, from the measured statistics.

2.2.1 Temperature structure function. Majumdar and Gamo measure the temperature structure function as a primary means of characterizing the generated turbulence [15]. The temperature structure function is defined as the mean square temperature difference between two temperature probes,

$$D_T(\vec{r}_1, \vec{r}_2) = \langle [T(\vec{r}_1) - T(\vec{r}_2)]^2 \rangle, \quad (2.17)$$

where T is the temperature and \vec{r} is the position vector of the temperature measuring probe. When temperature fluctuations are homogeneous and isotropic, the structure function will depend only on the magnitude of the separation of the probes, r , where $r = |\vec{r}_1 - \vec{r}_2|$. Two micro-thermocouple probes are used by Majumdar and Gamo to measure instantaneous temperature difference between two locations within the turbulence. Probe separation is adjusted from 2 millimeters up to 20 centimeters in increments of 10 micrometers. This data is then squared and averaged to obtain an estimate of the temperature structure function. In the inertial subrange, the temperature structure function is proportional to $r^{2/3}$:

$$D_T(r) = C_T^2 r^{2/3}, \quad (2.18)$$

where C_T is the temperature structure constant [45]. This 2/3 power relationship is often called the Kolmogorov-Obukhov similarity law [15].

The data taken by Majumdar and Gamo indicate that the properties of the turbulence generated obey the Kolmogorov-Obukhov similarity law for probe separations between 2 centimeters and 6 centimeters at the location $x = 0.38$ meters, $y = 0.12$ meters, and $z = 1.09$ meters within the turbulence generator (see Figure 2.2). From a plot of the data obtained, a value for the strength of temperature fluctuations, C_T^2 , was obtained and found to be $52.9^\circ \text{ K}^2 \text{ m}^{-2/3}$.

The refractive index structure function is defined as:

$$D_n(\vec{r}_1, \vec{r}_2) = \langle [n(\vec{r}_1) - n(\vec{r}_2)]^2 \rangle, \quad (2.19)$$

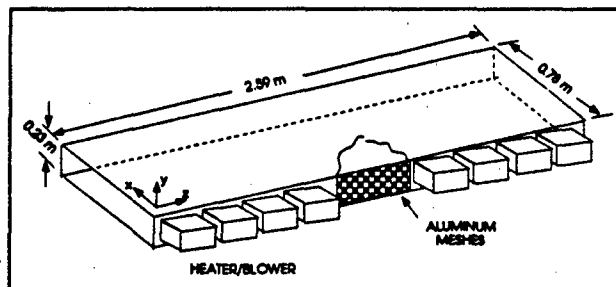


Figure 2.2. Turbulence generator used by Majumdar [15].

where $n(\vec{r})$ is the index of refraction variation at position \vec{r} . In the inertial subrange of homogeneous and isotropic turbulence, $D_n(\vec{r})$ can be expressed with the same 2/3 power relationship as the temperature structure function:

$$D_n(r) = C_n^2 r^{2/3}. \quad (2.20)$$

The refractive index structure constant, C_n , can be expressed as a function of the temperature structure constant C_T [15] assuming constant pressure,

$$C_n = \frac{77.6 P}{T^2} \left(1 + \frac{0.00753}{\lambda^2} \right) \times 10^{-6} C_T, \quad (2.21)$$

where P is the pressure in millibars, T is the temperature in degrees Kelvin, and λ is the optical wavelength. Using this expression for the index structure constant and Equation 2.10, an expression for the phase structure function can be found.

2.2.2 Mean square phase fluctuations. Another technique commonly used to characterize the statistics of turbulence is to directly measure the statistics of the phase variations. Carnevale, Bertolotti, and their associates utilize a Mach-Zender interferometer to measure the mean square value of the phase fluctuations, $\langle \phi^2 \rangle$, of a laser beam propagated through turbulence [6, 10]. If the mean value of ϕ is zero and the turbulence is homogeneous and isotropic, then the phase structure

function can be found using the expression

$$D_s(r) = 2[\overline{\phi^2} - C_{\phi\phi}(r)], \quad (2.22)$$

where $C_{\phi\phi}(r)$ is the correlation function of ϕ , defined by

$$C_{\phi\phi}(r) = \overline{\phi(\vec{r}_1)\phi(\vec{r}_2)}. \quad (2.23)$$

The turbulence is produced by flowing air over a heated nichrome grid as shown in Figure 2.3. Carnevale and his associates measure the mean square phase variations between the two beams propagated through the turbulence by examining the interference pattern formed [10]. The mean squared phase variations are measured for distances from the heated grid, x , ranging from 1 to 3 meters while holding the separation between the two beams, d , constant; therefore, the dependence of the mean square phase fluctuations on separation distance cannot be determined. However, Bertolotti and his associates measure this dependence for a similar turbulence generator, and the data suggest that an inertial subrange, as described by Kolmogorov, does exist in this turbulence [6].

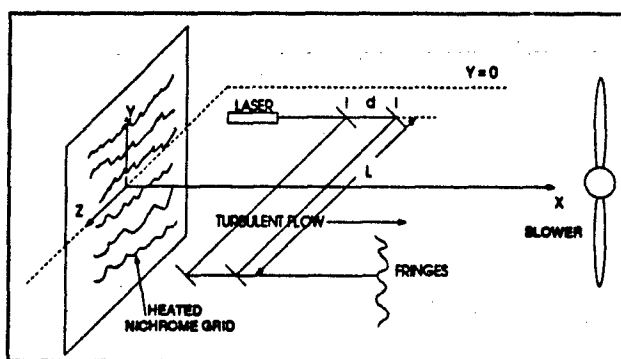


Figure 2.3. Turbulence generator used by Carnevale [10].

2.3 Problem

A statistically characterized turbulence generator is needed to test current and future adaptive optics and image enhancement techniques. The structure of the turbulence must match the known characteristics of the atmosphere and the resulting phenomena must be scaled to laboratory dimensions. As opposed to laboratory testing, testing these techniques in the Earth's atmosphere imposes many limitations. In the atmosphere there is no control over meteorological conditions which can change over the time required to perform the testing. When attempting to characterize a random process in terms of average effects, several realizations of the effects must be obtained to ensure confidence in the estimate. In order to accurately characterize the effects of the atmosphere on optical propagation, several "pictures" of the turbulence effects must be taken and averaged. Obtaining an accurate estimate imposes the requirement of taking large amounts of data over long periods of time to obtain an appropriate sample size. If the sample size is not large enough, an accurate estimation of the turbulence effects is improbable [4]. Therefore, accurately testing image enhancement techniques at an observatory becomes very expensive and time consuming. With the added variable of weather conditions, the burden becomes even greater. Using a laboratory scaled turbulence generator, with statistics matching those of atmospheric turbulence, the testing of image enhancement techniques can be conducted in the controlled environment of the laboratory providing a first step in determining the performance of new image enhancement techniques.

This chapter has introduced some background information needed to understand the problem that is being addressed by this research. Of particular importance is the dependence of the average optical transfer function of the atmosphere, from Equation 2.11, on the phase structure function, D_p . The phase structure function is a measure of the correlation of the phase between two points in a plane perpendicular to the direction of propagation and can be estimated only in practice.

In the next chapter, the experimental procedures used to characterize the statistics of laboratory generated turbulence are discussed. The technique used is new in that the effects of the

turbulence are characterized by directly measuring the perturbed wavefront phase with a wavefront sensor and estimating the phase structure function, \hat{D}_ϕ . Because the phase structure function is directly related to the average OTF by Equation 2.11, the effects of the turbulence on imaging performance can be realized without the need of inferring \hat{D}_ϕ from other measured quantities.

III. Experimental Setup and Procedures

A turbulence chamber has been produced for the purpose of testing existing and future techniques used to improve imaging performance in the presence of atmospheric turbulence. An experiment has been designed to characterize a second order statistic of the turbulence, the phase structure function. This experiment utilizes a unique technique for estimating the phase structure function, \hat{D}_s . The wavefront phase of an optical beam subjected to the random effects of the turbulence is sensed with a wavefront measuring device—a shearing interferometer—and the phase structure function is estimated from these phase measurements. Because the phase structure function is directly related to the average OTF of an imaging system, no inferences are made about the effects of the turbulence on imaging performance.

In this chapter, a description is given of the experimental procedures used to characterize the statistics of the generated turbulence. Figure 3.1 shows a block diagram of the experimental setup. A plane-wave is propagated through the lab-generated turbulence, and the perturbed wavefront is sensed by the wavefront sensing device. The wavefront sensor gives an estimate of the wavefront phase. It is from this measured wavefront phase that the phase structure function of Equation 2.16 is calculated. Section 3.1 discusses the wavefront sensor; Section 3.2 introduces the design of the turbulence chamber; and Section 3.12 addresses the actual experimental setup.

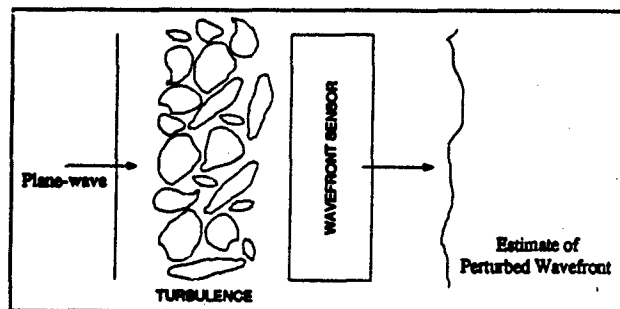


Figure 3.1. Block diagram of the experimental setup used.

3.1 Shearing interferometer

The shearing interferometer (SI) is the wavefront measuring instrument used in the experiment due to its high spatial resolution capabilities. The spatial sampling interval is approximately 0.5 millimeters. The SI is shown in Figure 3.2. For a detailed description of the shearing interferometer, including the mathematics describing its operation, the reader is referred to Appendix A; a qualitative description and an example are given below.

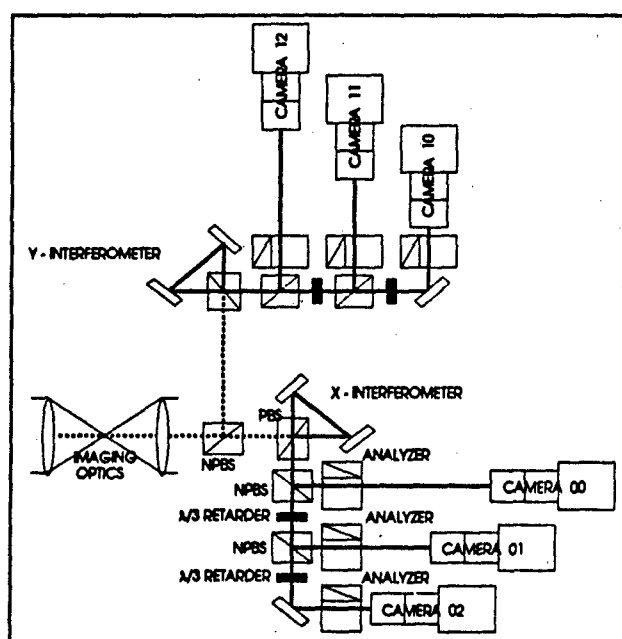


Figure 3.2. Shearing Interferometer.

As can be seen in Figure 3.2, there are two identical legs of the SI, the x -interferometer and the y -interferometer. The purpose for the two identical legs will become apparent shortly; for now, the discussion is limited to one leg of the SI. The input beam, which is linearly polarized at 45 degrees, is split into two independent beams with orthogonal linear polarizations by a polarizing beam splitter (PBS). The PBS, in combination with two mirrors, forms an equal path interferometer that produces a lateral shear in one beam with respect to the other (see Figure 3.3). The two beams, one laterally displaced from the other in either the x - or the y -direction, then pass through the

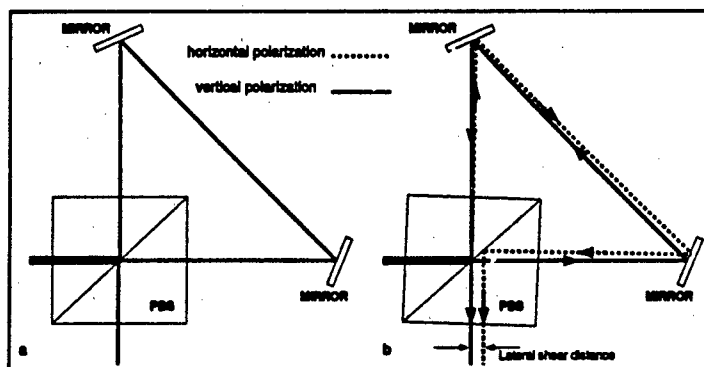


Figure 3.3. Method of producing lateral shear. a) No lateral shear produced. b) Lateral shear produced by rotating the PBS.

analyzer which recombines the independent beams and forms a pattern of interference fringes in the area of overlap. The fringes produced are proportional to the slope of the wavefront in the direction of shear (see Figure 3.4). In order to fully characterize the wavefront using a lateral shearing interferometer, two interferograms with mutually perpendicular shear directions must be used. This is the purpose of the two legs of the SI. The x -interferometer shears the beam in the x -direction and the y -interferometer shears the beam in the y -direction.

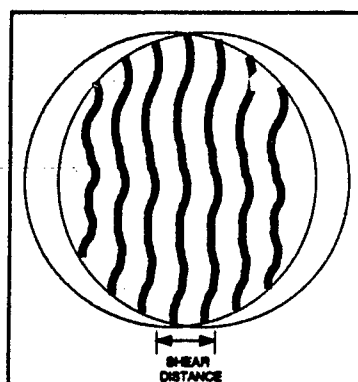


Figure 3.4. Overlap fringes in a Shearing Interferometer.

The slope measurements obtained from the SI must then be reconstructed into a phase map of the input wavefront. Wavefront reconstruction is performed by a software program that reads

in the interference patterns formed by the SI and, using a technique discussed by Hudgin [26], reconstructs the slope information into a phase map. This SI can sense a phase difference of $1/2$ wave ($\lambda/2$) per shear distance without any ambiguity. If the phase difference exceeds the $1/2$ wave per shear distance, an unresolvable ambiguity results. Therefore, decreasing the amount of shear induced in the beam will increase the magnitude of the phase variations that can be sensed. A larger shear induced into the beam tends to increase the signal, and the sensitivity to small values of the slope. Thus, when setting the shear distance, a tradeoff must be considered; use a small shear to sense large slopes with decreased sensitivity, and a larger shear to sense small slopes with limited dynamic range.

As an example of the information provided by the SI and associated software, a beam that is de-focused is input into the shearing interferometer. Figure 3.5 shows the raw interference patterns for the de-focused wavefront. The interference fringes of the images indicate areas where the phase difference between two points on the input wavefront separated by the shear distance is constant. The six images with interference fringes correspond to the three images with x -shear and three images with y -shear. The two sum images are simply the scaled sum of the three x -images and the scaled sum of the three y -images. Figure 3.6 shows a cross section through the center of each image parallel to the direction of shear. These plots clearly show the relationship described in Equations A.6-A.8 and plotted in Figure A.3. From these interference patterns produced by lateral shears, the x -tilt and y -tilt for each point within the aperture are calculated. The tilts, shown as surface plots, are shown in Figures 3.7 and 3.8. The wavefront slope estimates are then combined in a linear fashion and converted to absolute wavefront phase. The resulting wavefront phase is shown in Figure 3.9. Figure 3.10 displays two computer generated interferograms. The interference patterns are produced by digitally "interfering" the calculated wavefront with reference plane waves having a user defined amount of x - and y -tilt in waves. The amount of x - and y -tilt in the reference plane wave is shown below each interference pattern.

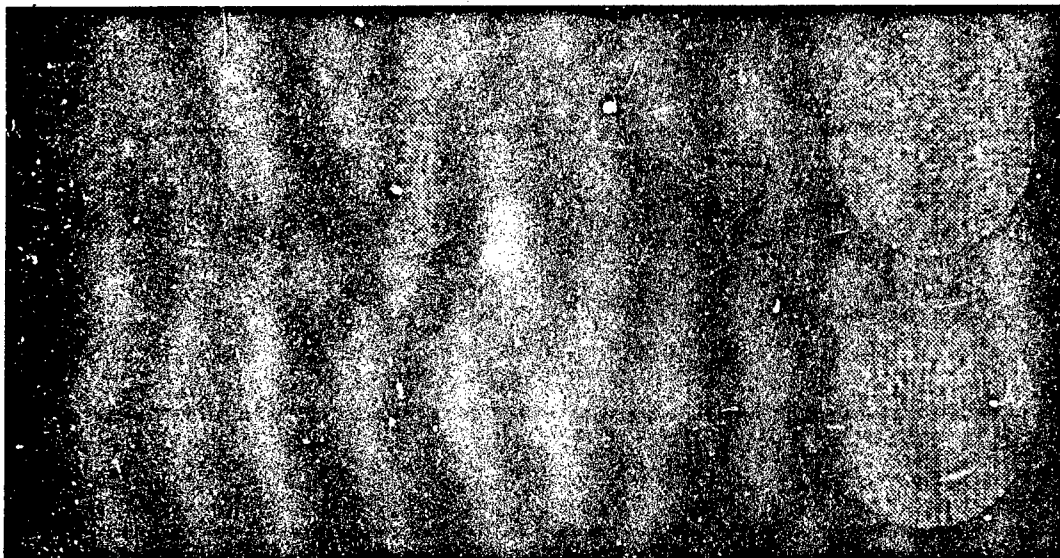


Figure 3.5. Raw interference images and sums for group 2147S, frame 0 (2147S/0).

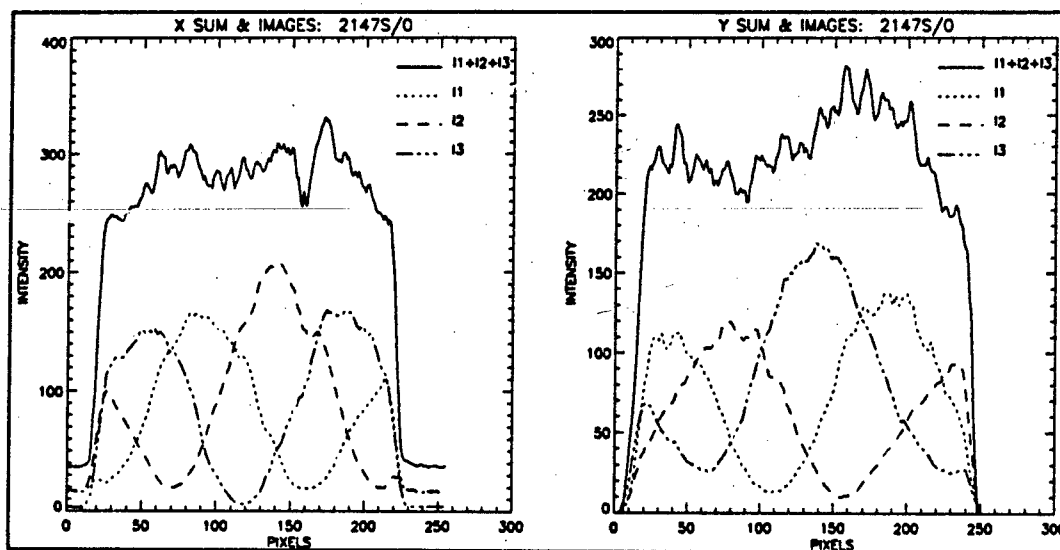


Figure 3.6. Cross sections of the raw images shown in Figure 3.5

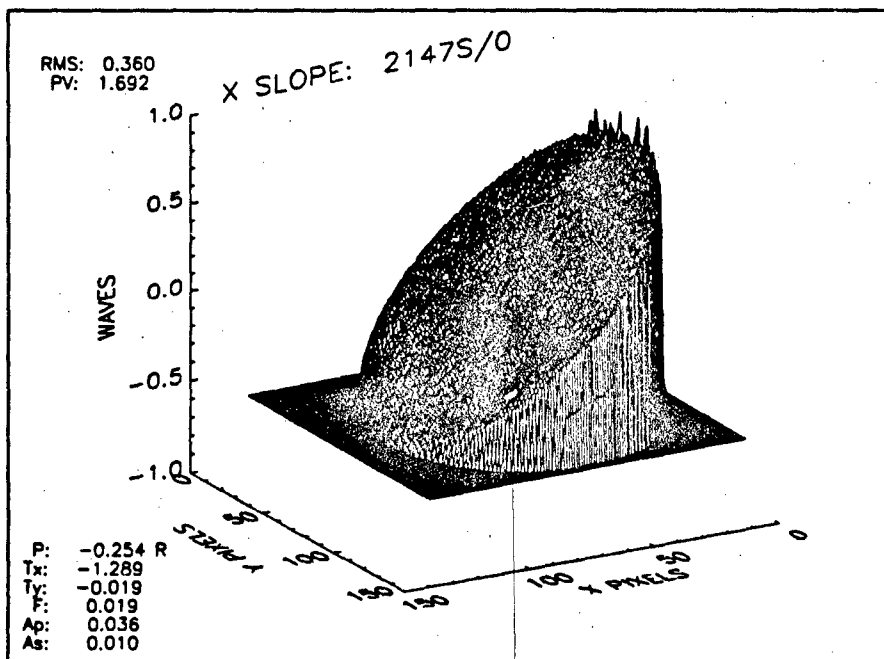


Figure 3.7. X-Tilt map for group 2147S, frame 0

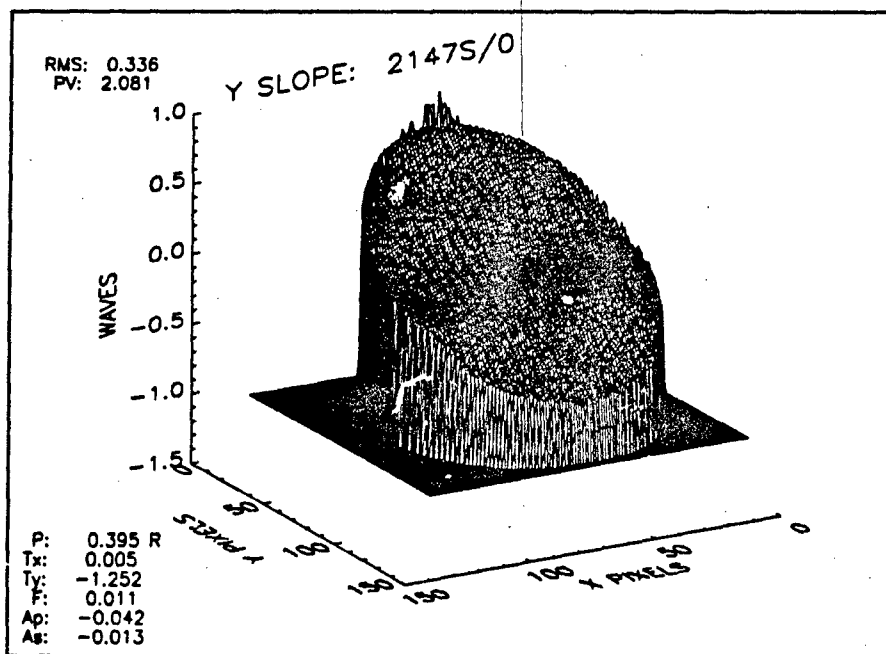


Figure 3.8. Y-Tilt map for group 2147S, frame 0

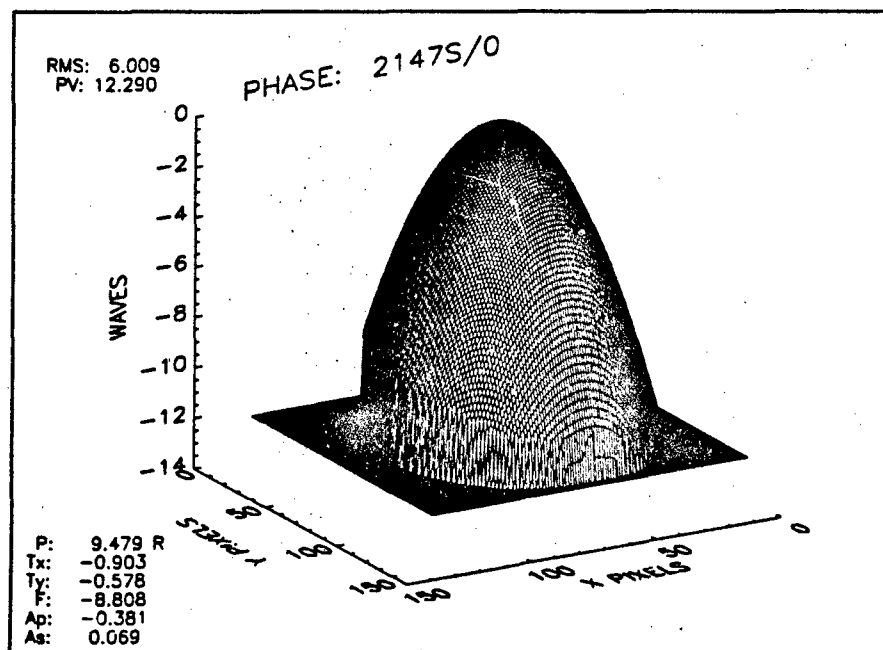


Figure 3.9. Phase map for group 2147S, frame 0.

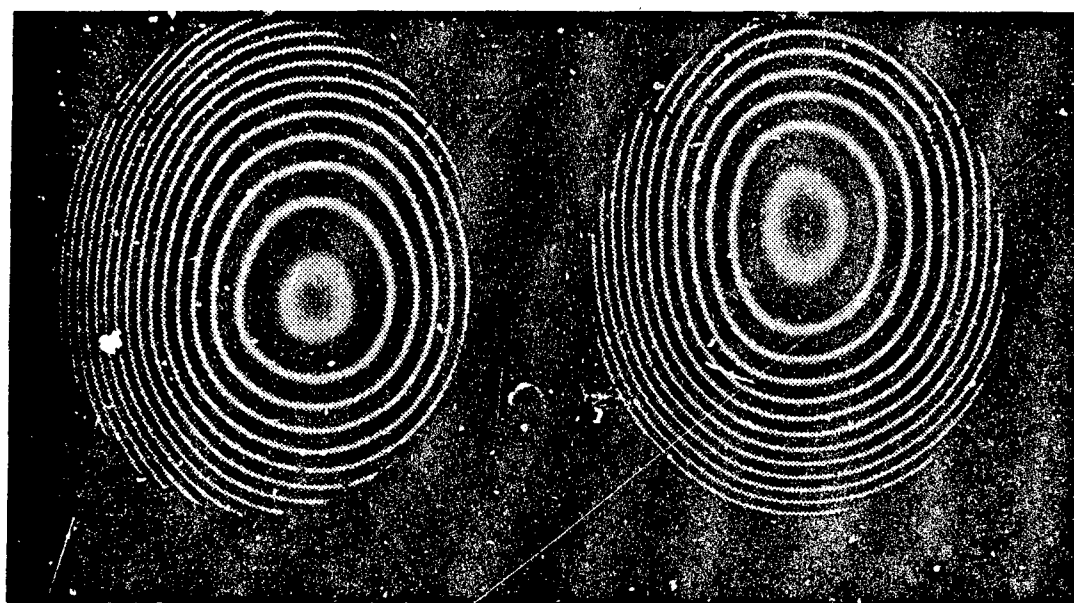


Figure 3.10. Computer generated interference patterns for group 2147S, frame 0.

3.2 Turbulence generator

A side view of the turbulence generator and the associated coordinate system used for this experiment is shown in Figure 3.11. The internal dimensions of the chamber are $5 \times 5 \times 18$ cubic inches. A turbulent flow through the chamber is created by two fans and a heating element. The turbulence generator is designed such that the airflow created will not interfere with the optical propagation outside the chamber. The flow is created parallel to the optical bench surface, the positive y -direction, and perpendicular to the optical transmission direction, the positive z -direction. The coordinate system designated in this section is used throughout the remainder of this thesis.

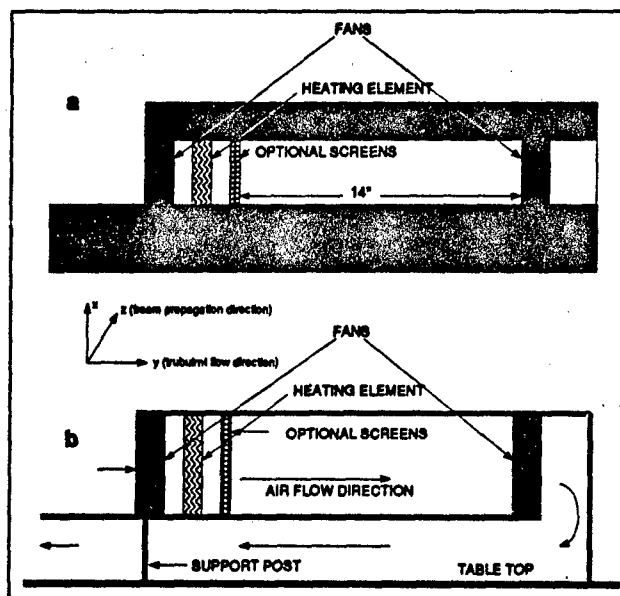


Figure 3.11. a) Turbulence generator. b) Plexiglass sides removed.

Figure 3.11a shows the turbulence generator with the plexiglass sides in place. The chamber is constructed of wood with plexiglass sides. An airflow is created in the positive y -direction by two DC Centaur model CNDC38D4-907 fans, one at each end. The speed of the fans is controlled by a Hewlett Packard 6205B Dual DC Power Supply. The temperature of the air within the chamber

is controlled by a heating element connected to a Cole Parmer model 2603 Voltage Controller. For experimental reproducibility purposes, fan speed and air temperature inside the chamber are measured. The fan speed is measured with a calibrated strobe, and the temperature is measured with a simple thermometer. If desired, screens can be inserted into the chamber to help break up the flow and homogenize the turbulence.

Figure 3.11b shows the turbulence generator with the plexiglass sides removed. From this diagram the airflow direction can be visualized. This turbulence chamber was designed by Thomas Baudendistel and built by the fabrication shop at the Air Force Institute of Technology (AFIT). Detailed design drawings of the turbulence chamber are given in Appendix C.

3.3 Experimental Setup

Figure 3.12 shows the optical setup used to experimentally determine the phase map of an optical wave propagated through laboratory generated turbulence. The shearing interferometer

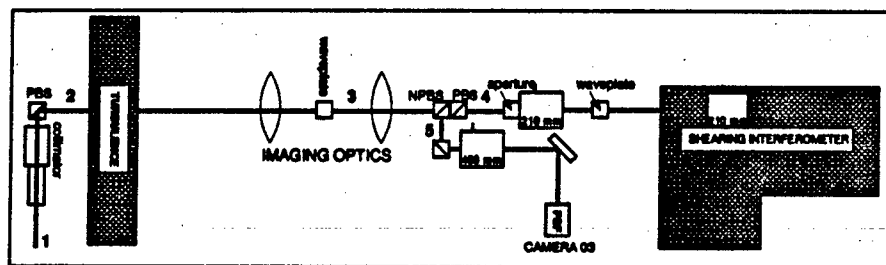


Figure 3.12. Experimental setup used.

shown in the figure is identical to that shown in Figure 3.2 and discussed in Section 3.1. The two 210-millimeter lenses, one on the SI, the other just prior to the SI, are the imaging optics shown in Figure 3.2. The laser beam in Figure 3.12 is passed through the collimator at location 1. The collimator produces a two-inch diameter beam. At location 2 the beam is linearly polarized in the vertical direction. The beam then passes through the lab generated turbulence. The imaging optics image a location just inside the turbulence generator onto the aperture at location 4. The location

of the aperture is referred to as the pupil plane of the SI. It should be noted that there will be other locations along the optical path where intermediate images are formed. The wave-plate at location 3 rotates the polarization by 90 degrees, giving horizontal polarization. The non-polarizing beam splitter (NPBS) at location 5 splits the beam so that a portion of the energy is directed to the Point Spread Function (PSF) camera. The Polarizing Beam Splitter (PBS) passes only the horizontally polarized portion of the beam that is passed through the NPBS. This PBS can be used with a pockel cell if a faster shutter speed is needed. The next two lenses, 210-millimeter focal lengths, image the pupil plane of the SI onto the six cameras of the SI and collimate the beam. The wave-plate just prior to the SI is an adjustable half-wave plate that can be rotated to change the input polarization to the SI. This wave-plate can be set to pass the vertical, horizontal, or both polarizations and is important to the calibration of the SI.

3.4 Experimental Procedures

In this section, the experimental procedures are described. The section begins with an introduction and an explanation of the common terms used throughout this section. Next, an explanation of how the measurement noise effects present in the experimental setup are determined. Characterizing the measurement noise present in the setup is an important step in the experiment, as it will determine the minimum sensitivity of the wavefront sensor. The final section provides a detailed explanation of how the estimate of the phase structure function is calculated.

3.4.1 Common terms. Measured wavefront data is stored into *groups*. Each *group* contains one or more *frames*—temporal realizations of the wavefront being measured. A *group* is classified as either a *reference group* or a *data group*, depending on the experimental conditions under which the information is acquired. A *reference group* is a group of 16 frames acquired with the turbulence turned off. These 16 frames are averaged to limit the effects of measurement noise, yielding a *reference wavefront*. A *data group* is a group of frames acquired under a particular set of

experimental conditions. These conditions include turbulence turned off, for noise characterization, and turbulence turned on, for phase structure function measurements. The strength of the turbulence can be varied as described in Section 3.2, and each data group is taken with the turbulence strength set to a particular level. Each data group consists of 120 frames, each giving independent realizations of the wavefront phase. The number of frames in a data group is determined by data storage limitations, instrument calibration limitations (see Appendix A), and sample size considerations—the larger the sample size, the more accurate the estimate of D_s .

In order to limit the systematic error effects, such as the limited optical quality of the components in the beam path, reference groups are acquired as closely in time as possible to data groups. The reference wavefront is then subtracted from each of the wavefronts in the data group, yielding a *delta-wavefront*, $\Delta\phi$, that carries only the random effects induced by the measurement noise and the turbulence.

3.4.2 Noise characterization. With the turbulence turned off, the noise is characterized by acquiring a reference group followed by acquiring a data group, consisting of 10 frames. The reference wavefront phase values are then subtracted from each of the measured data wavefronts. If there were no noise present in the system, the data wavefronts would be identical to the reference wavefront. Thus, subtracting the reference wavefront phase values from each of the measured data wavefronts would yield perfectly flat wavefronts. However, due mainly to measurement noise in the cameras, the measured delta-wavefront phases include some non-deterministic variations. These non-deterministic variations are characterized by calculating the combined mean and standard deviation of the phase values for all 10 delta-wavefronts, giving approximately 300,000 samples of the measurement noise. A histogram of the phase variations is also plotted. A measurement sensitivity can be calculated using the estimated statistics of the noise:

$$\epsilon_\phi = \sigma_{\Delta\phi} \times \text{SNR}_{\text{cameras}}, \quad (3.1)$$

where ϵ_ϕ is the sensitivity in the phase measurements, $\sigma_{\Delta\phi}$ is the standard deviation of the delta-wavefronts, and SNR cameras is the minimum signal-to-noise ratio required in the cameras.

3.4.3 Calculation of the phase structure function. The estimate of the phase structure function is calculated by acquiring a reference group followed by a data group with the turbulence at the desired setting. The reference wavefront phase values are then subtracted from each of the measured data wavefronts. The resulting delta-wavefronts, which carry the random effects induced by the turbulence, are analyzed to determine an estimate of the phase structure function, defined by Equation 2.16.

Because the phase structure function is directly related to the average OTF of the atmosphere, as discussed in Section 2.1.3, it will be the main statistic that is calculated. As discussed in Chapter II, the phase structure function is defined as the mean square phase difference between two points on the wavefront. By calculating $\hat{D}_s(\vec{r}_1, \vec{r}_2)$ as a function of the vectors \vec{r}_1 and \vec{r}_2 , no assumptions are made about the homogeneity or isotropy of the turbulence. Without the assumptions of homogeneity and isotropy, the averaging of the squared phase difference must be done for each vector separation across the ensemble of delta-wavefronts.

$$\hat{D}_s(\vec{r}_1, \vec{r}_2) = \frac{1}{N} \sum_{i=1}^N [\Delta\phi_i(\vec{r}_1) - \Delta\phi_i(\vec{r}_2)]^2, \quad (3.2)$$

where N is the number of realizations of $\Delta\phi$ within the group of data and \vec{r}_1 and \vec{r}_2 are points within the aperture. The number of delta-wavefront realizations in the ensemble is 120. Because $\Delta\phi$ is stored in a 256×256 array of which the aperture fills about 80 percent, there are approximately 52,425 different points that can be used for \vec{r}_1 and \vec{r}_2 . If every permutation of \vec{r}_1 and \vec{r}_2 were used to estimate the phase structure function, there would be as many as $(52,425 \times 52,424)/2 = 1,374,164,100$ different vector combinations. To reduce the number of vector combinations, a

representative sample of the 1,374,164,100 combinations is used to estimate the phase structure function.

The vectors used for calculating $\hat{D}_s(\vec{r}_1, \vec{r}_2)$ are determined by selecting a template of points within the aperture as shown in Figure 3.13. The first step in making this template is to determine where the wavefront phase should be sampled. Figure 3.13 shows the locations on the wavefront where all of the vector separations are centered. The circle represents the area over which the phase

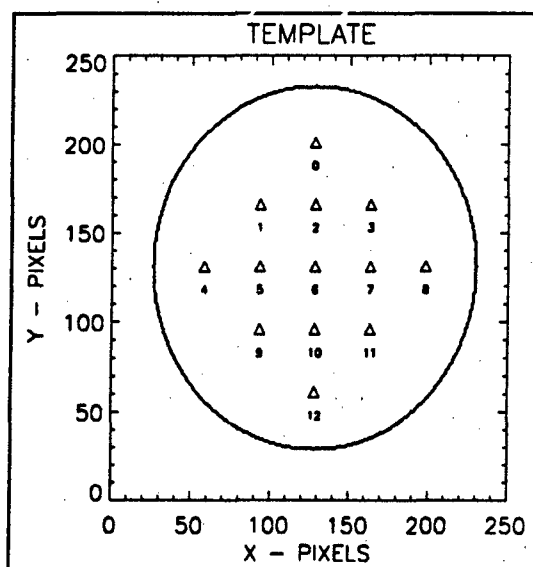


Figure 3.13. Template used to determine number of vectors within the aperture.

has been calculated. Points inside the circle represent good data points on the reconstructed delta-wavefront. The triangles within the circle serve as the origins for the different vectors, \vec{r}_1 and \vec{r}_2 . The vectors used are oriented at 0, +45, -45, and 90 degrees from the x -axis and centered on the template points shown in Figure 3.13. The magnitude of the difference between \vec{r}_1 and \vec{r}_2 is varied from the smallest value possible centered over the location of interest to the largest value possible while keeping both vectors, \vec{r}_1 and \vec{r}_2 , within the aperture. The number of possible vectors, and the maximum separation, varies depending on the vector orientation and the location within the aperture. For example, at location 0, the number of vector separations centered on that point in the

y -direction is less than the number in the x -direction. Also note that the largest vector separation between two points centered at location 0 is smaller in the y -direction than in the x -direction.

It is important to note that only the vectors having the same position, magnitude, and orientation within the wavefront are averaged over all realizations within the data group. Therefore, no assumptions are made about the homogeneity or the isotropy of the turbulence when estimating the phase structure function using Equation 3.2. The presence of these properties is determined by examining the functionality of the phase structure function. If the phase structure function is independent of vector orientation about a particular location, the turbulence is locally isotropic at that location. If the generated turbulence is homogeneous, the phase structure function will depend on only the vector separation, $\vec{r}_1 - \vec{r}_2$. If the phase structure function depends only on the magnitude of the vector separation, $|\vec{r}_1 - \vec{r}_2|$, then the turbulence is homogeneous and isotropic. Figure 3.14 illustrates the definitions of locally isotropic turbulence, homogeneous turbulence, and homogeneous and isotropic turbulence.

To test for isotropy, $\hat{D}_s(\vec{r}_1, \vec{r}_2)$ versus $|\vec{r}_1 - \vec{r}_2|$ is plotted for vector separations centered on one location within the aperture. Each of the four vector orientations centered on this location is plotted on the same graph. If the turbulence is isotropic, the plots will follow the same curve. When plotted on a log-log scale, a line with a slope of 5/3 is superimposed to determine if the structure function follows the Kolmogorov 5/3 power law relationship. This test for isotropy is accomplished for all 13 locations (see Figure 3.13) to determine if the turbulence is isotropic over the entire aperture. To test for homogeneity, $\hat{D}_s(\vec{r}_1, \vec{r}_2)$ versus $|\vec{r}_1 - \vec{r}_2|$ is plotted for a single vector orientation—say the x -direction—and compared by location within the aperture. For example, the structure function for locations 0, 1, 4, and 6 are all plotted on the same graph. If the turbulence is homogeneous for x -directed vector separations, the plots will follow the same curve. Again, a 5/3 slope line, on a log-log scale, is superimposed to determine if the structure function follows the Kolmogorov 5/3 power law relationship.

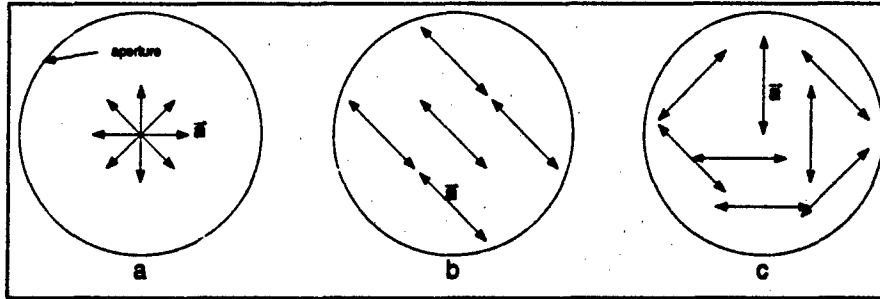


Figure 3.14. a) For locally isotropic turbulence, the value of the phase structure function, $D_s(\vec{a})$, is equal for all orientations of \vec{a} shown. b) For homogeneous turbulence, the value of $D_s(\vec{a})$ is equal for all \vec{a} shown. c) For homogeneous and isotropic turbulence, the value of $D_s(\vec{a})$ is equal for all orientation and locations of \vec{a} shown.

Properties of the phase structure function can be visualized by expanding the theoretical equation for the phase structure function (Equation 2.9):

$$D_s(\vec{r}_1, \vec{r}_2) = \langle \phi^2(\vec{r}_1) + \phi^2(\vec{r}_2) \rangle - 2C_{\phi\phi}(\vec{r}_1, \vec{r}_2), \quad (3.5)$$

where $C_{\phi\phi}(\vec{r}_1, \vec{r}_2)$ is the correlation function of ϕ . As the magnitude of $\vec{r}_1 - \vec{r}_2$ increases, the correlation function falls to zero and the phase structure function approaches the value $\langle \phi^2(\vec{r}_1) + \phi^2(\vec{r}_2) \rangle$. As the magnitude of $\vec{r}_1 - \vec{r}_2$ decreases, the value of $2C_{\phi\phi}(\vec{r}_1, \vec{r}_2)$ approaches $\langle \phi^2(\vec{r}_1) + \phi^2(\vec{r}_2) \rangle$ and the phase structure function will fall to zero.

Using optical phase measurements to determine statistical properties of laboratory generated turbulence eliminates the need for placing probes in the turbulence and possibly disrupting the actual characteristics of the turbulence. As described in Section 2.2.1, Majumdar [15, 34] and Bissonnette [7] use temperature probes to measure the temperature structure function, D_T , as a function of probe separation. These measurements are taken only at discrete locations along the length of the turbulence chamber and are used to characterize the turbulence at any location within the chamber. This assumes that the turbulence is homogeneous and isotropic at all locations when that may not be the case. The temperature structure function method used by Majumdar and

Bissonnette ignores any boundary layer disturbances that may be present at the front and back of the turbulent chamber. Boundary layers occur whenever a large gradient in the properties of the air is present. Effects of these boundary layers are difficult to characterize. Using the phase measurement technique, the effect of the boundary layer is not ignored; however, no attempt is made to characterize this disturbance. The optical phase measurements will also yield a phase structure function that is characteristic of the entire optical path within the turbulent chamber, unlike the temperature structure function which yields characteristics of discrete portions of the chamber. While measuring the temperature structure function does give an insight to the structure of the turbulence, the effects of this turbulence on optical imaging cannot be determined without calculating the phase structure function. The need to infer the phase structure function from the temperature structure function is eliminated by measuring the phase statistics directly.

A shortfall of measuring only the phase structure function is that the effects of the turbulence are integrated over the length of the cell giving no indication of how the turbulence is distributed within the cell. However, as stated in Chapter I, we are interested only in the integrated phase effects of the turbulence.

This chapter has described the major components of the experimental setup, namely the shearing interferometer and the turbulence generator. It will be important to remember the orientation of the coordinate system as shown in Figure 3.2. The experimental procedures were also outlined in this chapter. The equation used to estimate the phase structure function without any assumptions about the structure of the turbulence was given (Equation 3.2). The methods used for characterizing the homogeneity and isotropy of the turbulence were also presented.

Chapter IV presents the results from the experiment described in this chapter. A representative sample of the plots used to characterize the turbulence are given; and, observations of the homogeneity and isotropy of the turbulence are made. The remainder of the plots produced from the experimental data are presented in Appendix D. The strength of the turbulence, as quanti-

fied by the index structure function, C_n^2 , is characterized as a function of the turbulence settings.

Chapter IV closes with some observations about the general trends of the phase structure function as a function of the turbulence settings.

IV. Results

In this chapter, the results of the experiment are presented. The first section presents the results of the measurement noise characterization. The sensitivity of the shearing interferometer is estimated from the statistics of the measurement noise. In the second section, the results of the characterization of laboratory generated turbulence are presented. An estimate of the phase structure function is calculated from the acquired wavefront data. Conclusions are then drawn about the isotropy and homogeneity of the generated turbulence using the the estimated phase structure function.

4.1 Noise characterization results

To determine the magnitude of any noise effects within the system, including any noise from the cameras, data is taken with the turbulence turned off. As discussed in Section 3.4.2, a reference wavefront, consisting of the average of 16 realizations, is measured followed immediately by a group of data consisting of 10 wavefront realizations. The reference wavefront phase is then subtracted from each of these 10 wavefront realizations, yielding 10 realizations of $\Delta\phi$, where $\Delta\phi$ is a measure of the phase variations across the aperture. Any variations in the phase values are assumed to be due to measurement noise. Figures 4.1 and 4.2 show two examples of the delta-wavefront phase maps used to characterize the noise. Figure 4.3 shows the histogram of the phase variations, indicating that the noise is approximately a zero mean Gaussian random process with a standard deviation of 7.91×10^{-3} waves. The technique of plotting a histogram of the data as a means of characterizing a random process is used because of its simplicity. More accurate techniques of estimating density functions, such as Parzen windows and the nearest-neighbor rule, are described by Duda and Hart [11]. The sensitivity of the shearing interferometer is calculated by using Equation 3.1 and found to be 0.0237 waves, allowing for a signal-to-noise ratio in the cameras of 3. It should be noted that the sensitivity is measured with the shear set to four pixels in both the x - and y -directions. Thus,

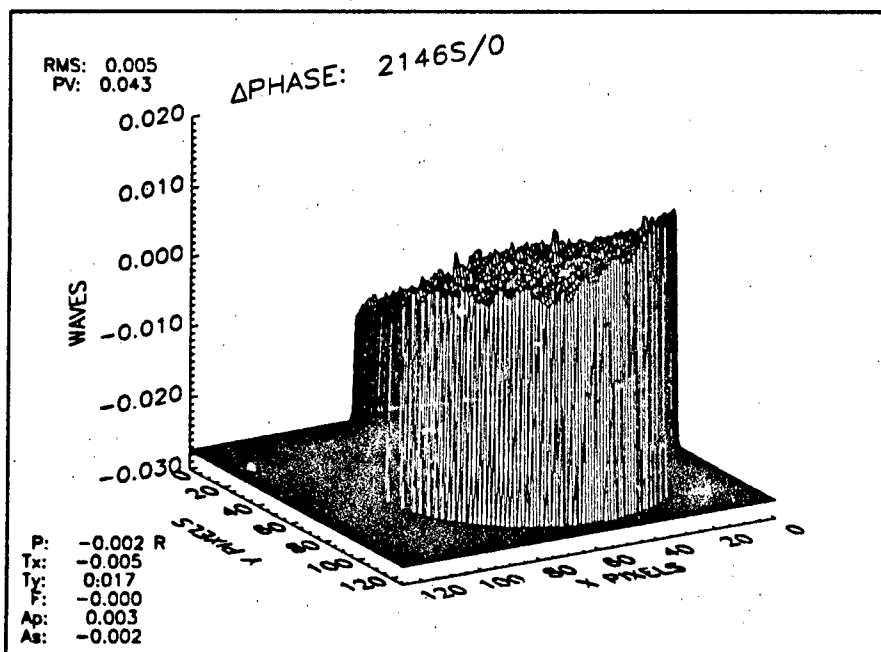


Figure 4.1. Delta phase for 2146, frame 0 (used for noise characterization).

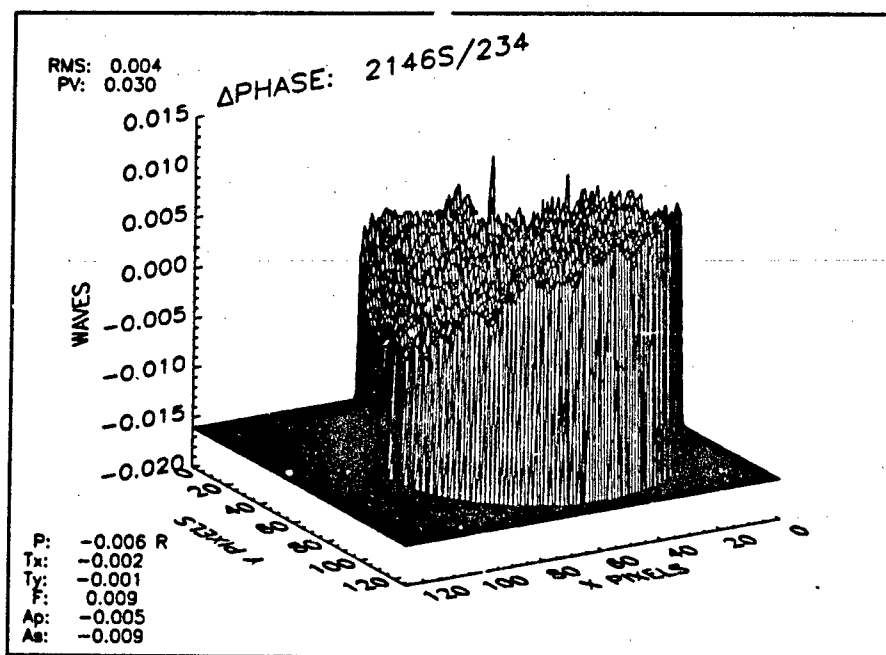


Figure 4.2. Delta phase for 2146, frame 234 (used for noise characterization).

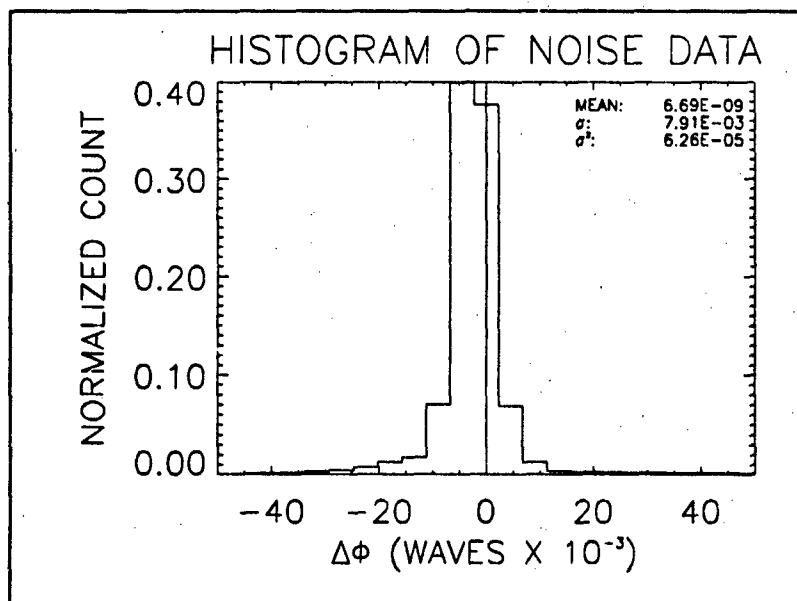


Figure 4.3. Histogram of the phase variations induced by measurement noise.

with four pixels of shear, the shearing interferometer can measure phase values as small as 0.02 waves and phase changes as large as 0.1 waves per pixel.

4.2 Phase structure function results

Characterization of the turbulence is accomplished by estimating the phase structure function as described in Equation 3.2. The design of the turbulence chamber is such that the temperature and the wind speed within the chamber can be controlled. The wind speed is controlled by varying the voltage applied to the fans and the temperature is controlled by varying the voltage applied to the heating element (see Section 3.2). The temperature inside the turbulence chamber is measured with a thermometer, giving an estimate of the average temperature within the chamber. The wind speed within the chamber is not measured directly; however, the fan speed, in rotations per minute, is measured using a calibrated strobe. To help homogenize the turbulence, screens can be placed in the turbulence flow.

Different combinations of the fan voltage and element voltage are used to fully characterize the properties of the turbulence. The structure of the turbulence is also characterized with and without screens placed within the chamber. Acquiring data with different turbulence settings also allows examination of the dependence of the phase structure function on average temperature, as well as wind speed. Table 4.1 summarizes the conditions under which data is acquired as well as identifying the group number for the settings. An estimate of the phase structure function is calculated for each one of the groups listed in Table 4.1 by measuring the phase disturbances induced by the turbulence. Figures 4.4 and 4.5 show example realizations of $\Delta\phi$ used to estimate the phase structure function.

Table 4.1. Test Matrix.

FAN (V)	ELEMENT (V)	SCREENS	T (°C)	FAN SPEED (rpm)	GROUP
20	35	NONE	27	830	2042
20	50	NONE	35	830	2050
20	65	NONE	49	830	2114
20	80	NONE	73	830	2108
20	35	ONE	32	830	2086
20	50	ONE	42	830	2092
20	65	ONE	60	830	2100
20	80	ONE	83	830	2116
35	50	NONE	35	1350	2112
35	65	NONE	44	1350	2068
35	80	NONE	56	1350	2080
24	53	ONE	42	1030	2122
28	55	ONE	42	1160	2124
32	58	ONE	42	1270	2128
36	60	ONE	42	1380	2132
40	61	ONE	42	1475	2138
OFF	OFF	N/A	AMBIENT	N/A	2146

The homogeneity and isotropy of the turbulence for the conditions outlined in Table 4.1 are determined by plotting the phase structure function as discussed in Section 3.4.3. If the phase structure function, $\hat{D}_s(\vec{r}_1, \vec{r}_2)$, is independent of the vector orientation of $\vec{r}_1 - \vec{r}_2$ about a location within the aperture, the turbulence is locally isotropic at that location. If the phase structure function depends only on $\vec{r}_1 - \vec{r}_2$ for all points in the aperture, the turbulence is homogeneous. For

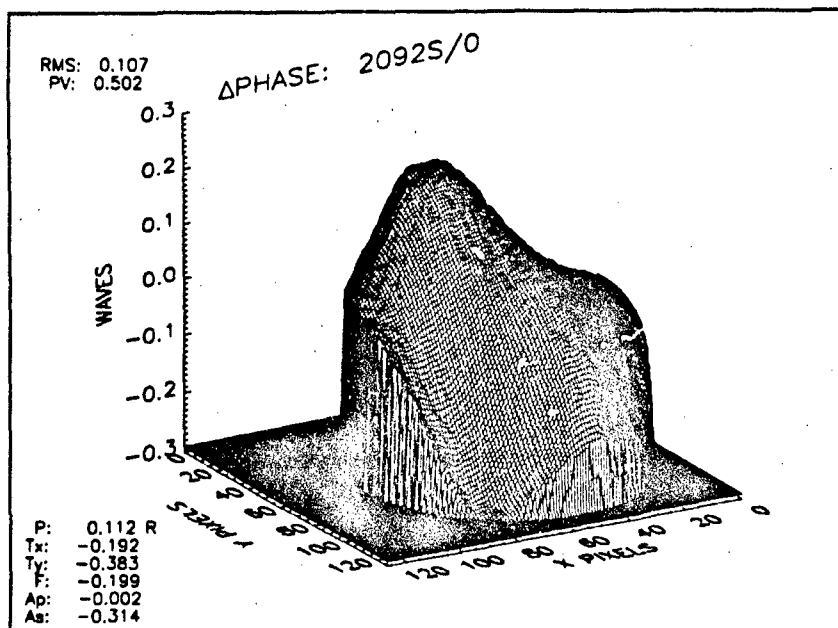


Figure 4.4. Delta phase for 2092, frame 0. The fan voltage is 20 volts; the element voltage is 50 volts; there is one screen in the chamber; the average temperature is 42° C.

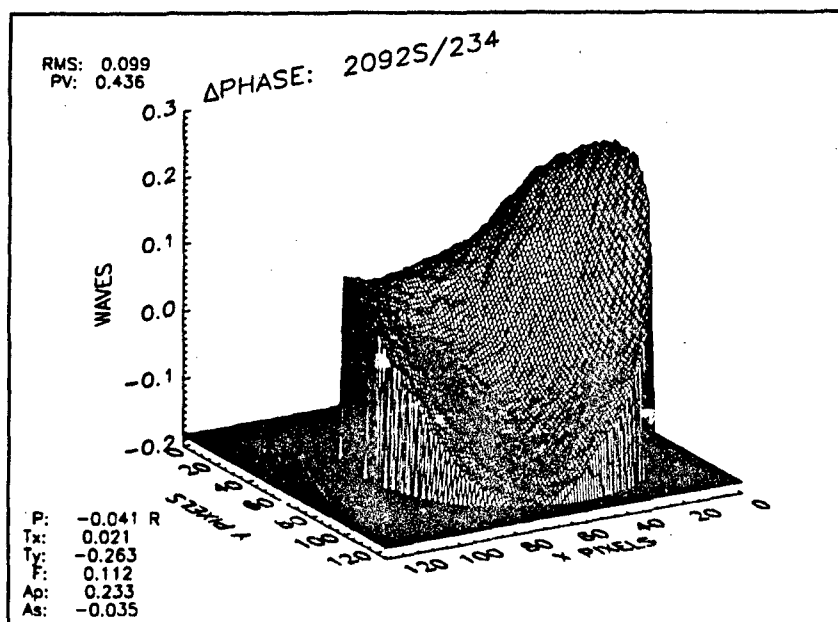


Figure 4.5. Delta phase for 2092, frame 234. The fan voltage is 20 volts; the element voltage is 50 volts; there is one screen in the chamber; the average temperature is 42° C.

turbulence that is both homogeneous and isotropic, the phase structure function depends only on $|\vec{r}_1 - \vec{r}_2|$.

In this section, the functionality of the phase structure function, D_s , is presented for the experimental conditions outlined in Table 4.1. Conclusions about the homogeneity and isotropy are made based on these functional relationships. The effect of the turbulence settings on the inner and outer scale sizes of the turbulence and the index structure constant, C_n^2 , is presented after determining if the generated turbulence is homogeneous and isotropic. The index structure constant is calculated using Equation 2.10. Also presented in this section is the dependence of \hat{D}_s on the wind speed and average temperature within the turbulence chamber. The section concludes with some general observations about the characteristics of the estimated phase structure function.

4.2.1 Isotropy. To test for isotropy, the phase structure function, \hat{D}_s , is plotted versus $|\vec{r}_1 - \vec{r}_2|$. The lines between the two points, \vec{r}_1 and \vec{r}_2 are oriented at 0, 45, -45, and 90 degrees with respect to the x -axis (see Figure 3.14a). A line proportional to $r^{5/3}$ is fitted to the linear portion of the data. It should be noted that determination of isotropy is somewhat subjective—determined by how closely packed the curves of \hat{D}_s are for the four vector orientations. If the $5/3$ slope line matches the trend of the data, implying Kolmogorov turbulence, the mean squared difference between the data and the $r^{5/3}$ line can be used as a relative measure of the isotropy. For the remainder of this thesis, when the term mean squared error is used, it refers to the mean squared error between the $r^{5/3}$ curve and the data. Figures 4.6 and 4.7 show example plots of $\hat{D}_s(r)$ for vectors centered on location 6 of the aperture (see Figure 3.13). These plots are for the data taken at the weakest and the strongest turbulence settings respectively. As can be seen in these figures, the turbulence produced does follow the Kolmogorov $5/3$ power law for a certain range of separations; therefore, the mean squared error is used as a quantitative measure of the isotropy.

A comparison of the mean squared error to the magnitude of the phase structure function in Figures 4.6 and 4.7 indicates that the turbulence appears to be locally isotropic at the center

of the aperture for both settings. Figure 4.6 shows $\hat{D}_s(r)$ for 2042. The turbulence settings for group 2042 are: 20 volt fan voltage; 35 volt element voltage; no screens; and 27°C temperature. The magnitude of the phase structure function over the range of values for r that $\hat{D}_s(r)$ follows the 5/3 slope line ranges from 10^{-4} to 10^{-1} while the mean squared error is on the order of 10^{-6} . The mean squared error is at least two orders of magnitude below the values of \hat{D}_s . Figure 4.7 shows $\hat{D}_s(r)$ for 2116. The turbulence settings for group 2116 are: 20 volt fan voltage; 80 volt element voltage; one screen; and 83°C temperature. The magnitude of the phase structure function over the range of values for r that $\hat{D}_s(r)$ follows the 5/3 slope line ranges from 10^{-1} to 10^{+1} while the mean squared error is on the order of 10^{-1} . The mean squared error is approximately one order of magnitude below the values of \hat{D}_s . Figure 4.7 shows that the degree of isotropy tends to decrease as the strength of turbulence increases.

Figures 4.8 and 4.9 shows a plots of $\hat{D}_s(r)$ for vectors centered on location 6 of the aperture for groups 2114 and 2092. The settings for these two groups are approximately the same in terms of average temperature within the chamber. The only difference between the conditions for 2114 and group 2092 is that for group 2114, a screen is not used; and, for group 2092, a screen is used (see Table 4.1). The screen that is used consists of a wire mesh of about 20 squares per inch. This wire mesh is placed on both sides of a frame that is inserted into the chamber so as to break up the flow of air (see Figures 3.2 and C.8). One effect of placing this screen in the chamber is to raise the average temperature within the chamber, most likely due to the restriction of airflow caused by the screen. From Figures 4.8 and 4.9 it can be seen that placing this screen in the chamber has a minimal effect on the isotropy of the turbulence.

Plots like those shown in Figures 4.6-4.9 are generated for each location in the aperture yielding similar results. Figures 4.10 and 4.11 show example plots of $D_s(r)$ for group 2092 at the remaining points in the aperture. As can be seen in these plots, the generated turbulence exhibits the properties of locally isotropic turbulence at all locations within the aperture; thus, the generated

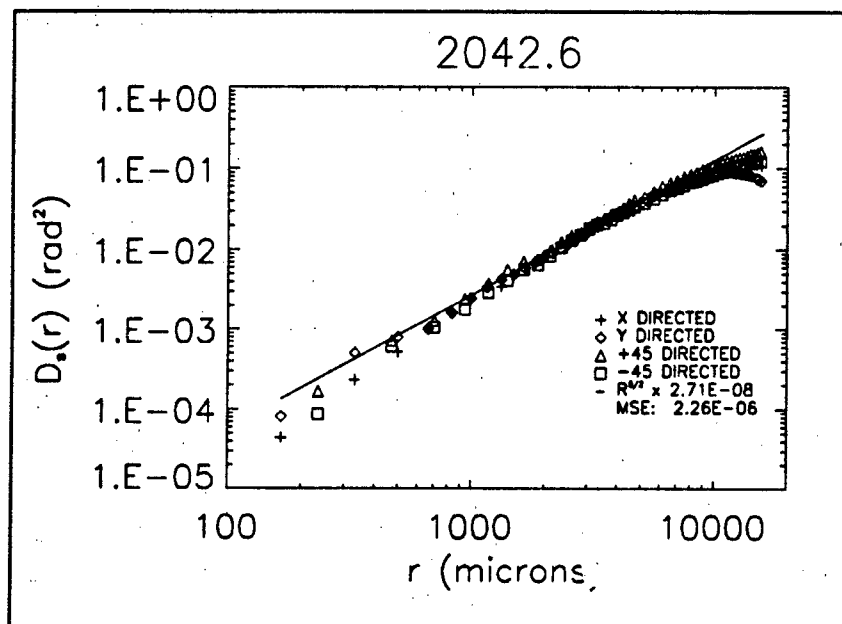


Figure 4.6. $\hat{D}_s(r)$ for 2042, location 6. The fan voltage is 20 volts; the element voltage is 35 volts; there is no screen in the chamber; the average temperature is 27° C.

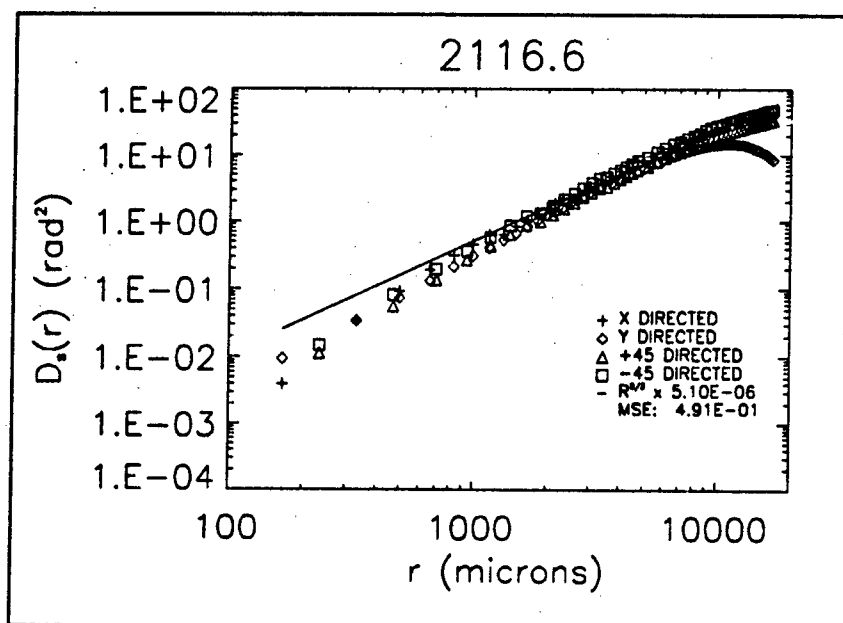


Figure 4.7. $\hat{D}_s(r)$ for 2116, location 6. The fan voltage is 20 volts; the element voltage is 80 volts; there is one screen in the chamber; the average temperature is 83° C.

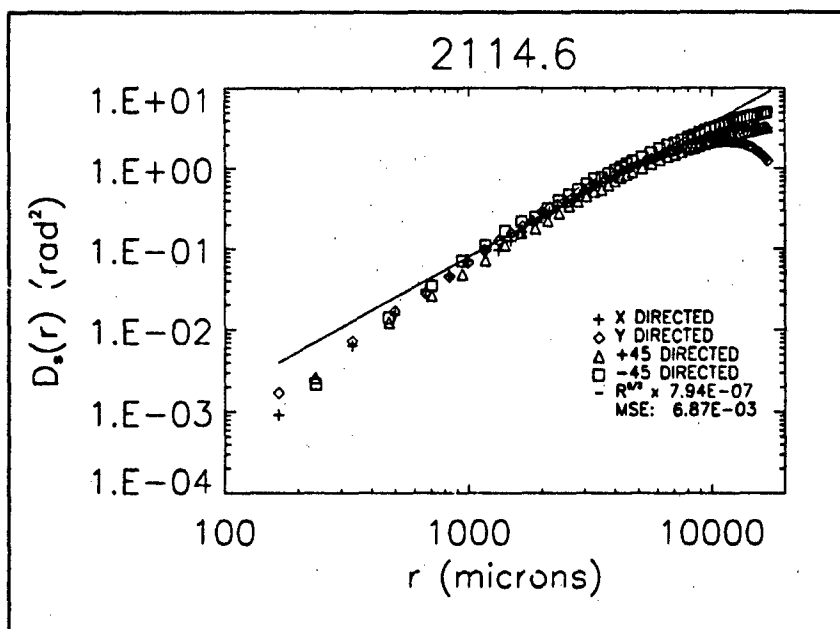


Figure 4.8. $\hat{D}_s(r)$ for 2114, location 6. The fan voltage is 20 volts; the element voltage is 65 volts; there is no screen in the chamber; the average temperature is 49° C.

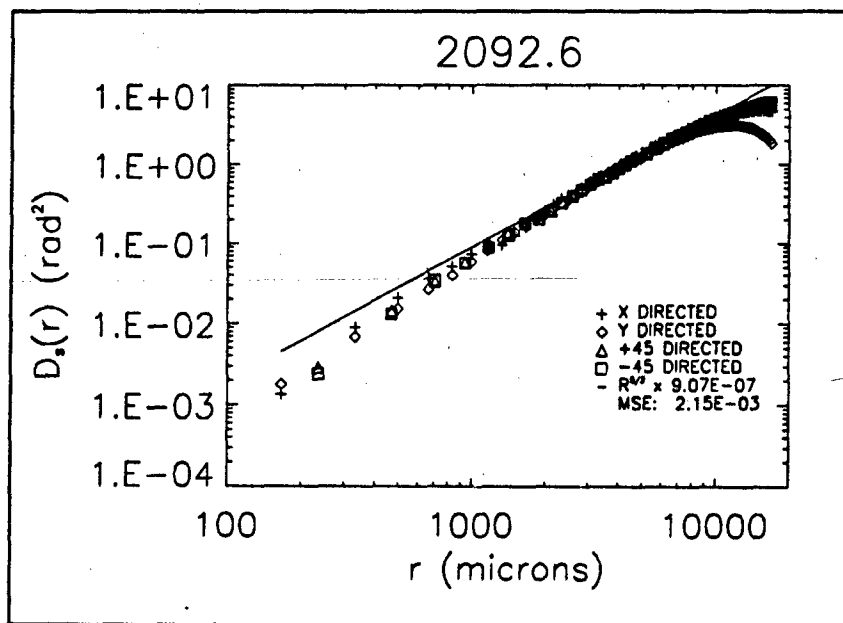


Figure 4.9. $\hat{D}_s(r)$ for 2092, location 6 test for isotropy. The fan voltage is 20 volts; the element voltage is 50 volts; there is one screen in the chamber; the average temperature is 42° C.

turbulence appears to be isotropic. Note also on these plots that the magnitude of \hat{D}_s is relatively constant across the aperture. The remainder of the isotropy plots, included in Appendix D, show that the turbulence appears to be somewhat isotropic for all the settings of turbulence outlined in Table 4.1.

4.2.2 Homogeneity. To test for homogeneity, the value of the phase structure function, \hat{D}_s , is plotted versus r , for vectors having the same orientation, $\vec{r}_1 - \vec{r}_2$, and different locations. The value of $\hat{D}_s(\vec{r})$ is compared by location of the vector \vec{r} within the aperture (see Figure 3.14b). Figure 4.12 shows the plots for group 2042; the fan setting is 20 volts; the element voltage is 35 volts; no screen is placed in the turbulent flow; and the average temperature is 26° C. Figure 4.12 shows four plots, one for each vector orientation. Again, because the phase structure function follows the 5/3 slope line, indicating Kolmogorov type turbulence, the mean squared difference between the phase structure function data and the $r^{5/3}$ line is used as a quantitative measure of the homogeneity. Figure 4.13 shows the homogeneity plots for group 2116; the fan setting is 20 volts; the element voltage is 80 volts; one screen is placed in the turbulent flow; and the average temperature is 83° C. Figures 4.12 and 4.13 are plots for the data acquired at the weakest and strongest turbulence settings respectively. From the plots it can be seen that the generated turbulence appears to be homogeneous. Also shown in the plots is that the mean squared error, as compared to the magnitude of \hat{D}_s , seems to increase as the temperature within the chamber increases, indicating that the turbulence is becoming less homogeneous. The decrease in homogeneity with increase in turbulence strength tends to hold for all the data groups. The remaining plots used to test for homogeneity, included in Appendix D, also indicate that the generated turbulence appears to be homogeneous for all settings.

As mentioned in Section 3.2, a screen can be placed in the turbulence chamber to help break up the flow and homogenize the turbulence; however, an increase in the homogeneity of the turbulence is not evidenced in the data. Figures 4.14 and 4.15 show example plots of $D_s(r)$ for data acquired

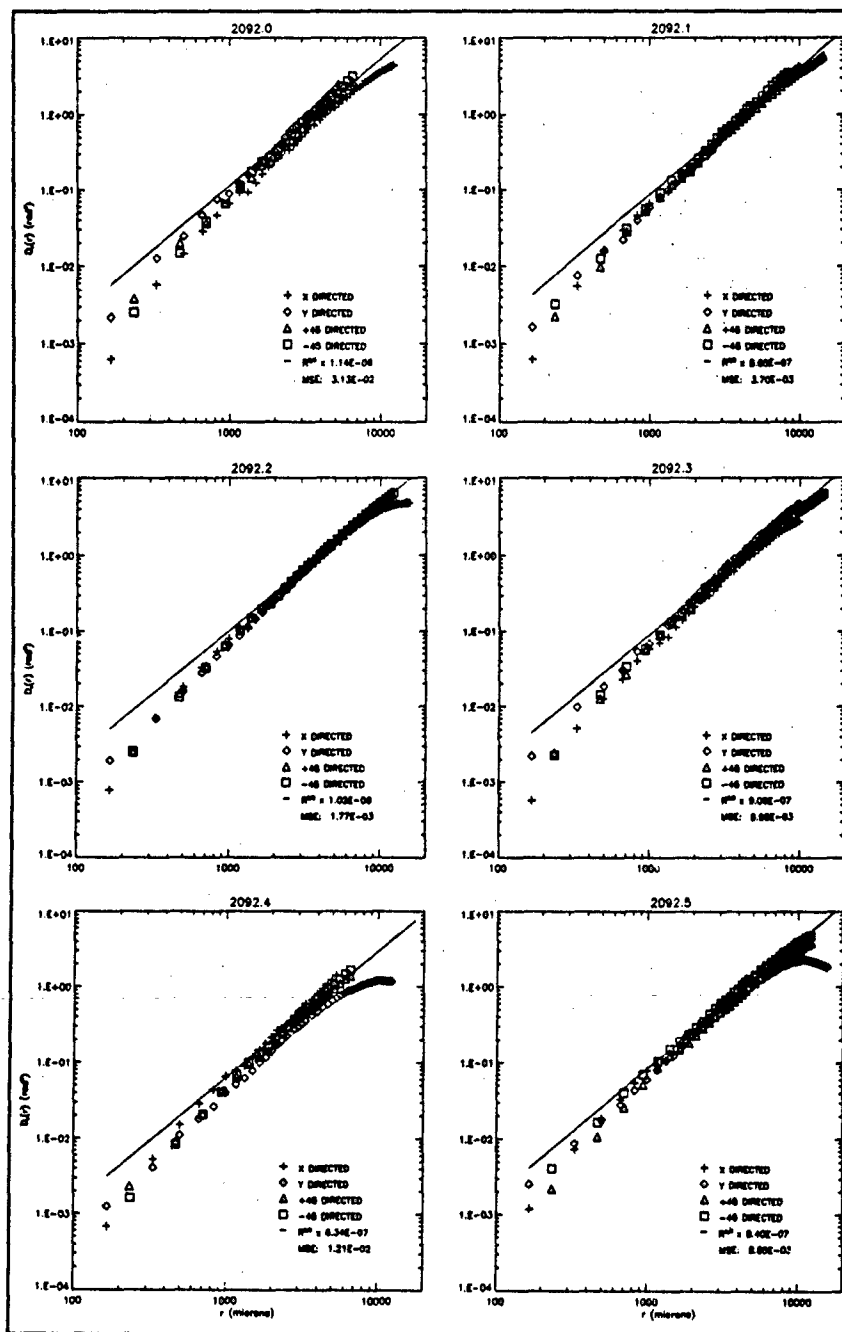


Figure 4.10. $\hat{D}_s(r)$ for 2092, locations 0 - 5. The fan voltage is 20 volts; the element voltage is 50 volts; there is one screen in the chamber; the average temperature is 42° C.

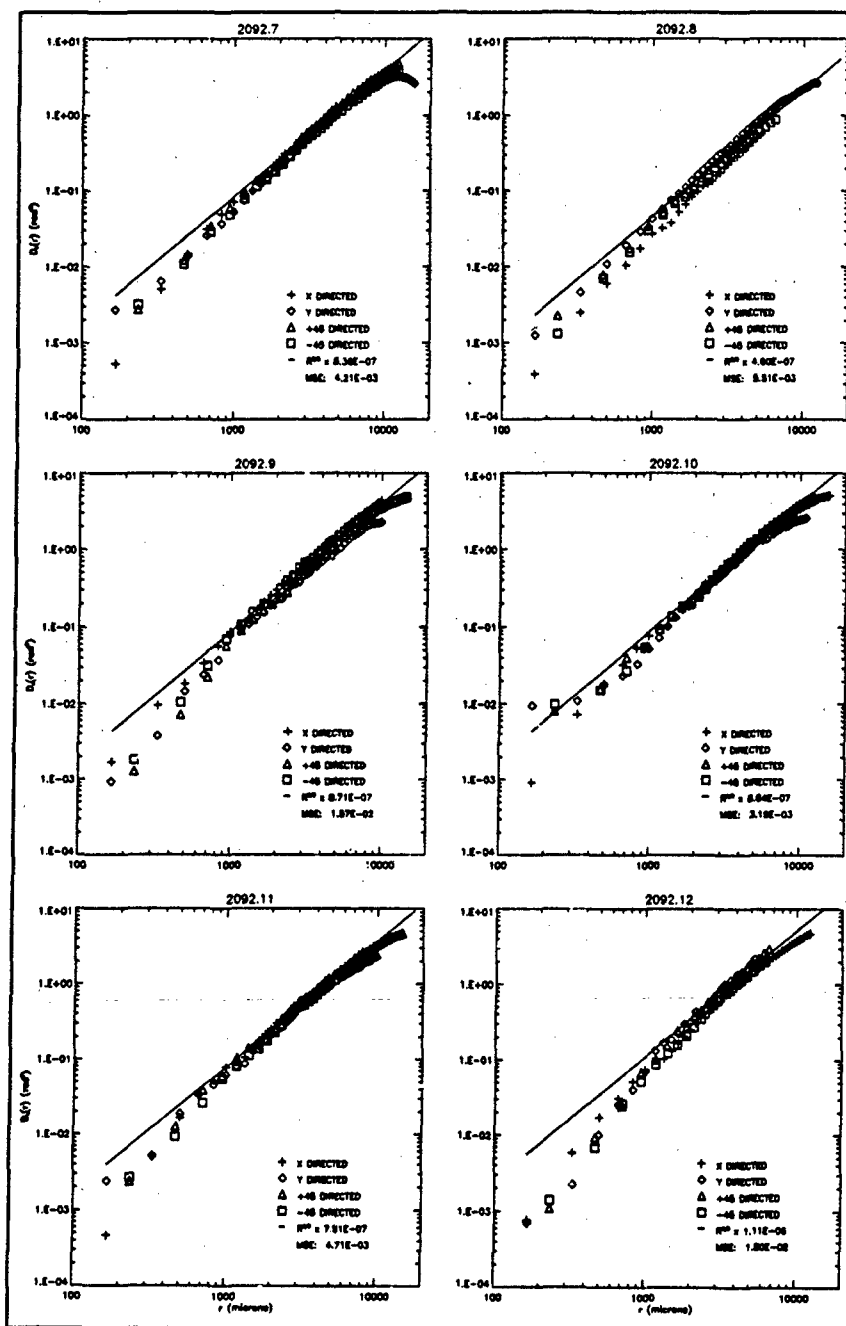


Figure 4.11. $\bar{D}_s(r)$ for 2092, locations 7 - 12. The fan voltage is 20 volts; the element voltage is 50 volts; there is one screen in the chamber; the average temperature is 42° C.

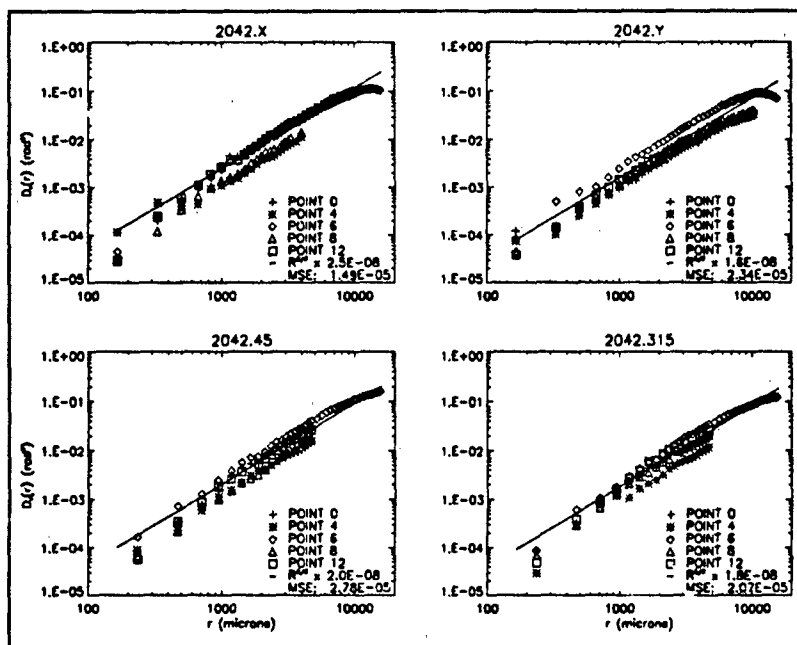


Figure 4.12. $\hat{D}_s(r)$ for 2042. The fan voltage is 20 volts; the element voltage is 35 volts; there is no screen in the chamber; the average temperature is 27° C.

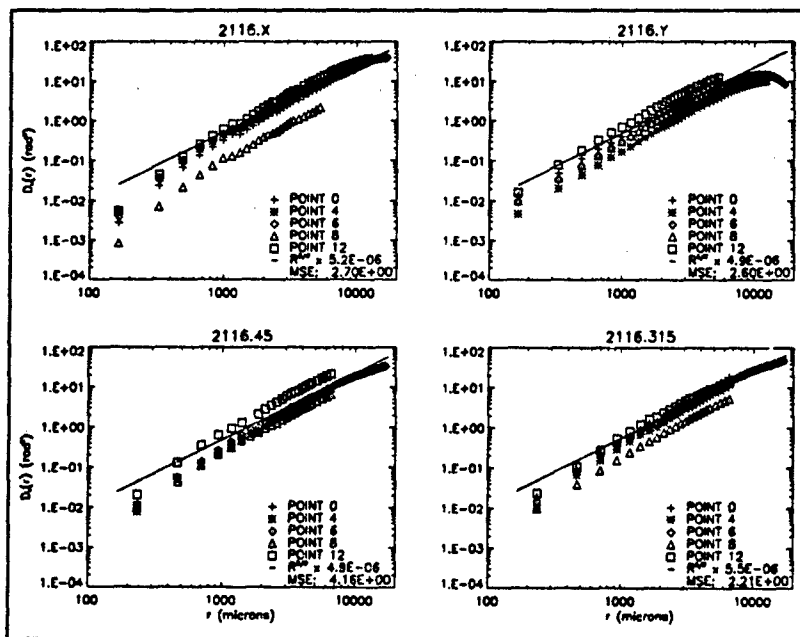


Figure 4.13. $\hat{D}_s(r)$ for 2116. The fan voltage is 20 volts; the element voltage is 80 volts; there is one screen in the chamber; the average temperature is 83° C.

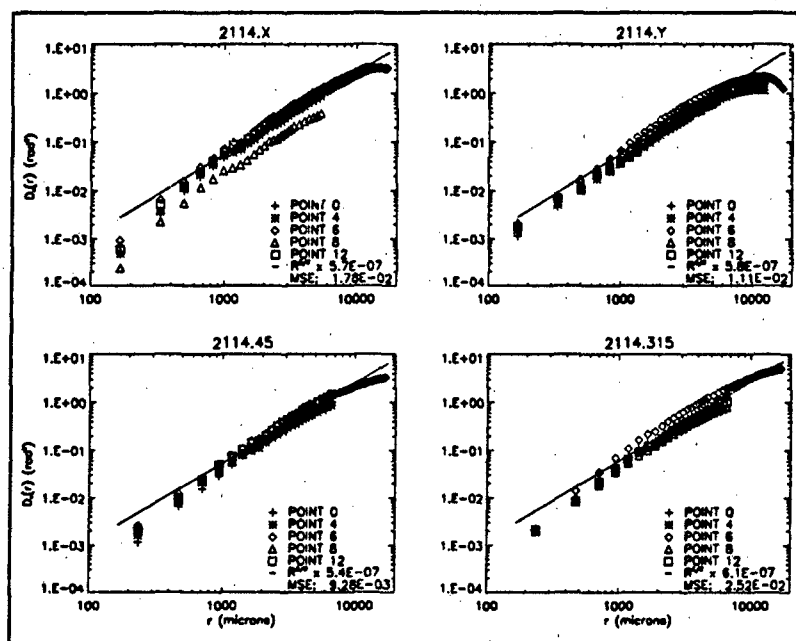


Figure 4.14. $\hat{D}_s(r)$ for 2114. The fan voltage is 20 volts; the element voltage is 65 volts; there is no screen in the chamber; the average temperature is 49° C.

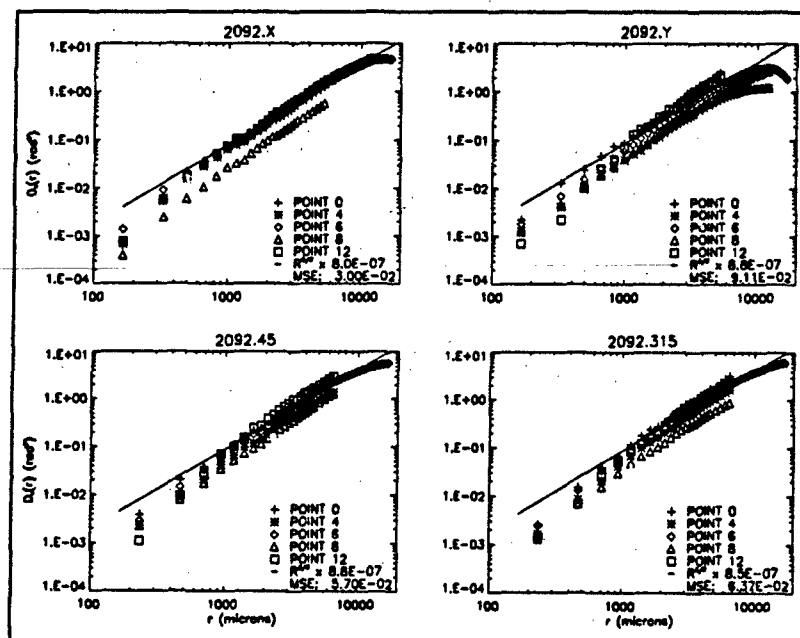


Figure 4.15. $\hat{D}_s(r)$ for 2092. The fan voltage is 20 volts; the element voltage is 50 volts; there is one screen in the chamber; the average temperature is 42° C.

at approximately the same turbulence settings; however, group 2092 is acquired with a screen in the chamber and group 2114 is acquired without the screen. Placing the screen in the chamber appears to have minimal effect on the homogeneity of the turbulence, as can be seen by comparing the plots from the Figures 4.14 and 4.15.

4.2.3 Inertial subrange. The value of the phase structure function, \hat{D}_s , appears to be independent of vector orientation and location; thus, the turbulence is approximately homogeneous and isotropic. Figure 4.16 shows an example plot of the phase structure function versus r for all vector locations and orientations. Estimates of the inner and outer scales of the turbulence, as well as a calculation of the index structure constant, C_n^2 , can be determined from the plots of $\hat{D}_s(r)$. The index structure constant is calculated by fitting a 5/3 slope line, on a log-log scale, to the linear portion of the data. The coefficient of the $r^{5/3}$ curve that minimizes the mean squared error between the curve and the data is related to the index structure constant by Equation 2.10. From the calculated value of C_n^2 , a value for the Fried seeing-cell size, r_o , is calculated using Equation 2.14. The inner and outer scales are estimated by qualitatively determining, from the plots of $\hat{D}_s(r)$, where the phase structure function no longer follows the Kolmogorov 5/3 power relationship. The range of values of r between the inner and outer scale is defined as the inertial subrange. Table 4.2 gives the values of the inner and outer scales, C_n^2 , r_o , and the average mean squared phase variations induced by the turbulence for each data group. The average mean squared phase variation is denoted by

$$\overline{(\Delta\phi^2)}, \quad (4.1)$$

where the over-line indicates an average over the aperture and $\langle \cdot \rangle$ indicates an ensemble average. Because the phase variations induced by the turbulence appear to be zero mean, as shown in Figure 4.17, $\overline{(\Delta\phi^2)}$ can be estimated by averaging the variance of the phase deviations. Again, the remaining plots used to calculate C_n^2 and the inner and outer scales of the turbulence are included in Appendix D.

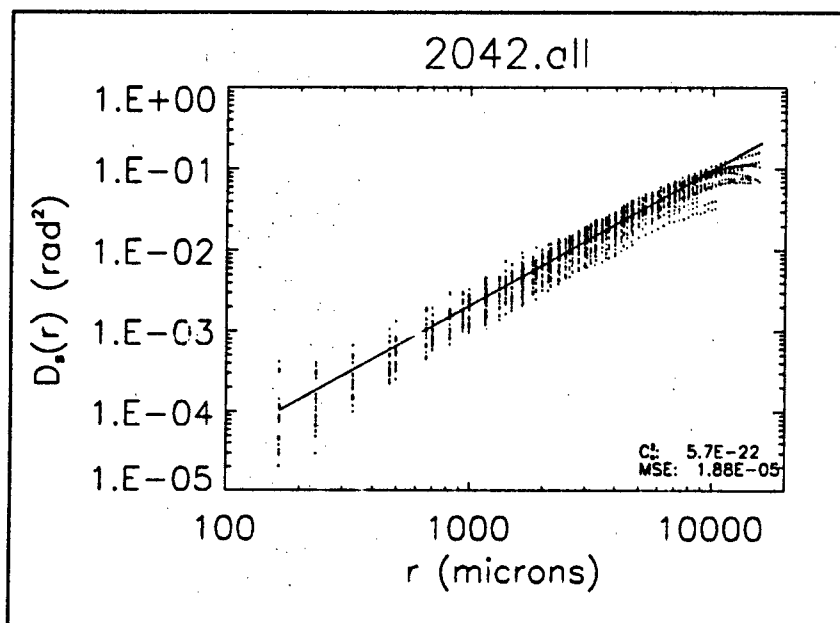


Figure 4.16. $\hat{D}_s(r)$ for 2042. The fan voltage is 20 volts; the element voltage is 35 volts; there is no screen in the chamber; the average temperature is 27° C.

Table 4.2. Test Results. The turbulence settings are indicated under the SETTINGS column and numbers in the column indicate fan voltage, element voltage, number of screens and temperature respectively.

GROUP	SETTINGS	C_n^2 (m ^{-2/3})	r_o (cm)	l_o (μm)	L_o (μm)	$\langle \Delta \phi^2 \rangle$ (rad ²)
2042	20/35/0/27°C	5.7×10^{-12}	13.0	400	9000	0.02
2050	20/50/0/35°C	2.3×10^{-11}	5.6	600	9000	0.09
2114	20/65/0/49°C	1.7×10^{-10}	1.7	800	9000	0.77
2108	20/80/0/73°C	4.2×10^{-10}	1.0	950	9000	1.39
2086	20/35/1/32°C	1.2×10^{-10}	2.1	900	8000	0.33
2092	20/50/1/42°C	2.4×10^{-10}	1.4	1000	1000	0.88
2100	20/65/1/60°C	6.6×10^{-10}	0.7	1000	9000	1.63
2116	20/80/1/83°C	1.4×10^{-09}	0.5	1000	10000	3.56
2112	35/50/0/35°C	5.0×10^{-11}	3.5	850	9000	0.13
2068	35/65/0/44°C	8.5×10^{-11}	2.6	700	8000	0.31
2080	35/80/0/56°C	2.4×10^{-10}	1.4	900	9000	0.74
2122	20/53/1/42°C	2.7×10^{-10}	1.3	1000	10000	1.04
2124	20/55/1/42°C	3.1×10^{-10}	1.2	1000	9000	1.05
2128	20/58/1/42°C	2.2×10^{-10}	1.4	800	10000	0.92
2132	20/60/1/42°C	2.7×10^{-10}	1.3	1000	9000	0.97
2138	20/61/1/42°C	2.6×10^{-10}	1.3	900	9000	1.04

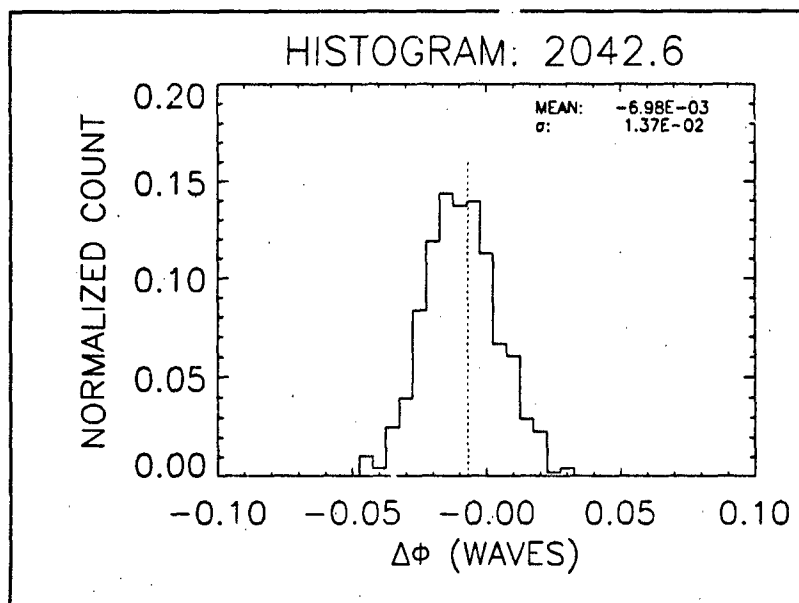


Figure 4.17. Histogram of the phase variations induced by turbulence for group 2042, location 6. The fan voltage is 20 volts; the element voltage is 35 volts; the average temperature is 27° C.

4.2.4 Dependence of \hat{D}_s on temperature and wind speed. The strength of the turbulence, as quantified by the index structure constant, increases as the average temperature within the chamber increases, as can be seen in Table 4.2. Figure 4.18 shows a plot of C_n^2 as a function of temperature. The increase in C_n^2 with increase in temperature is not surprising since the index of refraction variations also increase with temperature. The dependence of C_n^2 on fan speed is realized by comparing the index structure constant for groups 2092, 2122, 2124, 2128, 2132, and 2138. As shown in Table 4.2, the index structure constant appears to be relatively independent of the wind velocity. This phenomena is known as Taylor's "frozen flow" hypothesis [30]. If the exposure time is fast compared to the wind induced variations, the wind will not affect the phase structure function. The average value of C_n^2 for groups 2092, 2122, 2124, 2128, 2132, and 2138 is $2.6 \times 10^{-10} \text{m}^{-2/3}$ with a standard deviation of $3.06 \times 10^{-11} \text{m}^{-2/3}$.

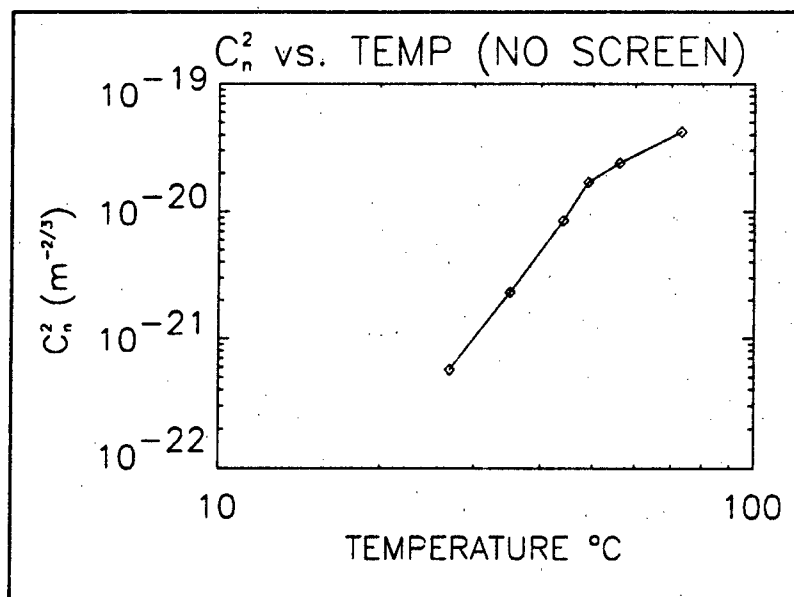


Figure 4.18. Index structure constant, C_n^2 , versus average temperature within the chamber.

4.3 Observations

In this section, some of the general trends of $\hat{D}_s(r)$ as a function of the turbulence settings are discussed. As mentioned in the previous sections, the generated turbulence exhibits the characteristics of homogeneous and isotropic turbulence for all the settings tested. However, there seems to be a trend of decreasing homogeneity and isotropy as the temperature within the chamber is increased. This apparent decrease in homogeneity and isotropy could be due to the non-uniform heating of the heating element used to create the temperature variations. The element used is a coil of wires arranged in a spiral pattern. When the temperature of the coils is hot enough that the element turns red, it becomes obvious that the element temperature is higher toward the center of the spiral pattern. This non-uniform heating of the element creates turbulence that has non-uniform index of refraction variations across the chamber.

Another trend that is obvious in the data, and generally present for all settings of turbulence, is that the magnitude of the phase structure function for vectors in the y -direction tends to decrease

at large separations, r . Theory predicts that the phase structure function should level and remain constant for values of separation greater than the outer scale of the turbulence, L_o . In light of Equation 3.3, this trend indicates that either the mean squared value of the phase deviations decreases near the edges of the aperture in the turbulence flow direction, or that the correlation of the phase at opposite edges of the aperture increases. The former implies that the turbulence is not homogeneous in the flow direction for separations on the order of the aperture size. The latter implies that the phase deviations at the edges of the aperture are correlated in some way. The most probable case is that of the mean squared value of the phase deviations decreasing near the edges of the aperture, implying that the turbulence is not homogeneous at the edges of the aperture in the direction of turbulence flow.

Theory predicts that for Kolmogorov type turbulence that is homogeneous and isotropic, the phase structure function will be proportional to $r^{5/3}$ for values of r between l_o and L_o , the inertial subrange. For values of r less than l_o , the phase structure function will follow an r^2 power relationship. Plots of the phase structure function indicate that the turbulence does follow the Kolmogorov 5/3 power law relationship within a range of values of r . Although the actual slope has not been estimated for values of r less than the inner scale, the data does indicate that the slope of the phase structure function, on a log-log, does decrease from the 5/3 slope for values of r less than the inner scale.

As shown in Table 4.2 the values of C_n^2 range in magnitude from 10^{-12} to $10^{-9} \text{m}^{-2/3}$. The corresponding values of r_o range from 13.0 to 0.5 cm. The values of C_n^2 are approximately 4 to 5 orders of magnitude larger than typical C_n^2 values for the atmosphere. However, because the propagation path length for the turbulence chamber is much smaller than the propagation path length within atmospheric turbulence, in order to realize the same type of effects as atmospheric turbulence, the turbulence chamber must create stronger turbulence.

V. Conclusions

A unique method of measuring the effects of laboratory generated turbulence on optical imaging has been developed. Direct measurements of optical wavefront phase are made using a wavefront sensor; and, from these measurements, an estimate of the phase structure function is calculated. The estimate of the phase structure function is calculated in such a manner as to eliminate any assumptions about the structure of the turbulence. Because the phase structure function is directly related to the average OTF of the optical system, the need to infer system performance characteristics from other measurements is eliminated.

The measurement noise associated with the shearing interferometer was characterized. The sensitivity of the SI was found to be approximately 0.0237 waves, allowing for a signal-to-noise ratio in the cameras of 3. Thus, with the shear distance set at 4 pixels in both the x - and y -directions, the shearing interferometer can sense phase values as small as 0.0237 and phase changes as large as 0.1 waves per pixel.

A turbulence generator has been designed and built to aid in the characterization of current adaptive optics and image enhancement techniques, as well as the development of new image enhancement techniques. The generated turbulence has been characterized using the unique method of directly measuring the wavefront phase perturbations induced by the turbulence. The characteristics of the turbulence has been found to match reasonably well with those of the Earth's atmosphere. Determinations of homogeneity and isotropy were made by observing the functional dependence of the phase structure function on the magnitude, orientation, and location of the vector $\vec{r}_1 - \vec{r}_2$. Plots of the estimated phase structure function, $\hat{D}_s(\vec{r}_1 - \vec{r}_2)$, indicate that the generated turbulence is reasonably homogeneous and isotropic. The plots also show that the phase structure function is proportional to $|\vec{r}_1 - \vec{r}_2|^{5/3}$ for a certain range of values, indicating Kolmogorov-type turbulence. Estimates of the index structure constant, which is often used to describe the strength of the turbulence, range in magnitude from 10^{-12} to 10^{-9} meters $^{-2/3}$. The corresponding values

of the Fried seeing-cell size, r_o , range from 13.0 to 0.5 cm. The turbulence strengths are 4 to 5 orders of magnitude larger than typical values of C_n^2 for atmospheric turbulence. The inner scale, as estimated from the plots of \hat{D}_s , ranges between 400 and 1000 micrometers and the outer scale ranges between 8 and 10 millimeters, depending on the turbulence settings. Average mean squared phase variations range between 0.02 and 3.56 square radians.

The turbulence generator designed and characterized for this project provides the Air Force Institute of Technology (AFIT) with the capability to test current and future adaptive optics and image enhancement techniques in a controlled laboratory environment. The turbulence chamber also provides a tool to aid in the understanding of turbulence effects on all electromagnetic propagation.

Appendix A. Shearing Interferometer

There are several different types of shearing interferometers. The principal concept is that the wavefront to be tested is interfered with a spatially shifted or sheared version of itself forming a pattern of fringes that are proportional to the slope of the wavefront in the direction of shear. This spatial shift can be created several different ways. Some examples are:

- Lateral shear - the replica is laterally displaced relative to the original.
- Radial shear - the original is interfered with a scaled replica.
- Rotational shear - the replica is rotated some angle relative to the original.
- Folded shear - the replica is inverted about some axis relative to the original.

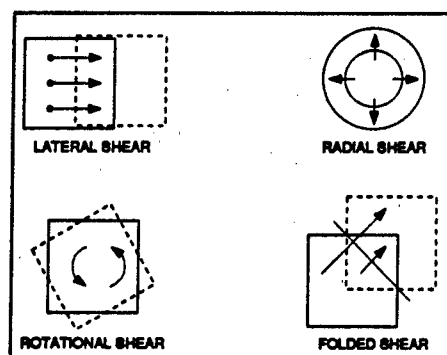


Figure A.1. Types of Shearing Interferometers.

This appendix will concentrate on the lateral shearing interferometer (SI). For discussions and descriptions of the other types of shearing interferometers, see, for example, [9, 24, 44].

A.1 Introduction to the lateral shearing interferometer

The first lateral shearing interferometers were developed by Lenouvel and Lenouvel in 1938, Bates in 1947, and Hariharan and Sen in 1960 [24]. The Lenouvel and Lenouvel SI was based on the Michelson interferometer, the Bates SI was a modification of the Mach-Zehnder interferometer,

while the Hariharan and Sen SI was based on the Sagnac interferometer. These three shearing interferometers could only be used with converging wavefronts. Several modifications to these interferometers for use with spherical and planar wavefronts are discussed by Murty [37].

There are several applications of the SI. Because the shape of a wavefront is a function of the optical element producing it, the SI can be applied to the testing of optical systems and components (lenses and mirrors) for determining performance. Thus, the shapes of mirror surfaces and aberrations of lenses can be obtained from the measurement of wavefront phase or shape. Shearing interferometry has also been applied to the high speed measurements of optical beams transmitted through the atmosphere and diagnostic measurement of laser systems [23]. An SI can also be used to directly measure the Optical Transfer Function (OTF) of a system. The method for obtaining the OTF from SI measurements is described by Hariharan [24]. Other applications of shearing interferometry are described in detail by Bryngdahl [9].

The primary advantage of a SI is that the wavefront is interfered with itself, thus eliminating the need for a separate reference wavefront. Because the interfering beams travel nearly identical paths, the problems of vibration and turbulence inherent in other interferometers are significantly reduced. Another advantage is that a SI can be configured to operate with broadband or "white light" sources [37]. The SI provides linear wavefront measurements over a large dynamic range which makes it valuable in measuring steep aspherics. A major disadvantage of the SI is that the interference pattern formed is not directly related to the wavefront shape, as is the case when a separate reference wavefront is used. Because the fringe pattern is proportional to the slope of the wavefront in the direction of shear, the shearing interferometer can only measure wavefront slope over small sections of the wavefront. These slopes must be pieced together or reconstructed to obtain the actual wavefront. In order to fully characterize the wavefront with a lateral SI, two interferograms with mutually perpendicular shear directions must be used.

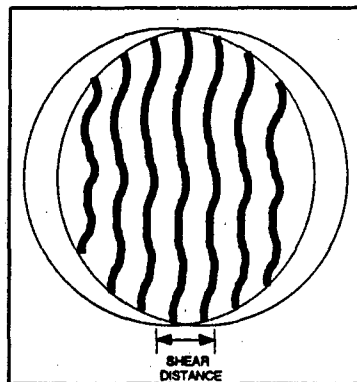


Figure A.2. Overlap fringes in a Shearing Interferometer.

A.2 Theory of lateral shearing interferometer

In a lateral shearing interferometer (SI), a pattern of fringes is formed by interfering a beam with a spatially shifted version of itself; fringes are produced in the overlap region (see Figure A.2). This section discusses the mathematics associated with the formation of the fringe pattern shown in Figure A.2. This description is independent of the method by which the lateral shear is produced. The analysis is also limited to a shear in the x -direction; the analysis for the y -direction is identical.

Let the complex amplitude, $\Phi(x, y)$, of the wavefront entering the SI be described by:

$$\Phi(x, y) = A(x, y) \exp^{j\phi(x, y)}, \quad (\text{A.1})$$

where $A(x, y)$ is the amplitude, $\Phi(x, y)$ is the phase, and x and y are spatial coordinates. A spatially shifted—in the x direction—version of the complex amplitude of this wave is described as:

$$\Phi(x + \Delta x, y) = A(x + \Delta x, y) \exp^{j\phi(x + \Delta x, y)}, \quad (\text{A.2})$$

where Δx is the shear distance. Then the fringe pattern formed by the interference of the fields described in Equations A.1 and A.2 is given by the squared magnitude of the sum of the amplitudes:

$$|\Phi(x, y) + \Phi(x + \Delta x, y)|^2 = 2A^2 [1 + \cos(\Delta\phi)], \quad (\text{A.3})$$

where

$$\Delta\phi = \phi(x, y) - \phi(x + \Delta x, y). \quad (\text{A.4})$$

It can be shown [8] that for small values of Δx , the phase of the interference fringes, within a scale factor, at any point is given by:

$$\Delta\phi = \frac{\partial\phi}{\partial x} \Delta x. \quad (\text{A.5})$$

Thus, apart from the scale factor, the analysis of the wavefront is reduced to extracting $\Delta\phi$ from a signal of the form:

$$I_1 = 1 + \cos \Delta\phi. \quad (\text{A.6})$$

If phase retardations corresponding to $\frac{\lambda}{3}$ and $\frac{2\lambda}{3}$ can be introduced into the field of Equation A.6, the intensities would become:

$$I_2 = 1 + \cos \left(\Delta\phi + \frac{2\pi}{3} \right), \quad (\text{A.7})$$

and

$$I_3 = 1 + \cos \left(\Delta\phi + \frac{4\pi}{3} \right), \quad (\text{A.8})$$

respectively. Thus $\Delta\phi$ can be found by manipulating Equations A.6 - A.8 yielding:

$$\Delta\phi = \tan^{-1} \left(\frac{I_3 - I_2}{I_1 - I_2} \right). \quad (\text{A.9})$$

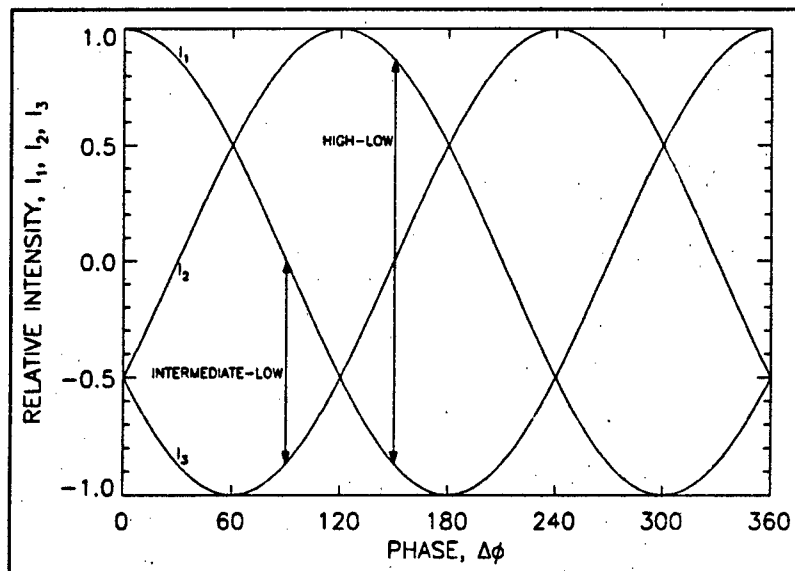


Figure A.3. Hexflash method.

Due to the difficulties associated with calculating the arctangent, some algorithm must be used that will yield unambiguous results. Such an algorithm has been developed in an independent research program and is called hexflash phase analysis [43]. A brief description of this algorithm follows.

The three signals described by Equations A.6 – A.8 are shown in Figure A.3, where intensity, I , is plotted on the y -axis and phase, $\Delta\phi$ on the x -axis. Note that in any 60 degree interval the difference between the highest and lowest signal is approximately constant, and the difference between the intermediate and lowest signal ranges from 0 to 1. There is thus a one to one correspondence between the intensity measurements:

$$\frac{\text{intermediate} - \text{low}}{\text{high} - \text{low}}, \quad (\text{A.10})$$

and the value of the phase, modulo 60 degrees. By observing which permutation of I_1 , I_2 , and I_3 , gives highest, intermediate, and lowest intensities, the 60 degree interval to assign the phase is

known. The phase then is a function:

$$\Delta\phi = F \left(\frac{\text{intermediate} - \text{low}}{\text{high} - \text{low}} \right) + N \times 60^\circ, \quad (\text{A.11})$$

where N is the permutation number. This functionality is implemented in software whose output then yields $\Delta\phi$, the phase difference between points on the wavefront defined in Equation A.4. This phase difference is calculated for all pixel locations, (x, y) , in the aperture. The array of phase differences, or slope measurements, is then reconstructed to form a phase map. Reconstruction techniques and an analysis of their performance are discussed by Rimmer [41], Fried [13], and Hudgin [25, 26], for example.

For general shear distances the phase difference $\Delta\phi$ is given to the first order by:

$$\Delta\phi(x, y) = \frac{\partial\Phi}{\partial x} \Delta x + \frac{\partial\Phi}{\partial y} \Delta y, \quad (\text{A.12})$$

where Δx and Δy are the x - and y -shear in one leg of the interferometer. In the x -leg of the interferometer, the y -shear is set to $\Delta y = 0$. What nonzero value to set Δx to is determined by practical considerations. A larger shear induced into the beam tends to increase the signal, and the sensitivity to small values of $\partial\Phi/\partial x$, at the cost of dynamic range. Small shears induced in the beam will increase the amount of phase variations over the aperture that can be sensed, at the cost of decreased sensitivity. Thus, when setting the shear distance to be used, a tradeoff must be considered; use a small shear to sense large $\partial\Phi/\partial x$, and a large shear to sense small $\partial\Phi/\partial x$.

A.3 Description of the SI used in the experiment

A diagram of the shearing interferometer located at AFIT's Atmospheric and Adaptive Optics Laboratory is shown in Figure A.4. This SI is used to experimentally reconstruct the phase of an optical wavefront subjected to a random disturbance. The imaging optics at the front end of the

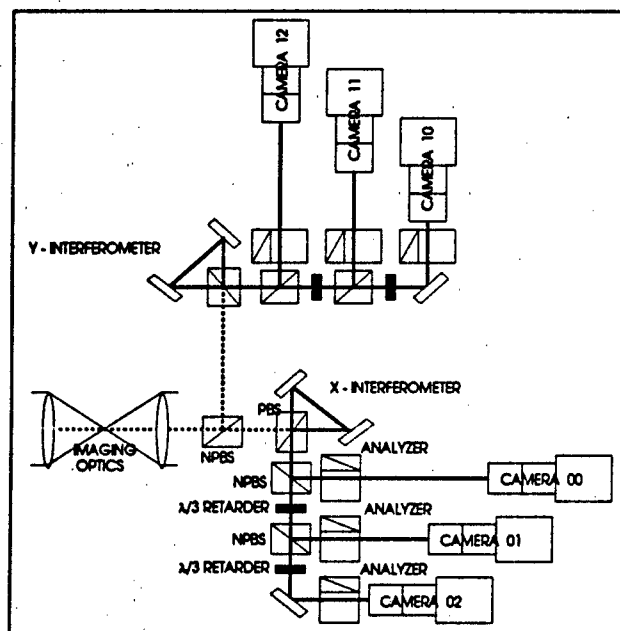


Figure A.4. Shearing Interferometer.

interferometer image the wave of interest onto the six cameras (three in the x -leg and three in the y -leg) and collimate the beam. The first Non-Polarizing Beam Splitter (NPBS) divides the beam into two legs, x and y . The purpose of the two legs is to produce two orthogonal shear directions. The figure shows that the two legs are identical; therefore, only the x -view will be discussed. The main component in each view is the Polarizing Beam Splitter (PBS) and two mirrors arranged in a triangle, forming an equal path interferometer. A shear is produced in one beam relative to the other by rotating the PBS (see Figure A.5). The sheared beam is then separated into three paths, the last two of which have an optical path that is longer by $\frac{\lambda}{3}$ and $\frac{2\lambda}{3}$ with respect to the first path. This optical path difference is introduced with the $\frac{\lambda}{3}$ retarders. The three analyzers then recombine the two polarizations created by the PBS to form an interference pattern at each camera. The interference pattern at each camera will be of the same form as described in Equations A.6 – A.8.

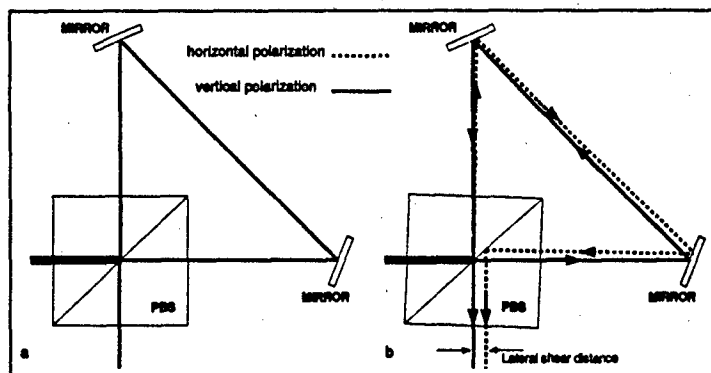


Figure A.5. Method of producing lateral shear. a) No lateral shear produced. b) Lateral shear produced by rotating the PBS.

The images produced by the SI must then be read in by the computer that houses the analysis software routines. Figure A.6 shows the hardware interfaces between the cameras, camera controllers, monitors and the image processing boards. All of the cameras are synchronized to Camera 03. The Androx Boards are used as frame grabbers to acquire the six interference patterns and the PSF and are housed in the Sun-4 computer that serves as the computer interface.

A.4 Alignment and calibration

The initial alignment of the SI is important to proper operation. Each of the six cameras, three for each leg, must image the same wavefront. The six cameras are mounted on three axis micro-positioning stages to enable accurate alignment and focus. The first step in ensuring that the six cameras are imaging the same wavefront is to place a small object, such as a human hair, in one of the object planes of the optical setup. The best location for the hair is at an object point that is located at a mirror. The hair can then be placed at the mirror with the end of the hair touching the mirror. The next step is to adjust the imaging optics and the location of the SI so that the hair is imaged at the cameras and the beam is collimated. This step works best if only one polarization is allowed to pass into the SI, controlled by the half-wave plate prior to the SI. Collimation can be verified by looking at the interference fringes, with both polarizations

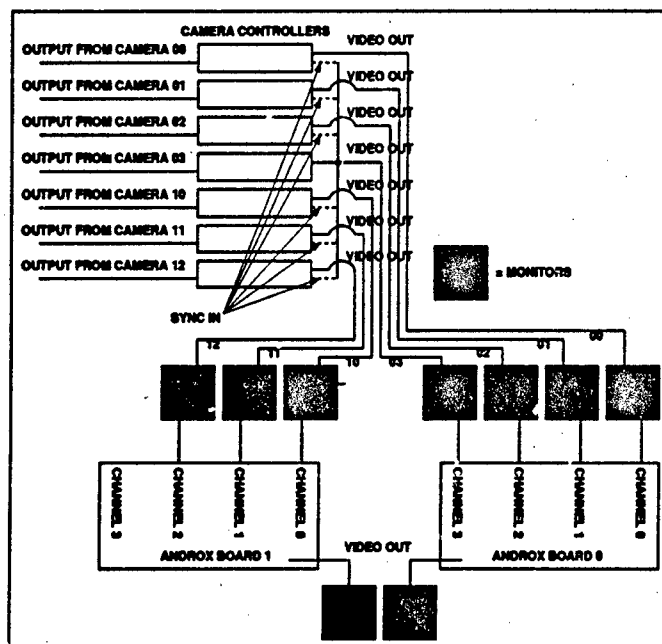


Figure A.6. Schematic of camera interfaces.

allowed to pass into the SI, and adjusting the imaging optics until the fringes disappear. This process is an iterative process and works best if only small adjustments are made each iteration. If all six cameras do not image the hair perfectly, minor adjustments to the quality of focus can be made by adjusting the micro-positioner corresponding to the direction of beam propagation until adequate focus is achieved. Another consideration while adjusting the focus/collimation is keeping the images centered on each of the six cameras.

Once the SI is positioned properly, some calibration of the cameras must be completed. The software that drives the SI and acquires the images to be analyzed aids the user in alignment and calibration of the SI. For a detailed explanation of the procedures to follow, see the corresponding section in Appendix B. This section provides a brief explanation of the types of calibration and alignment that are involved with the SI.

The alignment of the cameras must be calibrated. The three interference patterns for each leg are required to reconstruct the phase map; thus, to ensure accurate results, the interference

patterns must physically overlap. Pixel location 1 of image 01 must be compared to pixel location 1 of image 02 and pixel location 1 of image 03. All six cameras must be aligned with one camera, a reference camera. Camera 00, as shown in Figure A.6, is chosen as the reference camera. Alignment of the cameras is achieved by placing a set of cross-hairs in the pupil plane of the SI and adjusting the location of the camera being aligned, using the micro-positioning stages, until the cross-hairs formed on Camera 00 overlap with the cross-hairs formed on the camera being aligned. The best results are achieved if only one polarization is passed into the SI. This procedure is implemented in the software code that is used with the SI (see Section B.11.1.1).

The magnification of the cameras must also be calibrated. To ensure that all six images are the same size, the magnification of each camera must be identical. This procedure is not written into the code, but could very easily be added. With the circular aperture in the pupil plane, a set of images can be acquired via the software interface. The pixel extent, both in the x - and y -directions, can then be compared for each image. A procedure to implement the comparison of pixel extent can be written in IDL, the code that the current interface is written in. Once the pixel extents have been compared, the magnification can be adjusted by rotating the lenses on the cameras. This is an iterative process that must be repeated until all six images have the same pixel extent. Note that the x - and y -extent of the images is not the same even though the aperture is circular. This is due to the fact that the pixels on the CCD arrays of the cameras are rectangular.

Camera gain must also be calibrated prior to acquiring any data. Because the intensity of each pixel carries the data for the phase map, the camera gains must be adjusted so that they are identical. Before the gain is calibrated the control boxes for each of the cameras (see Figure A.6) must be set with the automatic gain control OFF, and the shutter speed at the fastest setting. The software interface provides for the option of calibrating the gain/offset of the cameras (see Section B.11.3). There are two methods that can be used to calibrate the gain of the cameras; however, only one of the methods calibrates the camera offset as well as the gain. The preferred

method is the one in which the camera gain and offset are calibrated. The calibration is achieved by placing varying magnitudes of neutral density (ND) filters in the optical path and acquiring an image. The software then compares the intensities of the images as a function of the filter density and fits the gain curve to each camera. The values of gain and offset are then saved and can be read in by the software when needed. Note that the gain/offset are adjusted for by the software interface and no physical adjustments need be made to the cameras. This procedure does not need to be completed as often as the alignment or shear/shift calibrations.

The calibration that needs to be completed the most often is the shear/shift calibration. The software interface provides the option for calibrating the shear/shift of the SI by two different methods, as discussed in Section B.11.4. The first method is accomplished by placing a small aperture in the pupil plane of the SI. The software acquires an image for each polarization, centroids the image, and calculates the amount of shear, in pixels, and the amount of shift relative to Camera 00. The shift that is calculated will be zero if the alignment calibration mentioned above is perfect (not likely). This shift is corrected for by the software when the images are analyzed to reconstruct the phase. When using this method, several realizations should be performed prior to and after each data run. The realization should then be averaged and the average values of shear and shift should be used when the images are analyzed. The second method acquires images for each polarization with the circular aperture in the pupil plane. The images are then correlated to calculate the shear and shift. This method takes considerably more computational time but requires less realizations because it is more accurate.

Appendix B. Software Users Manual

The calibration of the SI, data acquisition, and data analysis are all controlled by a user-friendly, menu-driven software interface written in the IDL program language. All of the code is accessible to the user should any alterations to the code be required. This section provides an overview of the operation of the code in some detail so that a new user can operate the SI adequately after reading this appendix. It should be noted that not every nuance of the code will be discussed here because the code itself can be followed by the user with an understanding of IDL. The user is encouraged to have a detailed understanding of the IDL programming language prior to embarking on the operation of the SI. A detailed understanding of the IDL programming language will help immeasurably when trying to understand the operation of the interface code as well as writing any new code that may be required. The description of the code that follows is given with the assumption that the user has a working understanding of the IDL programming language.

The main program and all of the procedures required to run the software interface for the SI are located in the directory */home/shear*, the home directory for user "shear". Thus the user must be logged into the computer as user "shear". The program must be run from within the Sun-View environment. When logged in as user "shear", Sun-View is opened as a default. At the user prompt within a shell-tool window, the code is started by typing *go*, which is an alias for *idl load*. This command starts a batch (*load*) that compiles all of the procedures, sets some parameters for IDL, and runs the main menu program. After all of the procedures are compiled, a small window will appear in the lower right portion of the screen. This is the *idl0* window that has to be opened when using the menu procedures. This window allows the user to switch between the Sun-View environment and IDL environment, determined by the location of the mouse pointer. After some initial programming parameters are set, the main menu for the software interface will appear on the screen. All interfacing to the software code is accomplished within the window from which the

code was started. When the code prompts the user to input a parameter, the input is read from that window. Likewise, any messages from the code are written to the window mentioned.

The main menu contains seven sections:

- **DATA SECTION** - Specifies the data on which operations are performed.
- **REFERENCE SECTION** - Specifies the baseline data used in delta operations.
- **ACQUIRE SECTION** - Used to acquire raw data.
- **ANALYZE SECTION** - Used to analyze raw data.
- **ARCHIVE SECTION** - Used to manage data files.
- **CALIBRATE SECTION** - Used to align and calibrate the SI.
- **DISPLAY SECTION** - Used to display raw and analyzed data.

Each section below is titled by the option in the main program and all subsequent options that fall under that main option are explained within that section. If the selection in the menu activates another menu, the selections from the new menu are described in a different section. The discussion under each section identifies the routines that are activated by selecting that option.

B.1 DATA SECTION

B.1.1 Mode: (current data mode). This line identifies the current data mode. Selecting this option allows the user to change the current data mode, current data group, as well as the current data frame. The data mode is a descriptor for the type of data that is current or the type of data that will be acquired. The data mode also determines which sub-directory the data is or will be stored in on the hard drive. The user can select among three different data modes:

- **real:** Real data includes data that is acquired and will be analyzed as actual experimental data.

- **cal:** Cal data is data that is taken for calibration purposes.
- **test:** Test data is not used but could be implemented to describe data taken to test the system operation, for example.

B.1.2 Group: (current data group). This line identifies the current data group. Selecting this line allows the user to select a data group from the disk as well as the current data frame. The groups on the disk are listed by categories:

- **Data Groups** - Listing all the raw data , by group, currently on the disk.
- **Analysis groups** - Listing raw data, by group, that has previously been analyzed.

Data is stored by group numbers with a letter as the last character of the group name. The letter is a flag that identifies the method of acquisition. A group can contain several frames of raw data. For example, if data group 2025S is acquired, the raw data will be stored in the directory *real/data/2025S/* and the analysis of the raw data for group 2025S will be stored in the directory *real/anal/2025S/*.

B.1.3 Frame: (current data frame). This line identifies the current data frame. Selecting this line allows the user to select a data frame from the current data group. The data frames are separated into three categories.

- **DATA** - Listing of the raw data frames within the current data group.
- **TILT** - Listing of the data frames within the current data group for which the tilt analysis has been conducted previously.
- **PHASE** - Listing of the data frames within the current data group for which the phase analysis has been conducted previously.

The data frames are numbered sequentially, by twos starting with 0, in the order of acquisition. Each data file actually contains two video frames of raw data. For example, if, within the data

group 2025S, there are 4 files (0, 2, 4, and 6) containing the raw data, file 0 will contain frames 0 and 1, 0 corresponding to the even rows of pixels within the image and 1 corresponding to odd rows of pixels within the image. The two images are separated in time by $\frac{1}{60}$ of a second. This interlacing scheme is the method by which the video frames are acquired and the separation of the odd and even frames is accomplished by the software code.

B.1.4 Back: (*current background data*). This line identifies the current background data. Background data are images of light leakage through the shutter of the pockel cell when switched off. These images are subtracted from the data images to remove leakage effects. Note: THIS ONLY NEEDS TO BE DONE IF THE POCKEL CELL IS BEING USED AS A SHUTTER TO INCREASE THE SHUTTER SPEED. Selecting this line activates the background menu, described in Section B.8.

B.2 REFERENCE SECTION

B.2.1 Mode: (*current reference data mode*). This line identifies and selects the current reference data mode, group and frame. This is very similar to the description in Section B.1.1 with the exception that this line selects the reference mode.

B.2.2 Group: (*current reference group*). This line identifies and selects the current reference data group and frame. This is very similar to the description in Section B.1.2 with the exception that this line selects the reference group.

B.2.3 Frame: (*current reference frame*). This line identifies and selects the current reference data frame. This is very similar to the description in Section B.1.3 with the exception that this line selects the reference frame.

B.2.4 Source: (current reference source). This line identifies the source mode for selecting the reference data that is associated with the data that is acquired. Selecting this line enables the user to select from the following reference source modes:

- Data - This mode uses for analysis the reference data that was current when the data was acquired.
- Anal - This mode uses for analysis the reference data that was current when the data was analyzed.
- Current - This mode uses the current reference data for analysis.
- Initial - This mode uses for analysis frame 0 of the current data group.

B.3 ACQUIRE SECTION

B.3.1 Acquire (group to be acquired). This line is used to acquire new data. The number shown indicates the next group to be acquired if a new data group is started. When selected, the user is asked if a new data group is to be started. Depending on the acquisition mode that is selected, other prompts may appear as described in Section B.3.2. After all of the prompts associated with the acquisition mode are given, the hardware is initialized for acquisition and a response window appears. Data is acquired immediately after the clicking on the response box. As mentioned in Sections B.1.1 - B.1.3, data groups and data frames are identified by sequential numbers and the data group numbers are followed by a letter signifying the mode of acquisition.

B.3.2 Mode: (acquisition mode). This line identifies the acquisition mode. Selecting this line allows the user to select from one of the following modes:

- Group - Used to acquire a group of data consisting of 8 frames, 4 pairs of interlaced frames. The first frame of each pair is separated by $\frac{1}{15}$ of a second. Recall that the interlaced frames

are separated by $\frac{1}{60}$ of a second. Group names for data acquired in this manner end with "G."

- Group Pick - Used to acquire a group of data, 4 pairs of interlaced frames, with each pair being acquired after clicking the mouse. Group names for data acquired in this manner end with "P."
- Group Sync - Used to acquire a user defined number of groups separated by a user defined time interval. The actual time interval between subsequent groups depends on how the software is configured to display the acquired data. There is an inherent time delay that the computer uses to write the acquired data to disk and display the acquired frames—if the acquire display mode is set to "Images" (see Section B.3.4). This inherent time delay can be minimized by setting the acquire display mode to "None." The number of groups and time interval are defined after the acquire option is selected. The user is prompted to input both parameters. Group names for data acquired in this manner end with "X."
- Single Pick - Used to acquire single frames with each pair being acquired after clicking the mouse. All frames will be stored in the same data group. Group names end with "S."
- Single Sync - Used to acquire a user specified number of interlaced pairs separated by a user defined time interval. The actual time interval between subsequent frames depends on how the software is configured to display the acquired data. There is an inherent time delay that the computer uses to write the acquired data to disk and display the acquired frames—if the acquire display mode is set to "Images" (see Section B.3.4). This inherent time delay can be minimized by setting the acquire display mode to "None." The number of pairs and the time interval are defined in the same manner as explained for Group Sync. All frames are stored within the same data group and group names also end with "S."

B.3.3 Analyze: (analysis mode). This line identifies the state of the analyze after acquisition. When the mode is set to ON, the raw data will be analyzed immediately after acquisition is

completed. When using either the *Single Sync* or *Group Sync* acquisition mode, the *analysis mode* should be set to OFF.

B.3.4 Display: (acquire display mode). This line identifies what is to be displayed after an acquire is completed. Selecting this line allows the user to choose either "images" or "none." Choosing "images" sets the software to display the raw images associated with the data acquired.

B.4 ANALYZE SECTION

B.4.1 ANALYZE >. Selecting this line activates the analysis menu, described in Section B.9.

B.5 ARCHIVE SECTION

B.5.1 ARCHIVE >. This line activates the archive menu, described in Section B.10. The archive facility produces 8mm tapes containing the raw and analyzed data groups. The tapes are named TAPE_#, where # is a sequential tape number. New data is appended to a list of data, stored in the file tape_buffer, that has not been archived. When this new data is archived, it is appended to the current tape.

B.6 CALIBRATE SECTION

B.6.1 CALIBRATE >. This line is used to activate the calibration menu, described in Section B.11. The calibration menu provides the commands needed for aligning and calibrating the interferometer.

B.7 DISPLAY SECTION

B.7.1 DISPLAY >. This line activates the display menu, described in Section B.12. From the display menu, raw and analyzed data can be displayed on the screen or printed.

B.8 BACKGROUND MENU

B.8.1 Mode: (current background mode). This line identifies and selects the current background data mode, group and frame.

B.8.2 Group: (current background group). This line identifies and selects the current background data group and frame.

B.8.3 Frame: (current background frame). This line identifies and selects the current background data frame.

B.8.4 Source: (current background source). This line identifies the source mode for selecting the background data that is associated with the data that is acquired. Selecting this line enables the user to select from the following background source modes:

- **Data** - This mode uses for analysis the background data that was current when the data was acquired.
- **Current** - This mode uses the current background data for analysis.
- **OFF** - This mode disables the use of background data.

B.8.5 ACQUIRE: (group to be acquired). This line is used to acquire new background data. The shutter should be closed when acquiring background data. When this option is selected, the hardware will be prepared for acquisition and a response window will appear. Data is acquired immediately after clicking on the response box.

B.8.6 Mode: (acquire mode). This line identifies the current background acquire mode. Selecting this line allows the user to select one of the following acquisition modes: Group, Group Pick, Group Sync, Single Pick, and Single Sync. Each acquisition mode is described in Section B.3.2

B.8.7 Save Data Background. Selecting this line associates the current background data to the data that is currently selected.

B.9 ANALYSIS MENU

B.9.1 DATA SECTION. This section allows the user to select the current data mode from the following:

- **Mode:** - Identifies and selects the current data mode, see Section B.1.1.
- **Group:** - Identifies and selects the current data group, see Section B.1.2.
- **Frame:** - Identifies and selects the current data frame, see Section B.1.3.
- **Back:** - Activates the background data menu, see Section B.8.

B.9.2 Analyze. This line initiates analysis of the current data according to the modes and parameters set in this menu.

B.9.3 Mode: (current analysis mode). This line identifies and selects the analysis mode from the following:

- **All** - In this mode, analysis is performed on all data groups currently stored on the hard drive.
- **Group** - In this mode, analysis is performed on all of the frames in the current data group.
- **Single** - In this mode, analysis is performed on the current data frame of the current data group.

B.9.4 UnWrap: (current UnWrap mode). This line identifies and allows the user to change whether or not the raw data is unwrapped into tilt maps in the analysis. The raw data must be present for this operation to function. The mode is either ON or OFF.

B.9.5 Recon: (current Recon mode). This mode determines if the tilt maps are to be reconstructed into a phase map in the analysis. The tilt maps must be present or analyzed for this mode to function. The mode is either ON or OFF.

B.9.6 Repeat: (current Repeat mode). This mode determines whether or not the analysis results are recalculated. When this mode is OFF, the analysis will not recalculate tilt maps or phase maps if the analysis is already present on the disk.

B.9.7 Screen: (current Screen mode). This mode determines if analysis results are displayed to the screen during the analysis. This mode is ON or OFF.

B.9.8 Gain Source (current Gain Source). This line identifies and selects the source of the gain calibration. The source may be one of the following:

- data - This source mode uses the gain calibration which was current when the data was acquired.
- save - This source mode uses the current saved gain calibration.
- call/anal/*.gain - This source mode uses the gain calibration selected from a list of analyzed calibration gains stored on the disk.

B.9.9 Shear Source (current Shear Source). This line identifies and selects the source of the shear calibration. The source may be one of the following:

- data - This source mode uses the shear calibration which was current when the data was acquired.
- save - This source mode uses the current saved shear calibration.
- call/anal/*.shear - This source mode uses the shear calibration selected from a list of analyzed calibration shears stored on the disk.

B.9.10 Shift Source (current Shift Source). This line identifies and selects the source of the shift calibration. The source may be one of the following:

- data - This source mode uses the shift calibration which was current when the data was acquired.
- save - This source mode uses the current saved shift calibration.
- call/anal/*.shift - This source mode uses the shift calibration selected from a list of analyzed calibration shifts stored on the disk.

B.10 ARCHIVE MENU

B.10.1 Load Tape: (current tape). This line identifies the last loaded tape. Selecting this line allows for selecting and loading a tape from the tapes available. This option is not necessary since tape loading is performed within other options.

B.10.2 View Tape: (current tape). This line allows the user to view the contents of archive tapes. The actual tapes do not need to be loaded into the tape drive for this command to operate. A list of the data groups stored on each archive tape are stored in a file under the archive directory. The file name is the same as the name of the tape.

B.10.3 Save Data. This routine is used to save to the current tape all data groups that have not yet been archived. The routine gives instruction for inserting the proper tape. Depending on the amount of data to be archived and the amount of data already on the tape, this could be a long process. Data will be stored to the last created tape.

B.10.4 Restore Data. This routine is used to restore archived data back to disk. The first step is to select which tape to restore data from (the View Tape command is useful in quickly locating the data). Instructions for loading the selected tape are then given. Once the selected tape

is loaded, a list of available groups is displayed. The user must then select the desired data group to be restored. After the selected group is restored to disk, the list of groups is again displayed so that other selections may be made. This process repeats until the user selects the QUIT option from the list of groups.

B.10.5 Delete Disk. This routine safely deletes the data from the hard drive. The routine will function only if all data has been archived with the Save Data command. The routine will give a list of data currently on the hard drive. The user may then select the group to be deleted. The data groups are categorized into sections for ease in locating the desired group. Each section is headed by an "ALL" option that deletes all of the data groups within that section. Note that the calibration section deletes only the raw calibration data; the analyzed calibration results are used in the data analysis and are not deleted.

B.10.6 Create Tape. This routine creates a new archive tape for data backups. Each tape is identified by a file written to the beginning of each tape, tape_id, that holds the tape name and date created. This file is read each time a tape is inserted to ensure that the proper tape is loaded.

B.11 CALIBRATION MENU

B.11.1 ALIGNMENT SECTION.

B.11.1.1 Align: (xx). This routine allows for physically aligning the cameras to the reference camera, Camera 00. The xx is a two digit number identifying the camera for alignment. The first digit is the Androx board number and the second digit is the Androx channel number, see Figure A.6. The routine gives a visual display on the Androx output monitors that aids in the alignment of the cameras. A cross-hair mask must be placed in the pupil plane of the SI. The camera to be aligned is then selected. The display flashes the cross-hair image from Camera 00 superimposed on the cross-hair pattern of the camera being aligned. Adjustments

are then made using the two micro-positioners corresponding to the directions transverse to the propagation direction of the beam until the images overlap.

B.11.2 DATA SECTION.

B.11.2.1 Mode: (current data mode). This line identifies and selects the current data mode, data group and data frame, see Section B.1.1.

B.11.2.2 Group: (current data group). This line identifies and selects the current data group and data frame, see Section B.1.2.

B.11.2.3 Frame: (current data frame). This line identifies and selects the current data frame, see Section B.1.3.

B.11.2.4 Back: (current background data). This line activates the background menu, see Section B.8.

B.11.3 CAMERA GAIN SECTION.

B.11.3.1 Acquire & Analyze Focus. This routine acquires and analyzes images for calibration of the gain as described below. The raw images are stored in the *cal/data/* sub-directory, and the data group names end with the identifier "F". This method of calibrating the camera gain is quick and crude and does not measure the camera offset.

B.11.3.2 Acquire Focus. This routine is used to acquire calibration images with a large amount of focus in the beam. The idea is to have several fringes across the images and therefore have areas of peak intensities on each camera.

B.11.3.3 Analyze Focus. The focus images are read and analyzed with this routine. The peak intensity for each camera is found and the gains which would make all of the cameras have the same peak intensity are calculated.

B.11.3.4 Read Focus Analysis. This routine displays the analyzed focus results.

B.11.3.5 Acquire & Analyze Gain/Offset. This routine acquires and analyzes the images for calibration of the gain and offset as described below. The raw images are stored in the *cal/data/* sub-directory, and the data group names end with the identifier "A". This method calculates the gain and offset adjustments for the cameras based on the measured linear relationship between beam intensity and image intensity. This method is preferred over the focus method.

B.11.3.6 Acquire Gain/Offset. This routine is used to acquire a set of images with various exposure levels. The data should be acquired with only one polarization present and therefore no interference effects. The routine repeatedly asks for exposure level and then acquire new data for that level. The exposure level is varied on a linear scale by adjusting the shutter speed or with ND filters.

B.11.3.7 Analyze Gain/Offset. This routine performs a linear regression of camera intensity as a function of exposure level for each camera. The mean intensity for a central area of each image is used for camera intensity. Then necessary gains and offsets which would make all cameras have the same linear relationship between exposure level and camera intensity are calculated.

B.11.3.8 Read Gain/Offset Analysis. This routine reads and displays the analyzed Gain/Offset results.

B.11.3.9 Save Gain/Offset. This routine saves the specified calibration data as the current instrument Gain/Offset calibration. When new data is acquired, this current calibration is stored along with the data.

B.11.4 SHEAR MEASUREMENT SECTION.

B.11.4.1 Acquire & Analyze Spot. This routine acquires and analyzes the images for calibrating the instrument shear, as described below. The raw images are stored in the *cal/data/* sub-directory, and the data group names end with the identifier "C". This method measures the shear by centroiding the image formed by a pinhole placed in the pupil plane of the SI. Data is acquired for both polarizations and the centroid of the spots gives the relative translations between images. The difference in the centroid locations of the two polarizations is a measure of the shear.

B.11.4.2 Acquire Spot. This routine prompts the user for setting and then acquiring data for horizontal and then vertical polarization. A pin hole mask should be placed at the pupil plane of the SI and not moved during data acquisition.

B.11.4.3 Acquire Multi Spots. This routine allows the user to acquire a user defined number of spots for calibration of the instrument shear and shift.

B.11.4.4 Analyze Spot. This routine calculates the centroids of the spot images and then takes their differences to produce the measured shear and the camera translation corrections relative to Camera 00.

B.11.4.5 Read Spot Analysis. This routine reads and displays the analyzed spot results.

B.11.4.6 Acquire & Analyze Correlation. This routine acquires and analyzes the images for calibrating the instrument shear, as described below. The raw images are stored in

the */cal/data/* sub-directory, and the data group names end with the identifier "B". This method measures the shear by correlating images of the full aperture. Data is acquired for both polarizations and the correlation between the images gives the relative translations between images. The correlation between the two polarizations is a measure of the shear. This method requires longer computation times, but is more accurate than the centroid spot routine described above.

B.11.4.7 Acquire Correlation. This routine prompts the user for setting and then acquiring data for horizontal and the vertical polarization.

B.11.4.8 Analyze Correlation. This routine correlates the images and uses the resulting lags to produce the measured shear and the camera translation corrections.

B.11.4.9 Read Correlation Analysis. This routine reads and displays the analyzed correlation results.

B.11.4.10 Save Shear & Shift. This routine saves the specified calibration data as the current instrument Shear & Shift calibration. When new data are acquired, this current calibration is stored along with the data.

B.12 DISPLAY MENU

B.12.1 DATA SECTION.

B.12.1.1 Mode: (current data mode). This line allows the user to select the current data mode, group, and frame, see Section B.1.1.

B.12.1.2 Group: (current data group). This line allows the user to select the current data group, and frame, see Section B.1.2.

B.12.1.3 Frame: (current data frame). This line allows the user to select the current data frame, see Section B.1.3.

B.12.1.4 Back: (current background data). This line activates the background data menu, see Section B.8.

B.12.2 REFERENCE SECTION.

B.12.2.1 Mode: (current reference mode). This line allows the user to select the current reference mode, group, and frame, see Section B.2.1.

B.12.2.2 Group: (current reference group). This line allows the user to select the current reference group, and frame, see Section B.2.2.

B.12.2.3 Frame: (current reference frame). This line allows the user to select the current reference frame, see Section B.2.3.

B.12.2.4 Source: (current reference source mode). This line allows the user to select the current reference source mode, see Section B.2.4.

B.12.3 SINGLE SECTION. This section is used to display the analyzed results of the current data frame.

B.12.3.1 SLOPES. Selecting this option displays surface plots of the *X* and *Y* tilt maps.

B.12.3.2 X SLOPE. Selecting this option displays a surface plot of the *X* tilt map.

B.12.3.3 Y SLOPE. Selecting this option displays a surface plot of the *Y* tilt map.

B.12.3.4 PHASE. Selecting this option displays a surface plot of the phase map and displays the reconstructed interferograms on the Androx monitors.

B.12.3.5 INTERFEROGRAM. Selecting this option displays the reconstructed interferograms on the screen and on the Androx monitors.

B.12.4 SINGLE DELTA SECTION. This section is used to display the difference between the analyzed results of the current data frame and the current reference frame.

B.12.4.1 SLOPES. Selecting this option displays surface plots of the ΔX and ΔY tilt maps.

B.12.4.2 X SLOPE. Selecting this option displays a surface plot of the ΔX tilt map.

B.12.4.3 Y SLOPE. Selecting this option displays a surface plot of the ΔY tilt map.

B.12.4.4 PHASE. Selecting this option displays a surface plot of the delta-phase map and displays the reconstructed interferograms on the Androx monitors.

B.12.4.5 INTERFEROGRAM. Selecting this option displays the reconstructed interferograms on the screen and on the Androx monitors.

B.12.5 GROUP SECTION. This section is used to scan through the analyzed results of the current data group. Note: there are some software bugs with this option.

B.12.5.1 X SLOPE. Selecting this option displays surface plots of the ΔX tilt maps.

B.12.5.2 Y SLOPE. Selecting this option displays surface plots of the ΔY tilt maps.

B.12.5.3 PHASE. Selecting this option displays surface plots of the delta-phase maps and displays the reconstructed interferograms on the Androx monitors.

B.12.5.4 INTERFEROGRAM. Selecting this option displays the reconstructed interferograms on the screen and on the Androx monitors.

B.12.6 GROUP DELTA SECTION. This section is used to display the difference between the analyzed results of the current data group and the current reference frame.

B.12.6.1 X SLOPE. Selecting this option displays surface plots of the ΔX tilt maps.

B.12.6.2 Y SLOPE. Selecting this option displays surface plots of the ΔY tilt maps.

B.12.6.3 PHASE. Selecting this option displays surface plots of the delta-phase maps and displays the reconstructed interferograms on the Androx monitors.

B.12.6.4 INTERFEROGRAM. Selecting this option displays the reconstructed interferograms on the screen and on the Androx monitors.

B.12.7 IMAGES SECTION. This section is used to display the raw images of the current data.

B.12.7.1 SINGLE. Selecting this line displays the raw images of the current data frame on the Androx monitors and the gain/offset adjusted images on the screen.

B.12.7.2 GROUP. Selecting this line scans through the raw images of the current data group and displays them on the Androx monitors.

B.12.7.3 PSF. Selecting this line displays, to the screen, the PSF image and a surface plot of the PSF intensity of the current data frame.

B.12.7.4 PSF GROUP. Selecting this line scans through the PSF images of the current data group and displays them on the Androx monitors. The centroid coordinates of the PSF are displayed to the screen.

B.12.8 OTHER SECTION. This section is used to set modes and parameters for the display menu.

B.12.8.1 SCREEN. This line identifies and allows the user to select the display screen mode from the following:

- **ON** - In this mode, graphics output is displayed to the screen.
- **ASK** - In this mode, the user is asked if the graphics output should be displayed to the screen.
- **OFF** - In this mode, graphics output is not displayed to the screen. Note: these options only effect the graphics outputs. All non-graphics output, text instructions, and inputs are always displayed to the window from which the software was started.

B.12.8.2 PRINTER. This line identifies and allows the user to select the display print mode from the following:

- **ON** - In this mode, graphics output is written to a postscript file and sent to the laser printer.
- **ASK** - In this mode, the user is asked if the graphics output should be written to a postscript file and sent to the laser printer.
- **OFF** - In this mode, graphics output is not written to a postscript file or printed.

B.12.8.3 X SECTION. This line identifies and allows the user to select the display cross section mode from the following:

- **ON** - In this mode, cross sections of the surface plots are displayed.

- **ASK** - In this mode, the user is asked if cross sections of the surface plots should be displayed.
- **OFF** - In this mode, cross sections of the surface plots are not displayed.

B.12.8.4 SET UP >. Selecting this line activates the Set Up menu for display parameters as described in Section B.13.

B.13 SET UP MENU

B.13.1 REMOVE CURVE FROM PHASE . This section allows the user to determine which aberrations are to be removed from the phase maps prior to display. The piston, tilt, focus and astigmatism of all phase and tilt maps are calculated and their values are listed on the surface plot of the phase. An "R" following the value of an aberration listed on the surface plot indicates that the aberrations have been mathematically subtracted from the surface plot. The menu lists the four aberrations mentioned. Selecting one of the aberrations listed toggles the value following the aberration between a "1" and a "0". The "1" indicates that the aberration will be removed while the "0" indicates that the aberration will not be removed.

B.13.2 REMOVE CURVE FROM SLOPES . This section allows the user to determine which aberrations will be mathematically subtracted from the tilt maps prior to display.

B.13.3 SHOW BORDER ON MAPS . This section allows the user to determine how the borders of the surface plots will be displayed. A "1" indicates that the border area is fit to the curve while a "0" indicates that the border will be set to the minimum value of the data being displayed. The plot border can be selected for both the phase maps and the tilt maps.

B.13.4 ADD TILT TO INTERFEROGRAMS . After the phase maps are calculated and displayed, two computer generated interferograms are displayed on the Androx monitors. Each interferogram is generated by "interfering" the calculated wavefront with a plane wave having

some amount of tilt. This section allows the user to input the amount of tilt - in waves - present in the reference wavefront.

B.13.5 1: X-Tilt. Identifies and sets the amount of tilt, in waves, applied to the reference plane wave in the *X* direction for the first interferogram.

B.13.6 1: Y-Tilt. Identifies and sets the amount of tilt, in waves, applied to the reference plane wave in the *Y* direction for the first interferogram.

B.13.7 2: X-Tilt. Identifies and sets the amount of tilt, in waves, applied to the reference plane wave in the *X* direction for the second interferogram.

B.13.8 2: Y-Tilt. Identifies and sets the amount of tilt, in waves, applied to the reference plane wave in the *Y* direction for the second interferogram.

B.14 EXAMPLE

This section outlines the procedures to calibrate the SI and acquire a set of experimental data. This section should serve as an example only. Several of the parameter settings discussed can be changed to the desired settings determined by the specific requirements of the experiment being conducted. All menu choices are indicated by boldface type.

B.14.1 Calibration. The camera gain and offset should be calibrated prior to starting a new experiment. For this procedure, the circular aperture should be placed in the pupil plane. This calibration procedure does not need to be conducted again for the duration of the experiment. The procedure is started by selecting the **CALIBRATION** option from the **MAIN MENU**. This selection activates another menu, the **CALIBRATION MENU**. Within this menu, select the **Acquire and Analyze Gain/Offset** option. The software then prompts the user to set a single polarization. The next step is to input the exposure level. The exposure level is determined by the

ND filter placed in the beam. Start with the lowest amount of filtering that does not completely saturate the cameras, input the exposure and click the mouse to acquire the images. Increase the filtering by a small amount and repeat the procedure. Continue this procedure approximately 10 to 15 times to ensure adequate sampling. After the last image has been acquired, select the quit option. The code then analyzes the images to calculate the gain and offset and sends the user back to the CALIBRATION MENU. From this menu, select the **Save Gain/Offset** option which saves the current gain/offset calibration to the disk.

The next calibration to be performed is the alignment. For this procedure the cross-hair mask should be placed in the pupil plane. From the CALIBRATION MENU, select the **Align 01** option. The Androx monitors then flash the cross-hair pattern from Camera 00 superimposed on the cross-hair pattern from Camera 01. Adjust the micro-positioners until the images overlap. The cross-hair pattern is actually several pinholes arranged in a + pattern. When the images overlap, the pinholes will be dark in the center. Once the images are aligned as desired, select the **continue** option from the prompt window. The user is then be sent to the CALIBRATION MENU. Repeat this procedure for Cameras 02, 10, 11, and 12.

Next, the shear and shift must be calibrated. Recall that there are two methods by which this can be accomplished. The first method is the spot centroid method. For this procedure the pinhole mask should be placed in the pupil plane. From the CALIBRATION MENU select the **Acquire and Analyze Spot** option. The software then prompts the user to set the horizontal polarization. This is accomplished by rotating the half-wave plate to the required position. After setting the polarization, click the mouse on the prompt window. The image for the horizontal polarization is then be acquired. The user is then be prompted to set the vertical polarization. After the polarization is set, click the mouse on the prompt window to acquire the image for the vertical polarization. The software then determines a centroid for each of the images and computes the shear and shift. Repeat this procedure about six times so that the results can be averaged. The

user is then sent back to the CALIBRATION MENU. Do not save the shear and shift calculations until after the results have been averaged. If the user decides to use the correlation method instead of the spot centroid method, the full aperture should be placed in the pupil plane. From the CALIBRATION MENU select the option **Acquire and Analyze Correlation**. The remainder of the procedure is identical to the centroid spot method. After the images are acquired, the software performs the correlations to determine the shear and shift. Because this method is more accurate, not as many realizations need to be acquired for averaging. Calibration of the shear and shift should be performed for each new data group being acquired. The shear and shift should also be calculated prior to and after acquisition of a data group and the results averaged.

B.14.2 Acquisition. After the pre-acquisition calibrations have been performed, a reference data group must be acquired. For this procedure, place the full aperture in the pupil plane and the set half-wave plate to pass both polarizations. The reference data is used to subtract the effects due to the experimental setup without any turbulence introduced. From the MAIN MENU under the ACQUIRE SECTION examine the line **Mode: acquisition mode**. The *acquisition mode* should be set at "Single Sync." If it is not, select that line to change the *acquisition mode* to read "Single Sync." The line **Analyze: analysis mode** should read OFF so that the analysis is not performed immediately after acquisition. The line **Display: acquire display mode** can be set to either ON or OFF. Also at the MAIN MENU, under the DATA section, the line **Mode: current data mode** should read "real" and the line **Back: current background data** should read OFF or not list a current background data group. Next, select the **Acquire** option from the MAIN MENU. The software then asks if a new group is to be started, click on the yes option. The next window displays the settings for the Single Sync acquisition mode. The number of interlaced frames should be about 8; this tells the software to acquire 8 pairs of images. This parameter can be changed by selecting the line and inputting the desired number at the window from which the program was initially started. The time interval can be changed in the same manner and, for this example,

should read 0 sec. The software then prompts the user with a continue window; this gives the user a last chance to make sure everything on the optics bench is set correctly. Be sure that the half-wave plate prior to the SI is set to pass both polarizations. If everything is set properly, select **CONTINUE**. The software then acquires the specified number of frame pairs. This data is analyzed after the experimental images are acquired.

After the reference data is acquired, the experimental data can be acquired. The steps to follow are identical to those followed for the reference data. The number of interlaced frames to be acquired should be set to 120, and the time interval should read 17 seconds. The software code then acquires the 120 frame pairs separated by about 30 seconds; the code has an inherent 13 second delay in this mode.

After the reference data and experimental data are acquired, more shear/shift calibrations should be performed. If using the spot centroid method, acquire and analyze the spot centroid about 4 more times. Next the shear/shift calibrations must be averaged. There is no current option for this from the main menu, so the user must exit the main program. Control is sent back to the *idl* prompt in the initial startup window. All procedures that were initially compiled are stored in memory. The user must then edit the *read_all_cal* procedure in the *calib.pro* file. This procedure must be edited to reflect the calibration group results that are to be averaged together as well as the filename to which the averaged results are to be written. After the file has been edited and saved, it must be recompiled. At the *idl* prompt, type *.run calib*. The procedures contained in the file *calib.pro* are recompiled. After the procedures are recompiled, call the procedure *read_all_cal* by typing the procedure name. The procedure is activated and the calibrations results defined in the procedure are averaged. These averaged results must then be made the current shear/shift results used for analyzing the acquired data. From the *idl* prompt, the MAIN MENU can be entered by typing *.go*. Enter the CALIBRATION MENU and set the Gain Source to "save", the Shear Source to the file that the averaged results were saved to plus the extension "shear", and the Shift

Source to the file that the averaged shift results were saved to plus the "shift" extension. Note that the extensions for the averaged results are written automatically.

B.14.3 Analysis. Now the data needs to be analyzed. From the MAIN MENU select the **ANALYZE >** option. This will activate the ANALYSIS MENU. The line *Mode: current analysis mode* should read "ALL" so that all of the data is analyzed. The lines **UnWrap**, **Recon**, and **Repeat** should read ON, ON, and OFF respectively. The **Gain Source**, **Shear Source**, and **Shear Source** should read as described above. With everything set as described, select the **Analyze** option to initiate the analysis.

When the analysis is complete, the experimental data must have the reference data subtracted. From the MAIN MENU, verify that the current reference mode and group are set to the reference data that was acquired. The reference frame should be set to *group*, the average of all the frames in that group. The line *Source: current reference source* should read *current*. From the DISPLAY MENU under the GROUP DELTA section, select the **Phase** option to calculate and display the delta phase maps. The display options for the screen and the printer need to be set to the desired settings prior to initiating this step. The delta data are be stored in a group name reflecting the two groups that were subtracted.

Appendix C. Turbulence Chamber Design Drawings

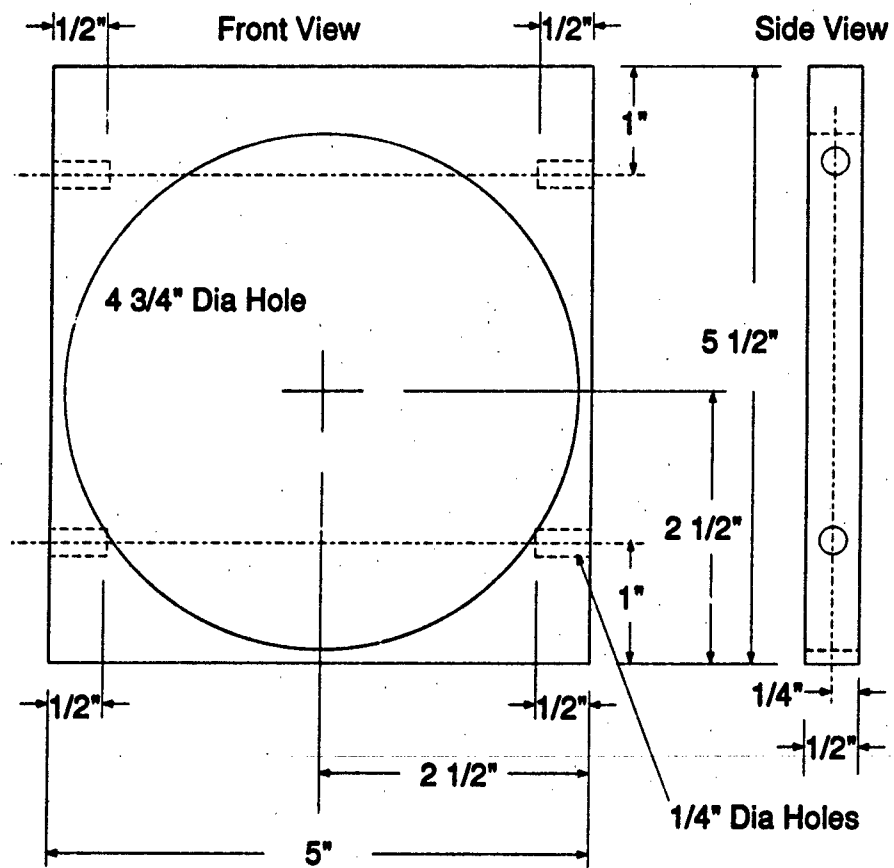
This appendix gives the detailed engineering drawings of the turbulence chamber used in this experiment. This turbulence chamber was designed by Thomas Baudendistel and built by the fabrication shop at the Air Force Institute of Technology (AFIT).

Turbulence Chamber Part List for two Chambers

Part Letter	Description	Number Required
A	Fan Mount (1/2" Plywood)	4
B	Top and Bottom (1/2" Plywood)	4
C	End Cover (1/2" Plywood)	2
D	Heater Element Mount (1/16" sheet metal)	2
E	Filter Guides (1/16" sheet metal)	8
F	Front Support (1/2" wood dowel)	2
G	Side Covers (1/2" Plywood)	4
---	1/4"dia x 1" Wood Dowel Pins	48
Notes:	Attach Parts A-F with glue and/or wood screws. Part G is attached to Chamber with wood dowel pins for removability. Chambers should also be able to connect together in series instead of side covers. Therefore, wood dowel pins should not be glued in place.	

Table C.1.

Part A



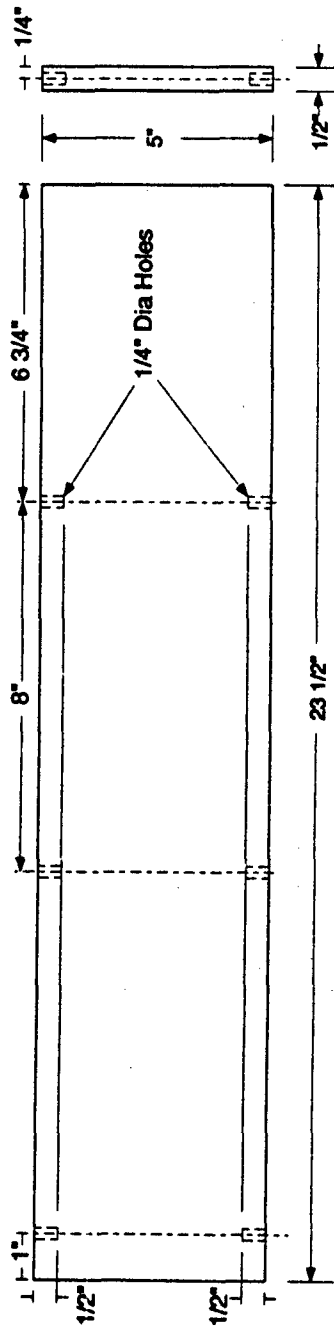
All Material - 1/2" Plywood Both sides finished
2 Required

Figure C.1.

Part B

Front View

Side View

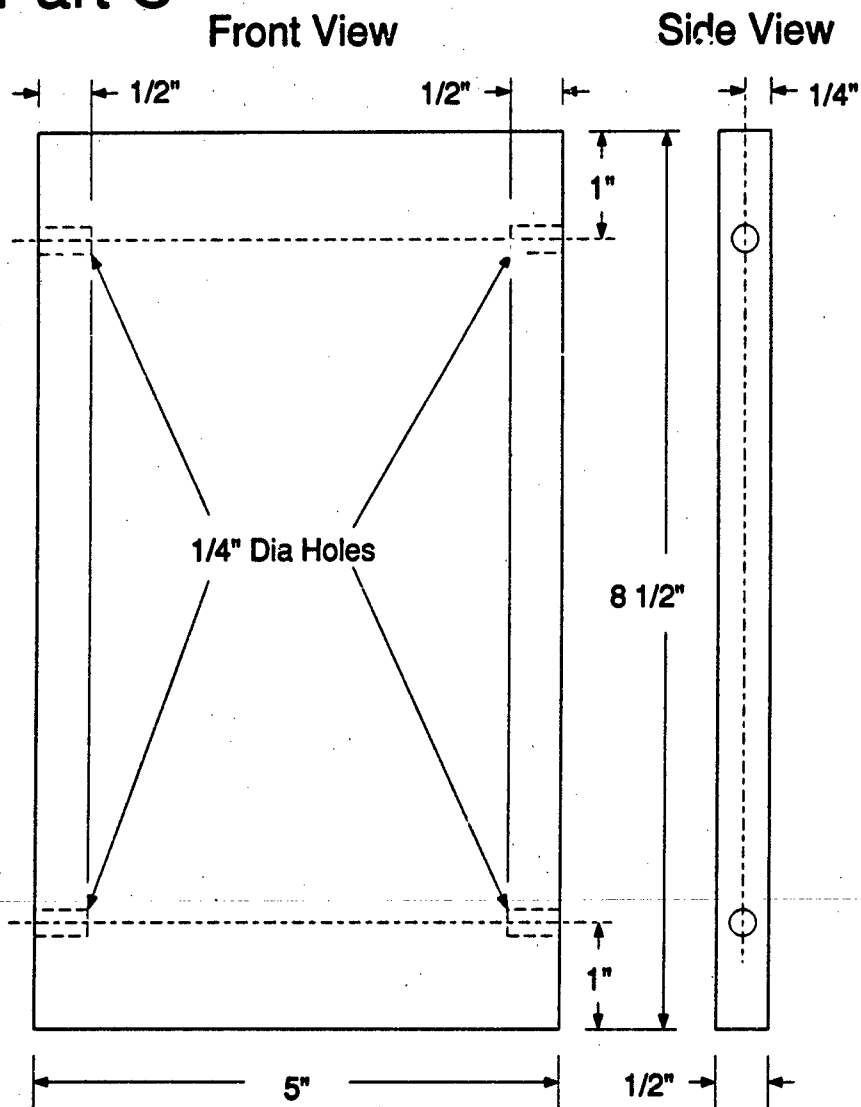


All Material - 1/2" Plywood Both sides finished

1 Required

Figure C.2.

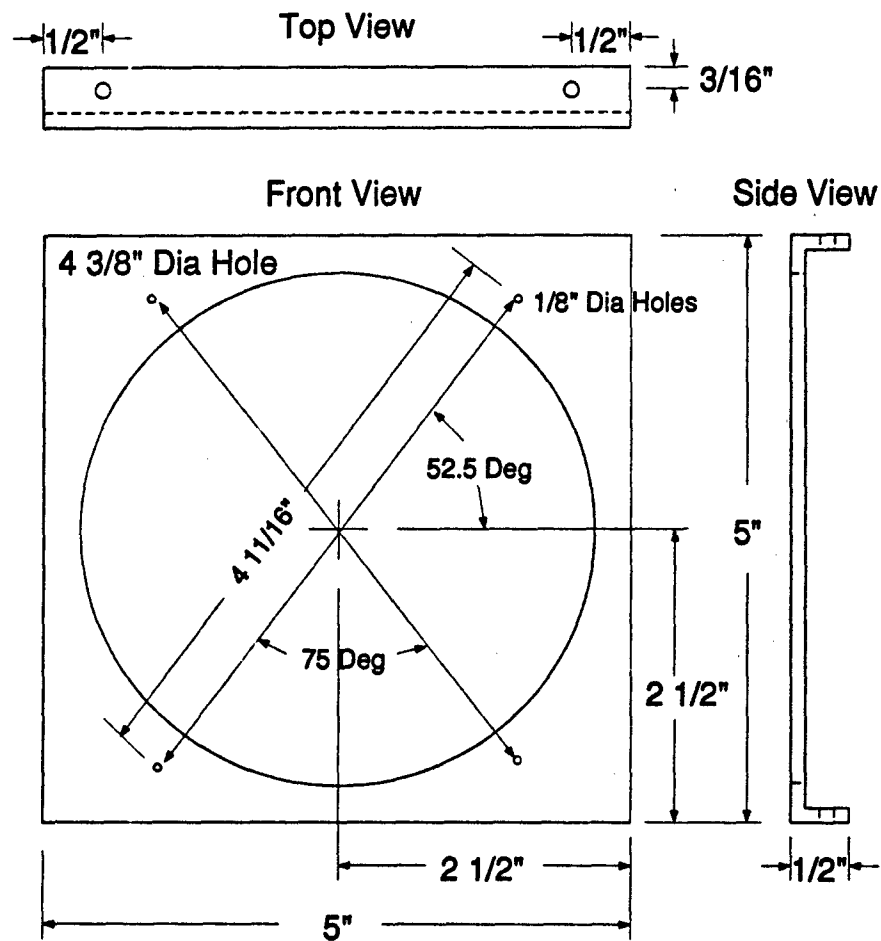
Part C



All Material - 1/2" Plywood Both sides finished
1 Required

Figure C.3.

Part D



All Material - $\frac{1}{16}"$ Thick Sheet Metal
1 Required

Figure C.4.

Part E

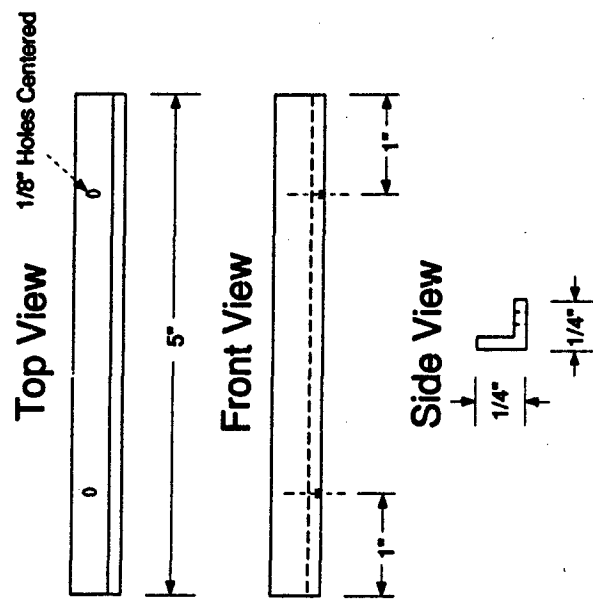
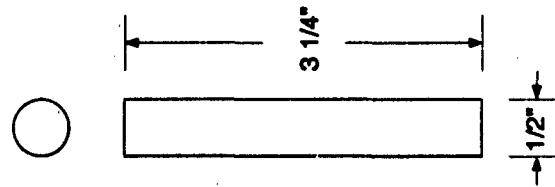


Figure C.5.

Part F



All Material - 1/16" Steel Angle
4 Required

All Material - 1/2" Wood Dowel
1 Required

Part G

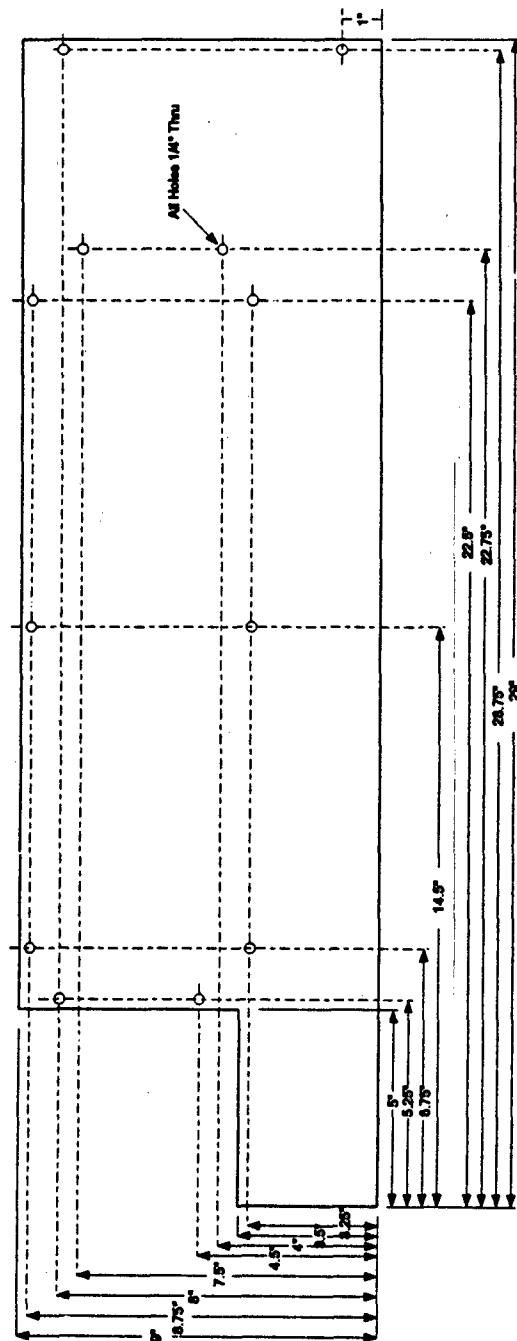


Figure C.6.

All Material - 1/8" Plexiglass

4 Required

Turbulence Chamber Front View

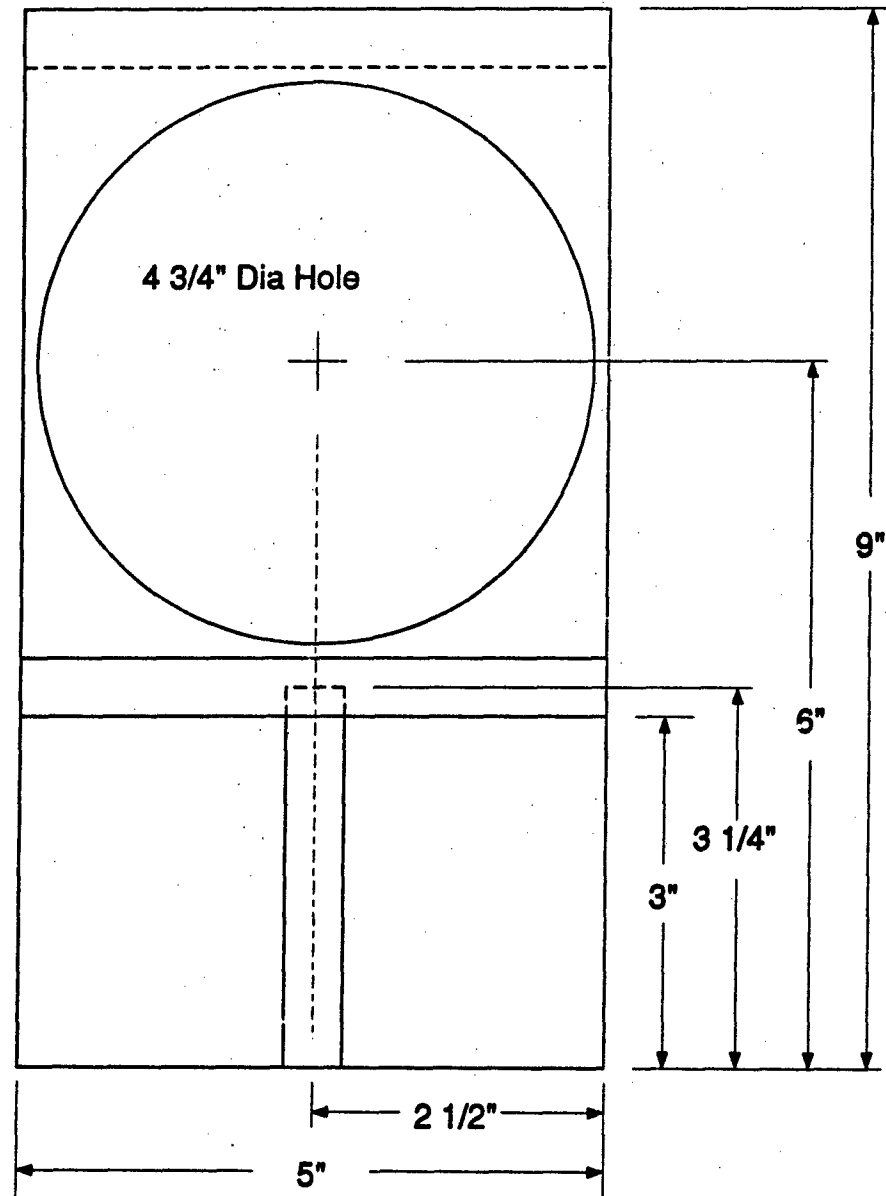


Figure C.7.

Turbulence Chamber Side View

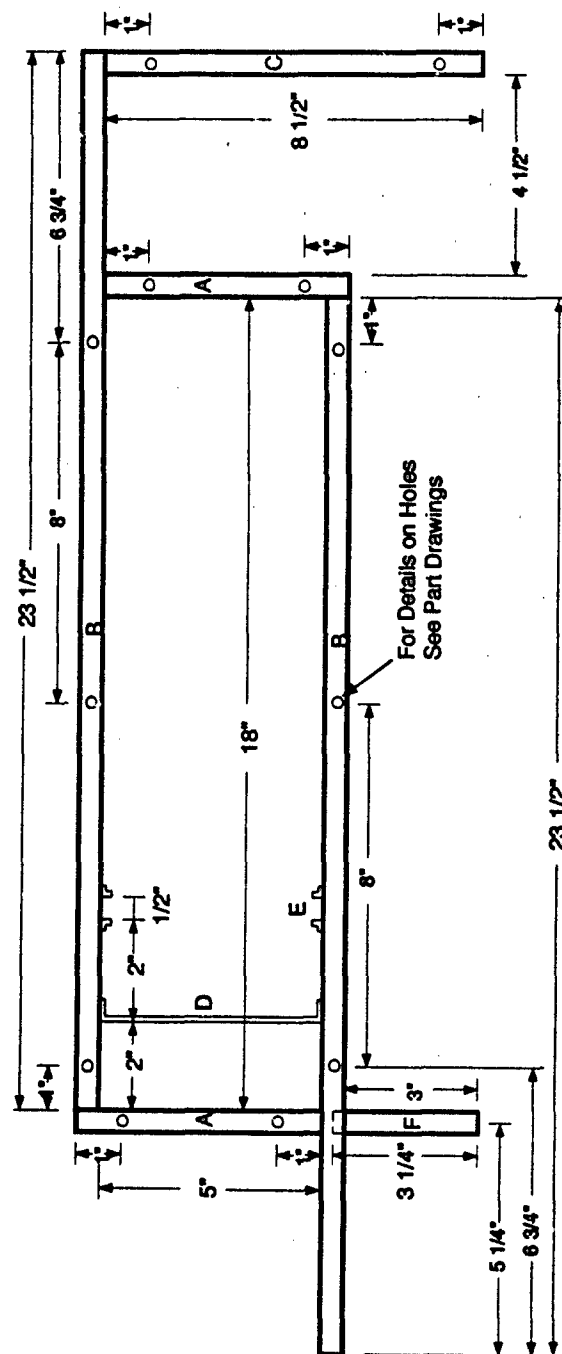


Figure C.8.

All Wood 1/2" Plywood - Both Sides Finished
Not Shown - Part G - Plexiglass Covers (Both Sides)

Appendix D. Additional Phase Structure Function Plots

This appendix includes the remainder of the phase structure function plots that are not included in the main results section. All of the data presented in this appendix is used to determine the characteristics of the turbulence generated.

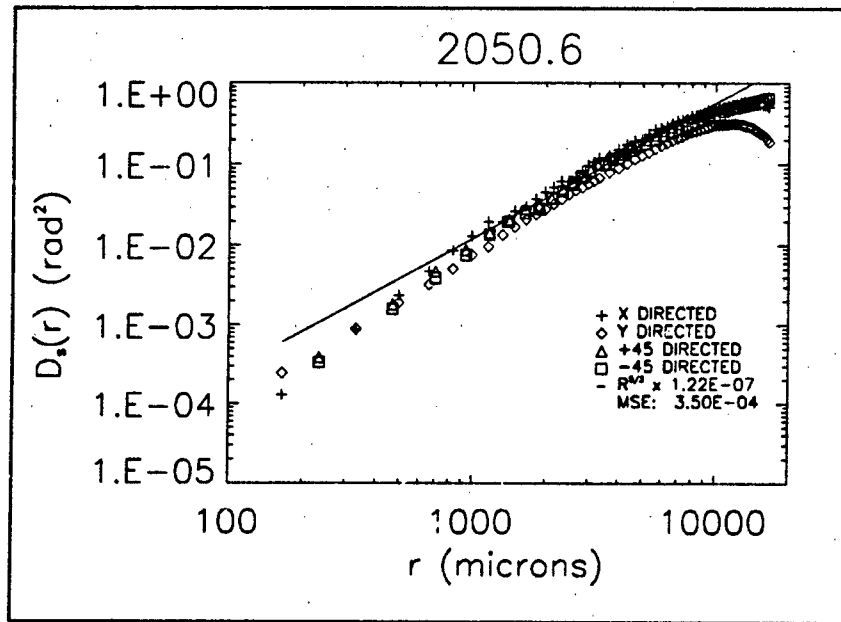


Figure D.1. $\hat{D}_s(r)$ for 2050, location 6. The fan voltage is 20 volts; the element voltage is 50 volts; there is no screen in the chamber; the average temperature is 35° C.

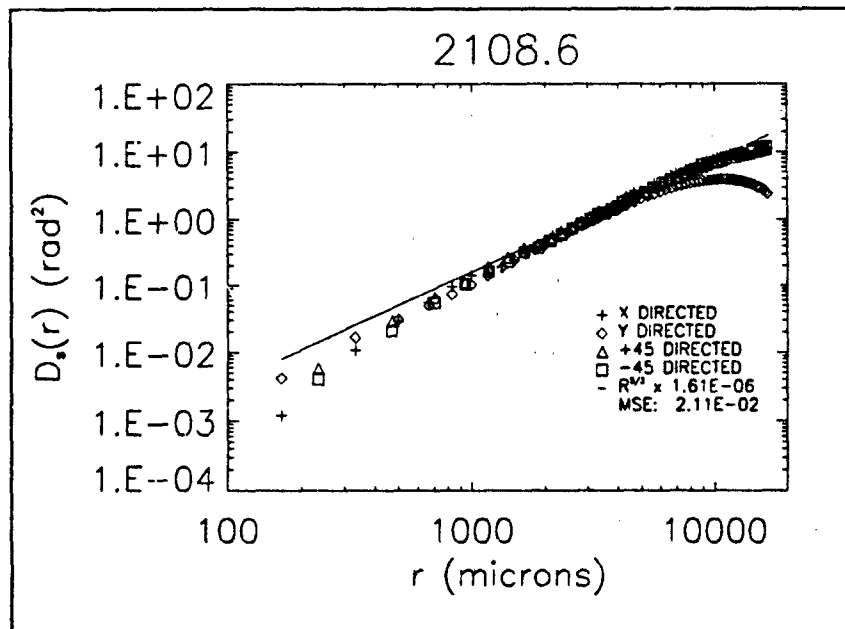


Figure D.2. $\hat{D}_s(r)$ for 2108, location 6. The fan voltage is 20 volts; the element voltage is 80 volts; there is no screen in the chamber; the average temperature is 73° C.

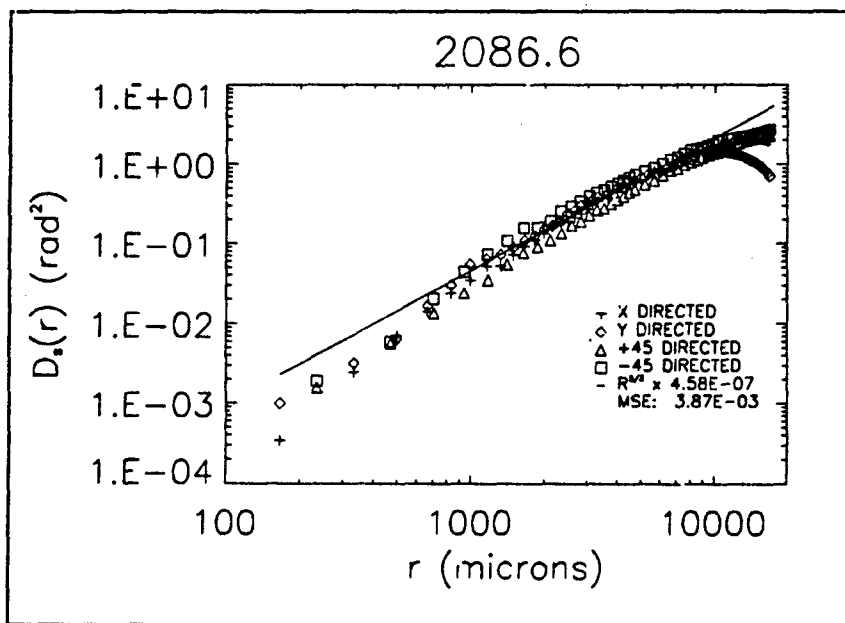


Figure D.3. $\hat{D}_s(r)$ for 2086, location 6. The fan voltage is 20 volts; the element voltage is 35 volts; there is one screen in the chamber; the average temperature is 32° C.

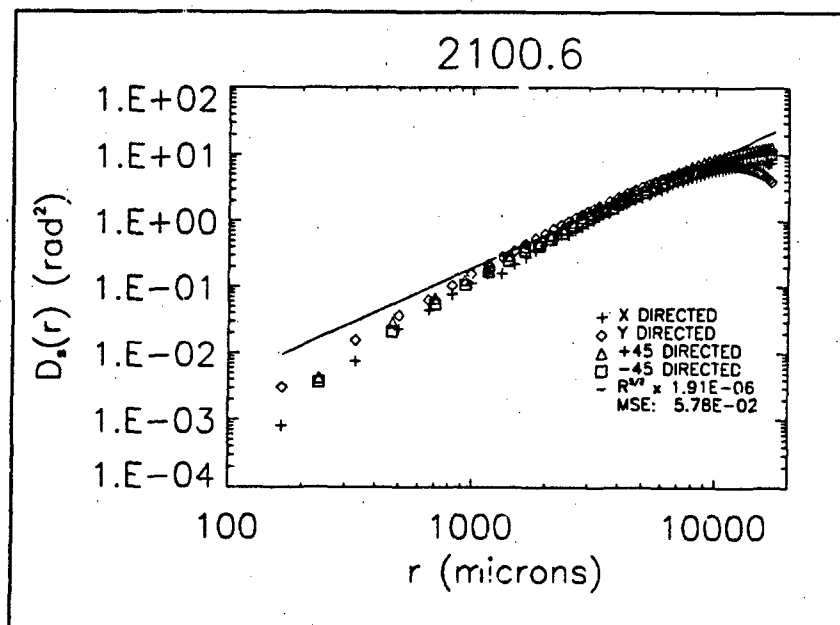


Figure D.4. $\hat{D}_s(r)$ for 2100, location 6. The fan voltage is 20 volts; the element voltage is 65 volts; there is one screen in the chamber; the average temperature is 60° C.

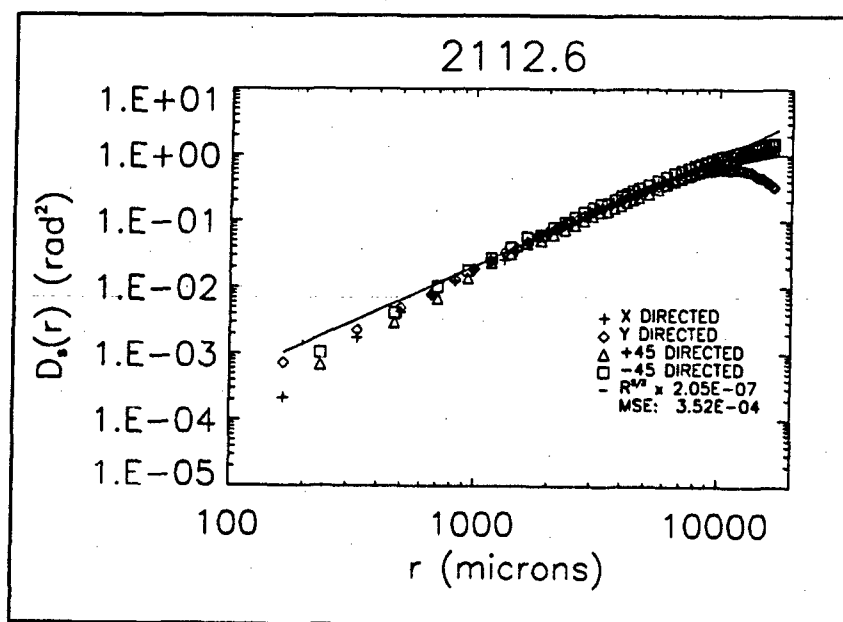


Figure D.5. $\hat{D}_s(r)$ for 2112, location 6. The fan voltage is 35 volts; the element voltage is 50 volts; there is no screen in the chamber; the average temperature is 35° C.

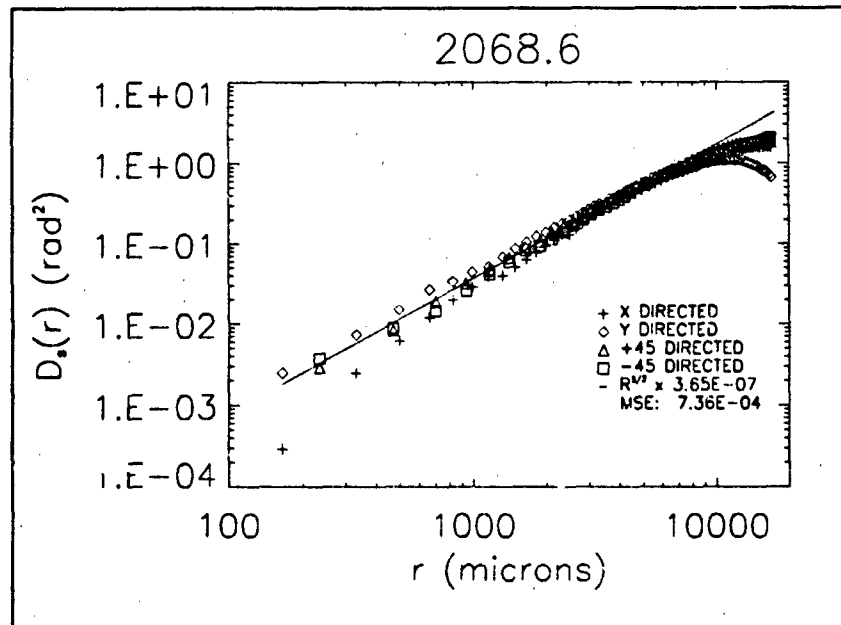


Figure D.6. $\hat{D}_s(r)$ for 2068, location 6. The fan voltage is 35 volts; the element voltage is 65 volts; there is no screen in the chamber; the average temperature is 44° C.

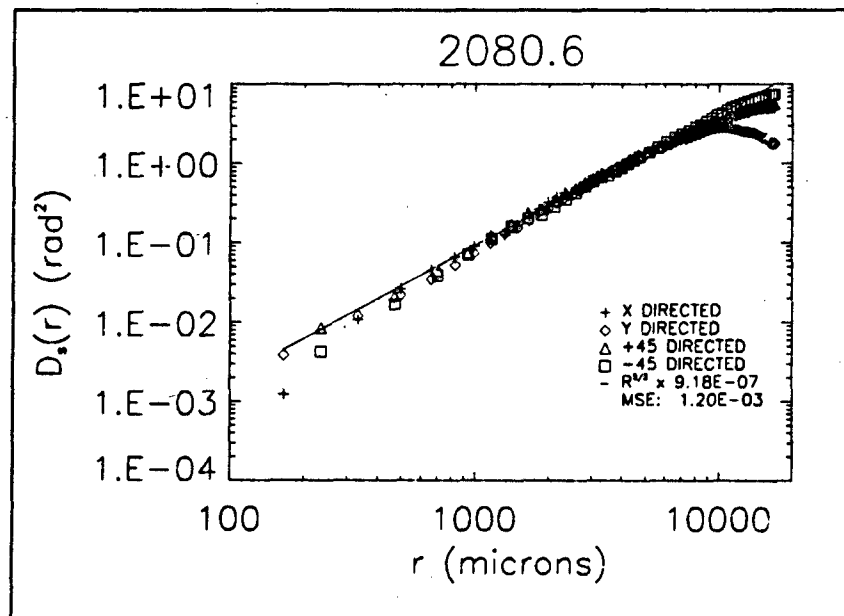


Figure D.7. $\hat{D}_s(r)$ for 2080, location 6. The fan voltage is 35 volts; the element voltage is 80 volts; there is no screen in the chamber; the average temperature is 56° C.

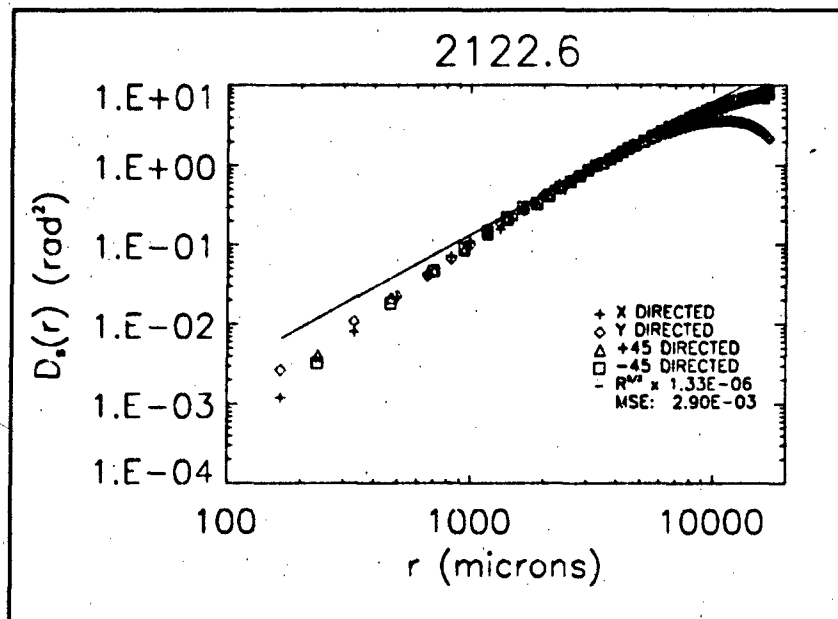


Figure D.8. $\hat{D}_s(r)$ for 2122, location 6. The fan voltage is 24 volts; the element voltage is 53 volts; there is one screen in the chamber; the average temperature is 42° C.

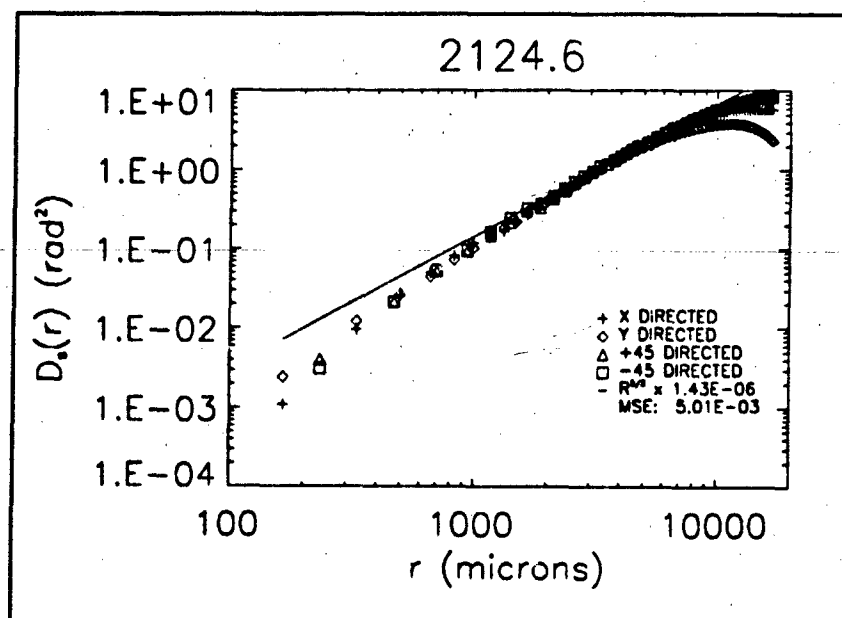


Figure D.9. $\hat{D}_s(r)$ for 2124, location 6. The fan voltage is 28 volts; the element voltage is 55 volts; there is one screen in the chamber; the average temperature is 42° C.

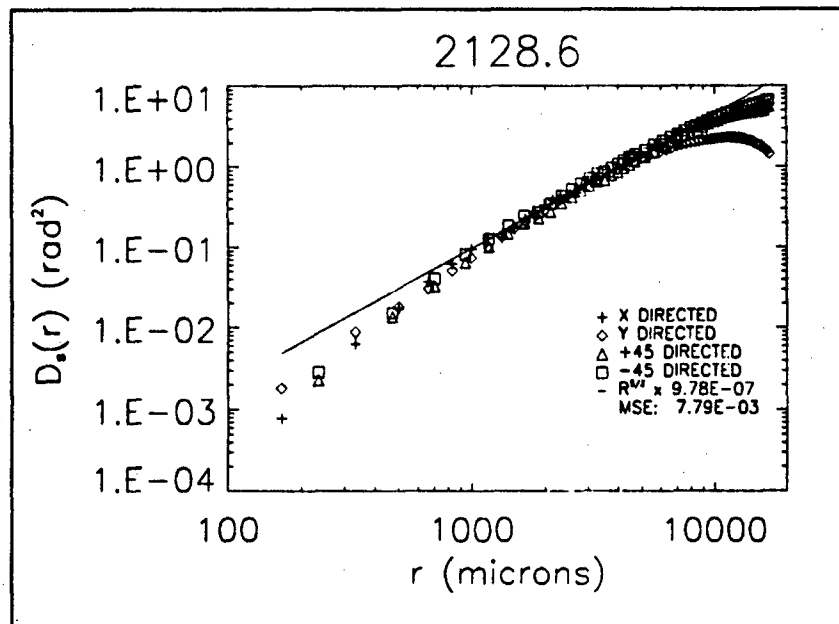


Figure D.10. $\hat{D}_s(r)$ for 2128, location 6. The fan voltage is 32 volts; the element voltage is 58 volts; there is one screen in the chamber; the average temperature is 42° C.

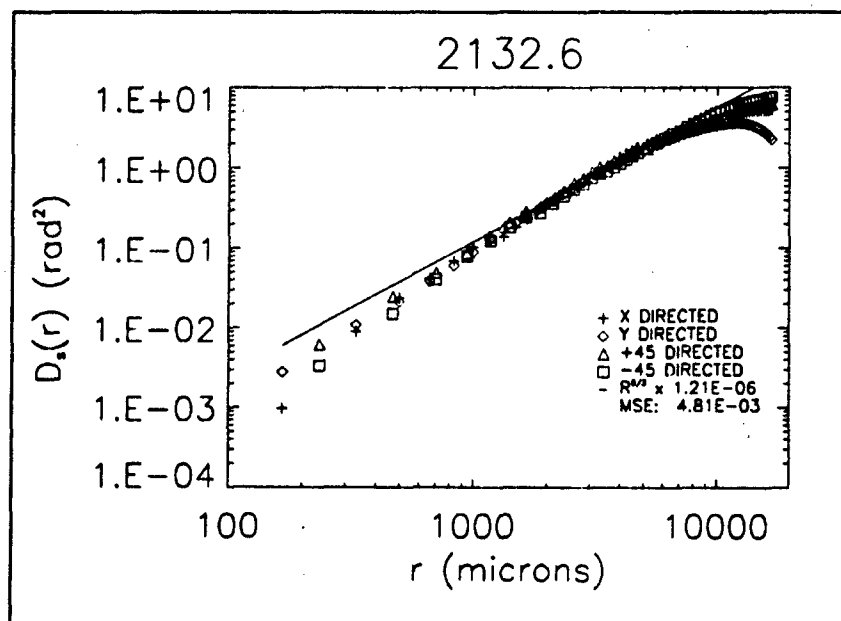


Figure D.11. $\hat{D}_s(r)$ for 2132, location 6. The fan voltage is 36 volts; the element voltage is 60 volts; there is one screen in the chamber; the average temperature is 42° C.

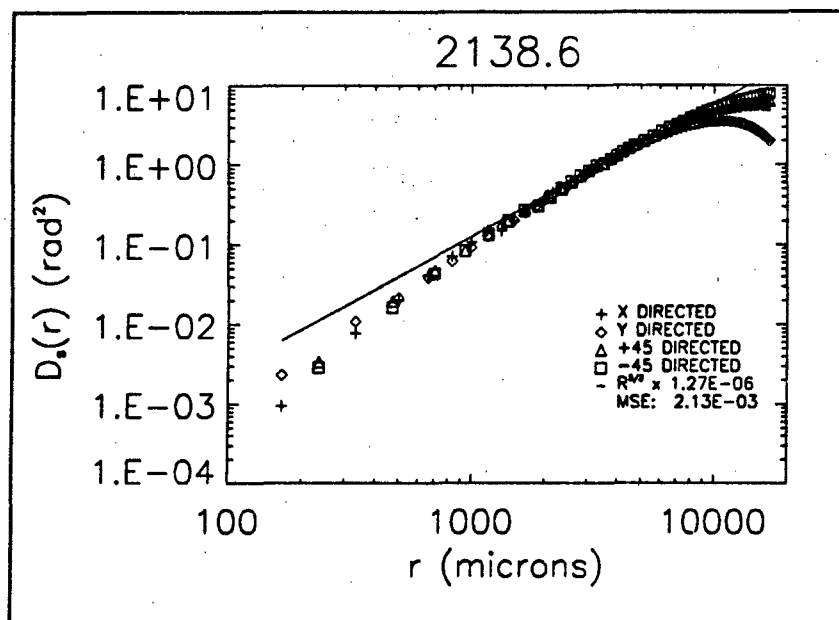


Figure D.12. $\hat{D}_s(r)$ for 2138, location 6. The fan voltage is 40 volts; the element voltage is 61 volts; there is one screen in the chamber; the average temperature is 42° C.

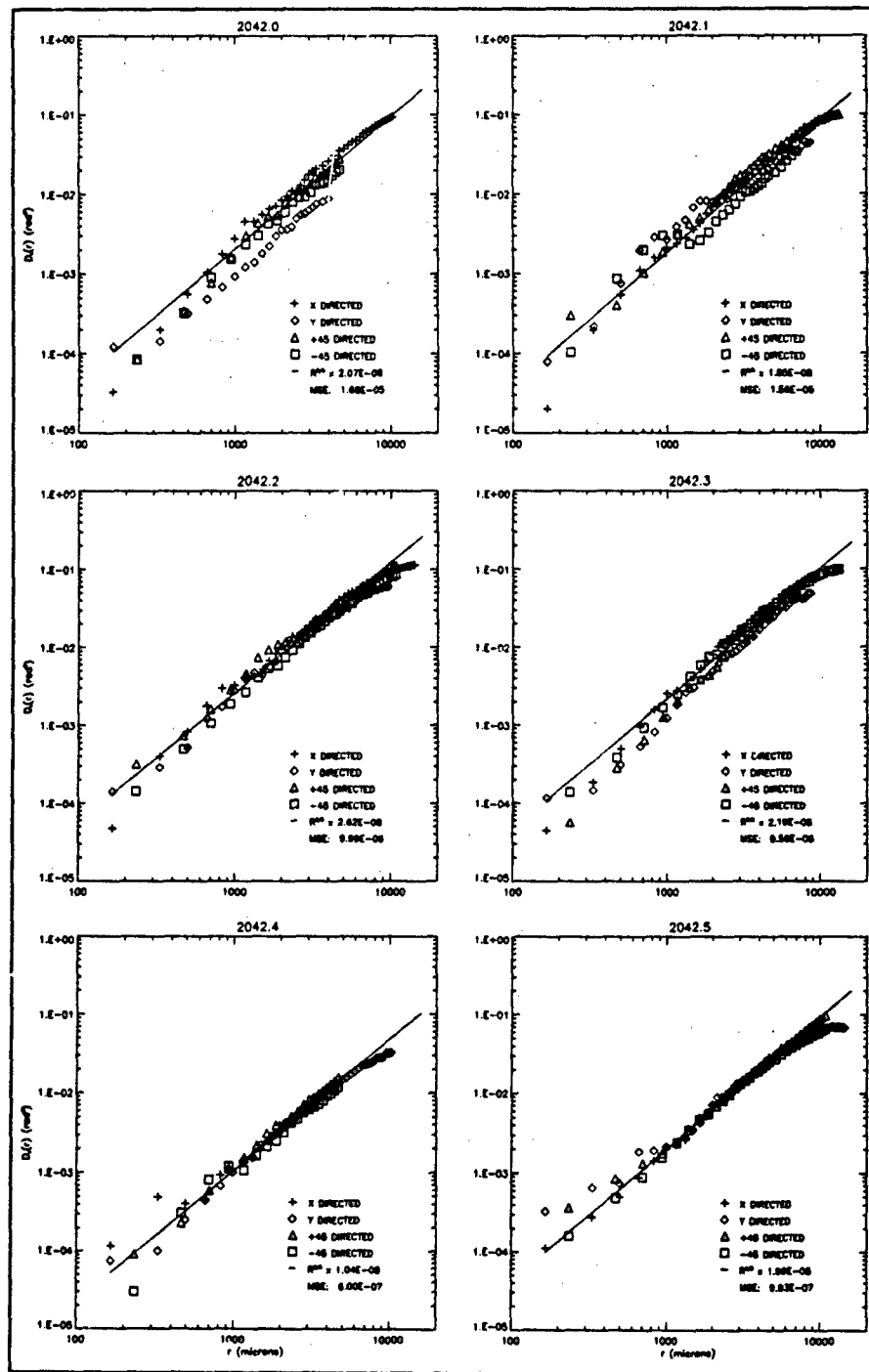


Figure D.13. $\hat{D}_s(r)$ for 2042, locations 0 - 5. The fan voltage is 20 volts; the element voltage is 35 volts; there is no screen in the chamber; the average temperature is 27° C.

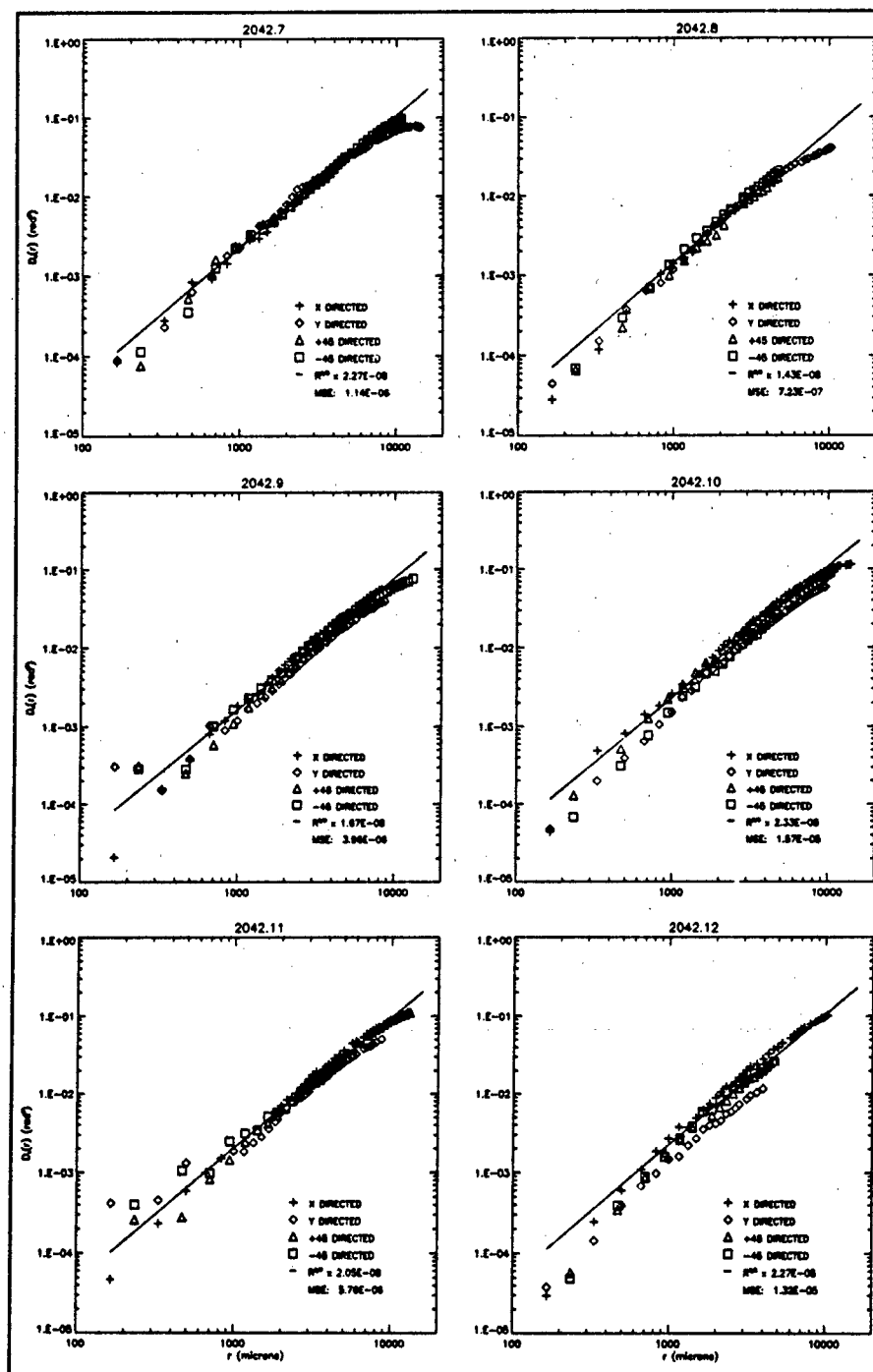


Figure D.14. $\hat{D}_s(r)$ for 2042, locations 7 - 12. The fan voltage is 20 volts; the element voltage is 35 volts; there is no screen in the chamber; the average temperature is 27° C.

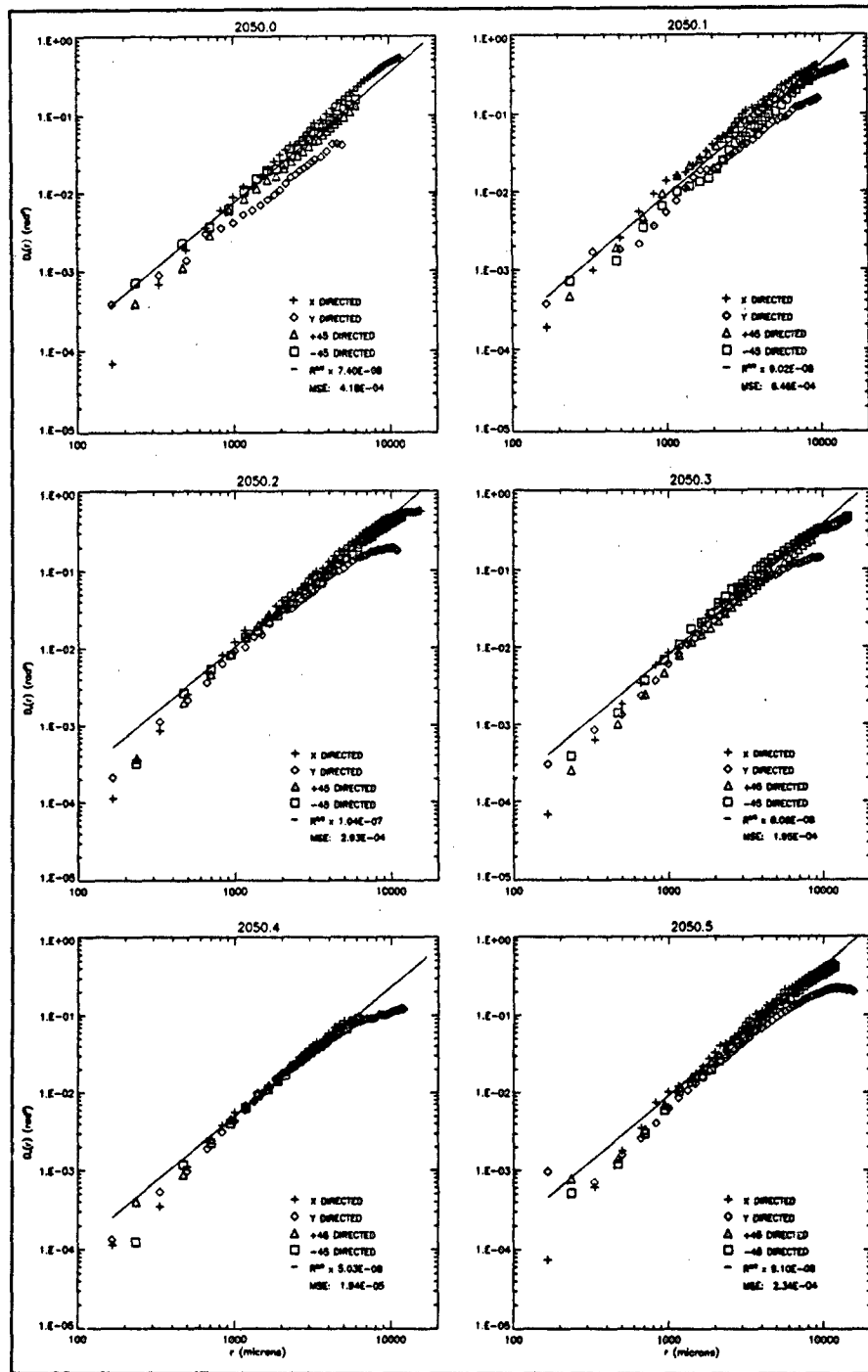


Figure D.15. $\hat{D}_s(r)$ for 2050, locations 0 - 5. The fan voltage is 20 volts; the element voltage is 50 volts; there is no screen in the chamber; the average temperature is 35° C.

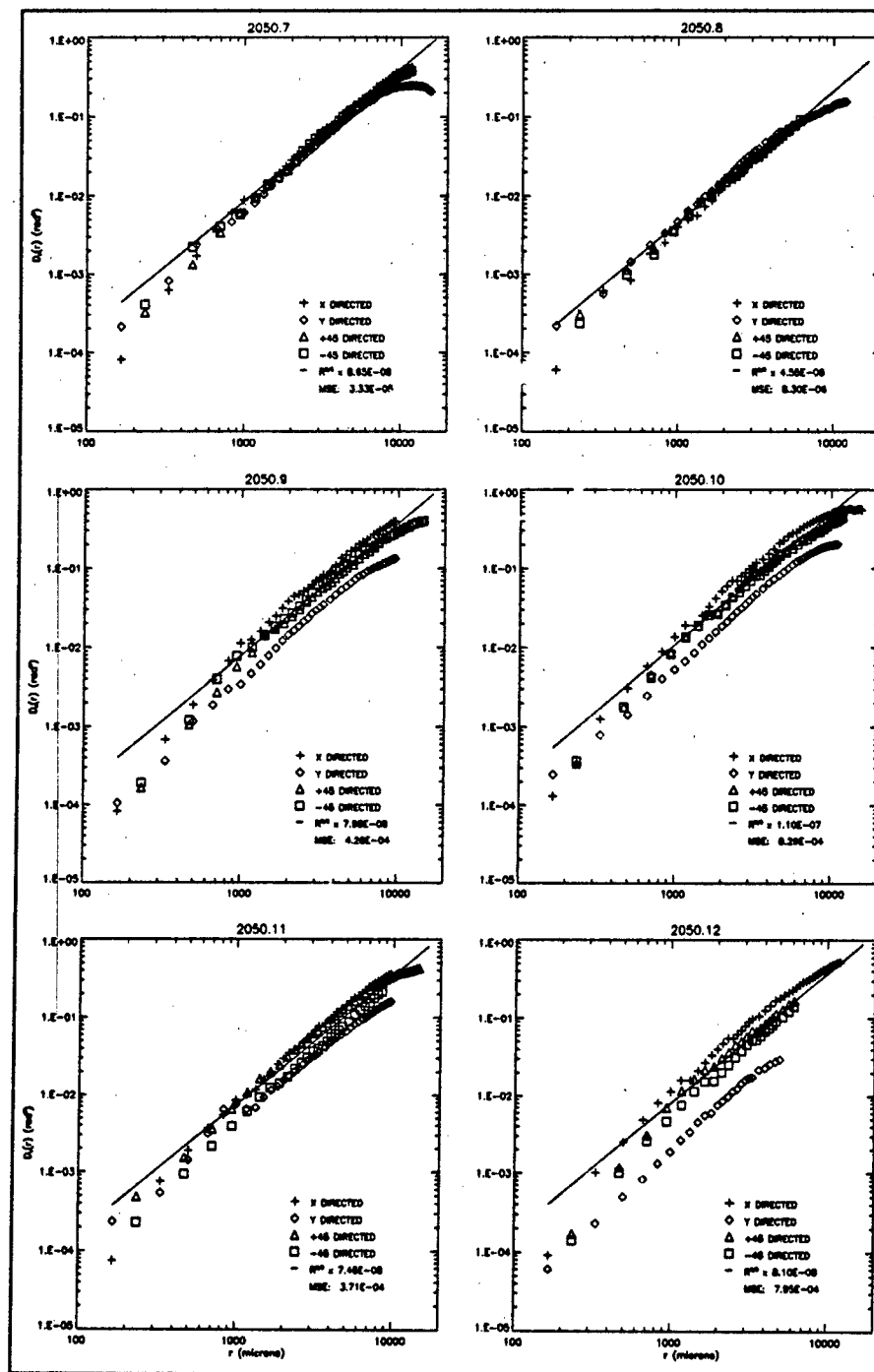


Figure D.16. $\hat{D}_s(r)$ for 2050, locations 7 - 12. The fan voltage is 20 volts; the element voltage is 50 volts; there is no screen in the chamber; the average temperature is 35° C.

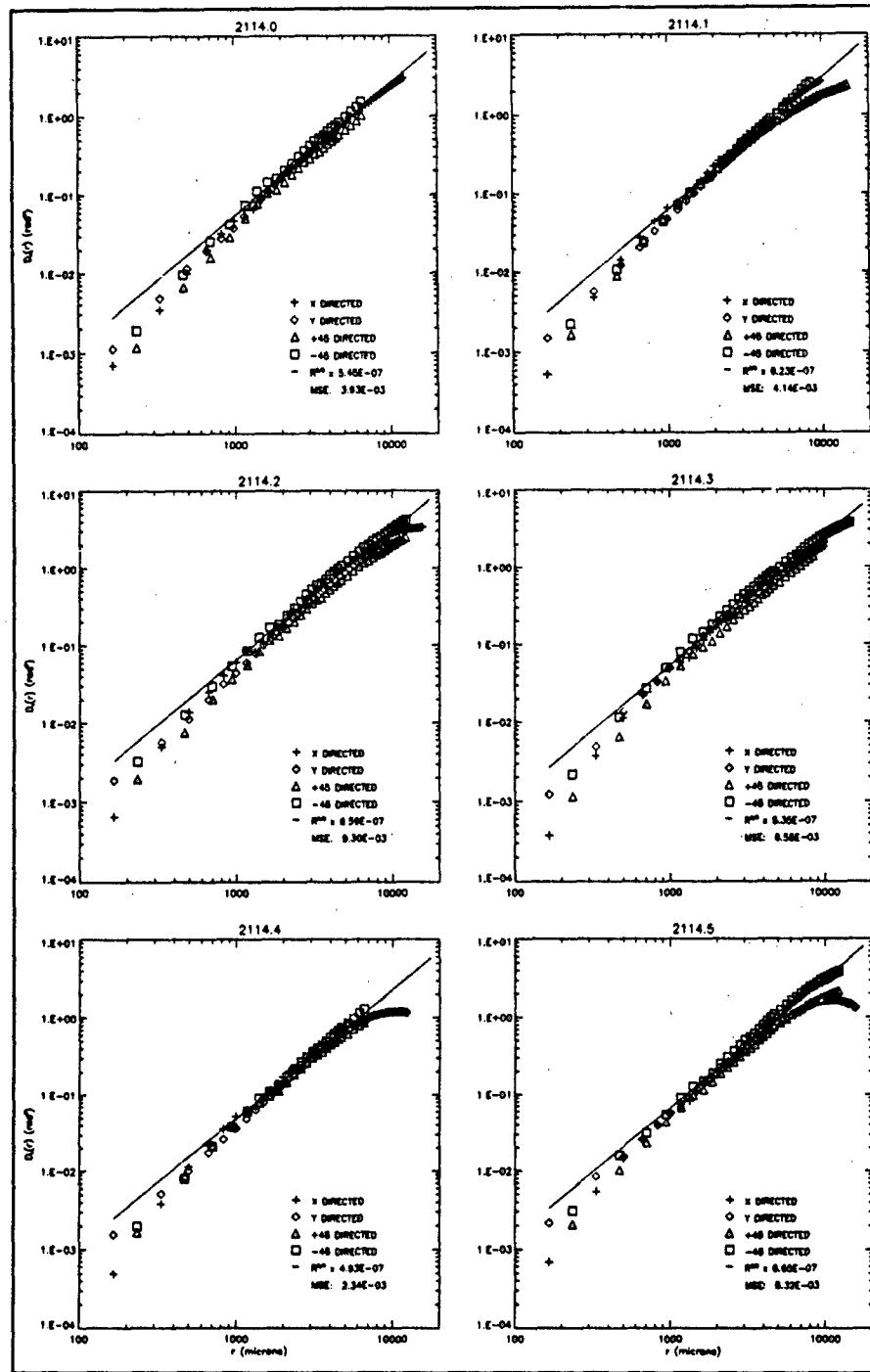


Figure D.17. $\hat{D}_s(r)$ for 2114, locations 0 - 5. The fan voltage is 20 volts; the element voltage is 65 volts; there is no screen in the chamber; the average temperature is 49° C.

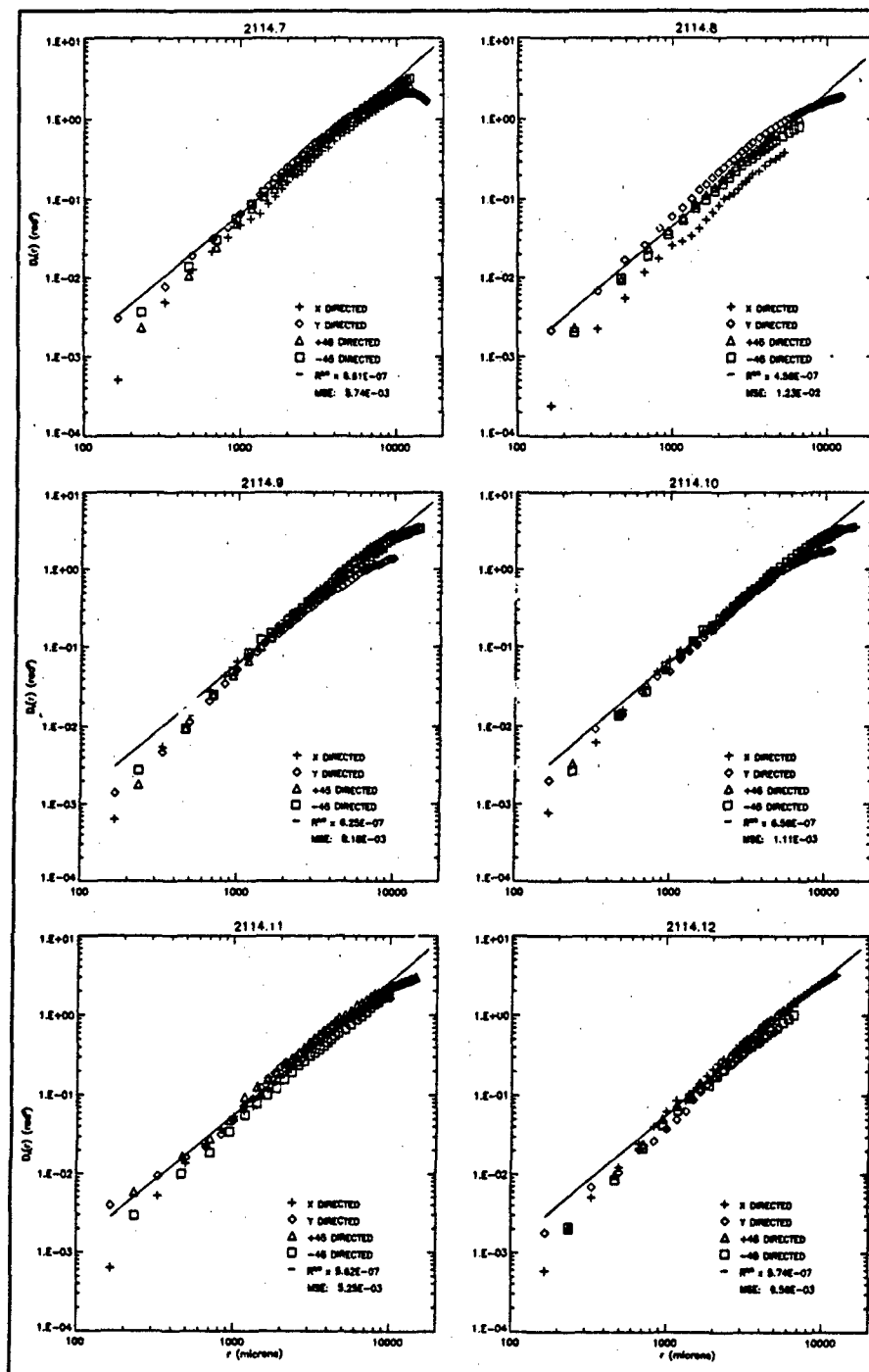


Figure D.18. $\hat{D}_s(r)$ for 2114, locations 7 - 12. The fan voltage is 20 volts; the element voltage is 65 volts; there is no screen in the chamber; the average temperature is 49° C.

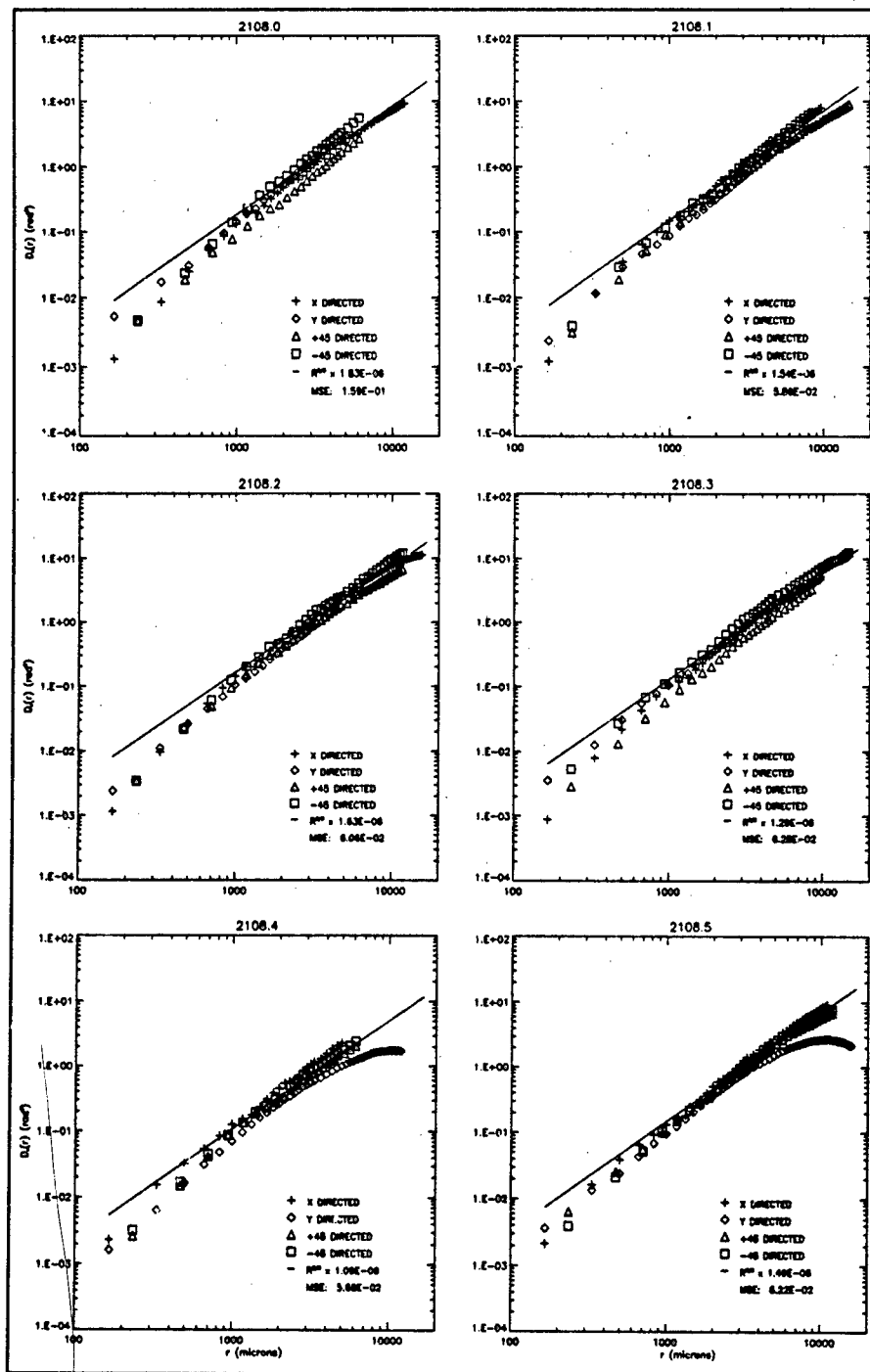


Figure D.19. $\hat{D}_s(r)$ for 2108, locations 0 - 5. The fan voltage is 20 volts; the element voltage is 80 volts; there is no screen in the chamber; the average temperature is 73° C.

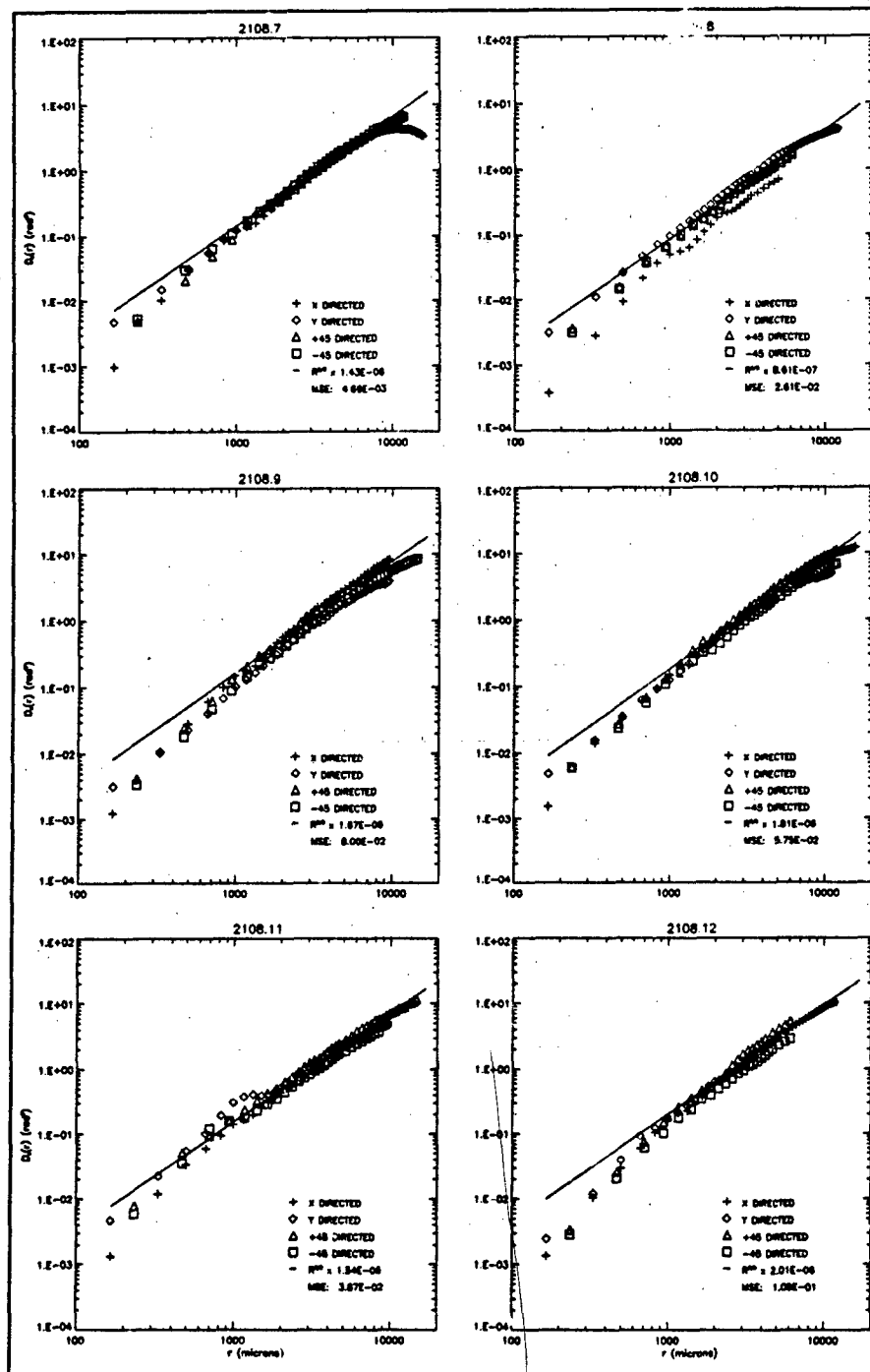


Figure D.20. $\bar{D}_s(r)$ for 2108, locations 7 - 12. The fan voltage is 20 volts; the element voltage is 80 volts; there is no screen in the chamber; the average temperature is 73° C.

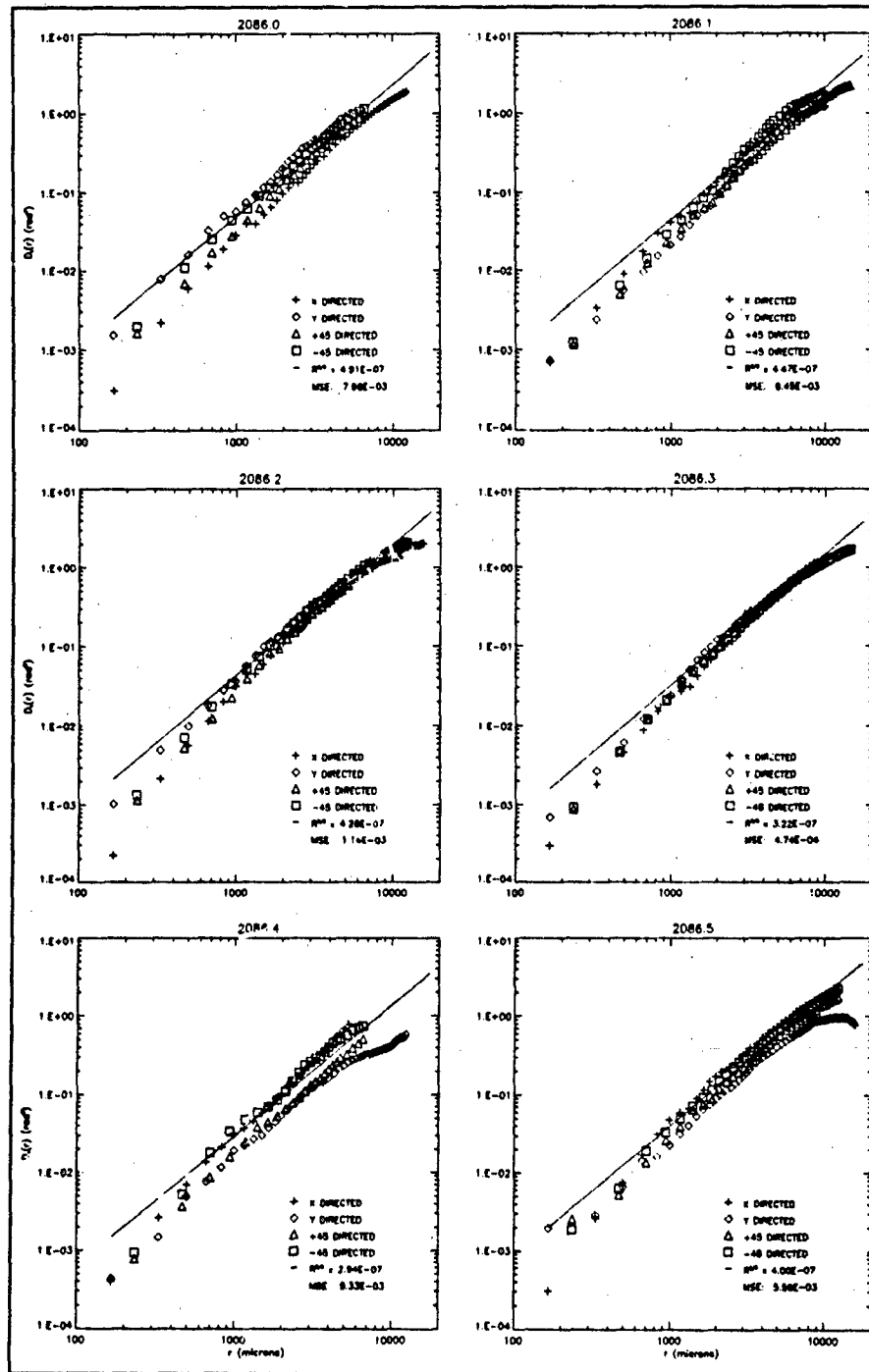


Figure D.21. $\hat{D}_s(\tau)$ for 2086, locations 0 - 5. The fan voltage is 20 volts; the element voltage is 35 volts; there is one screen in the chamber; the average temperature is 32° C.

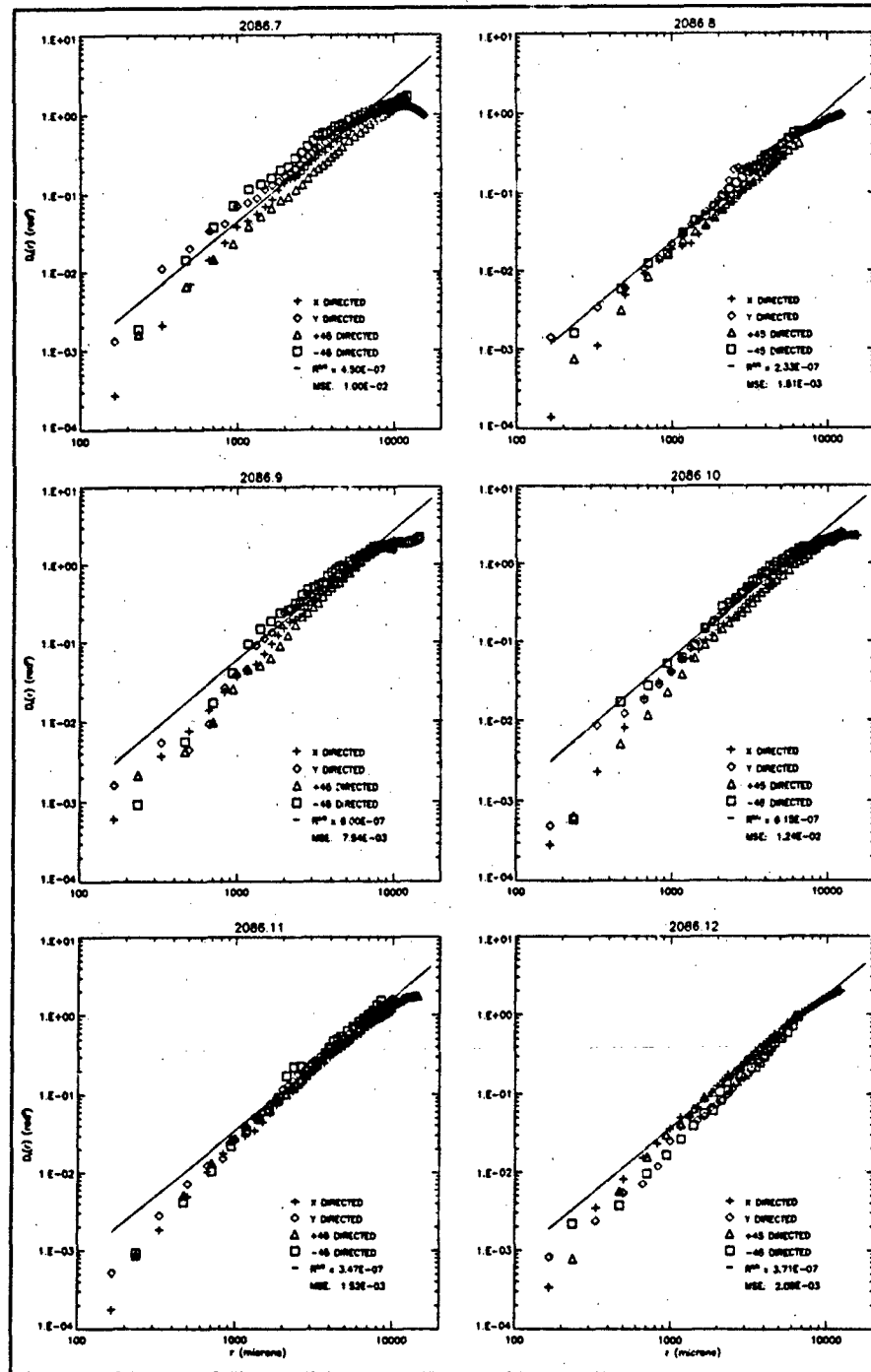


Figure D.22. $\hat{D}_s(r)$ for 2086, locations 7 – 12. The fan voltage is 20 volts; the element voltage is 35 volts; there is one screen in the chamber; the average temperature is 32° C.

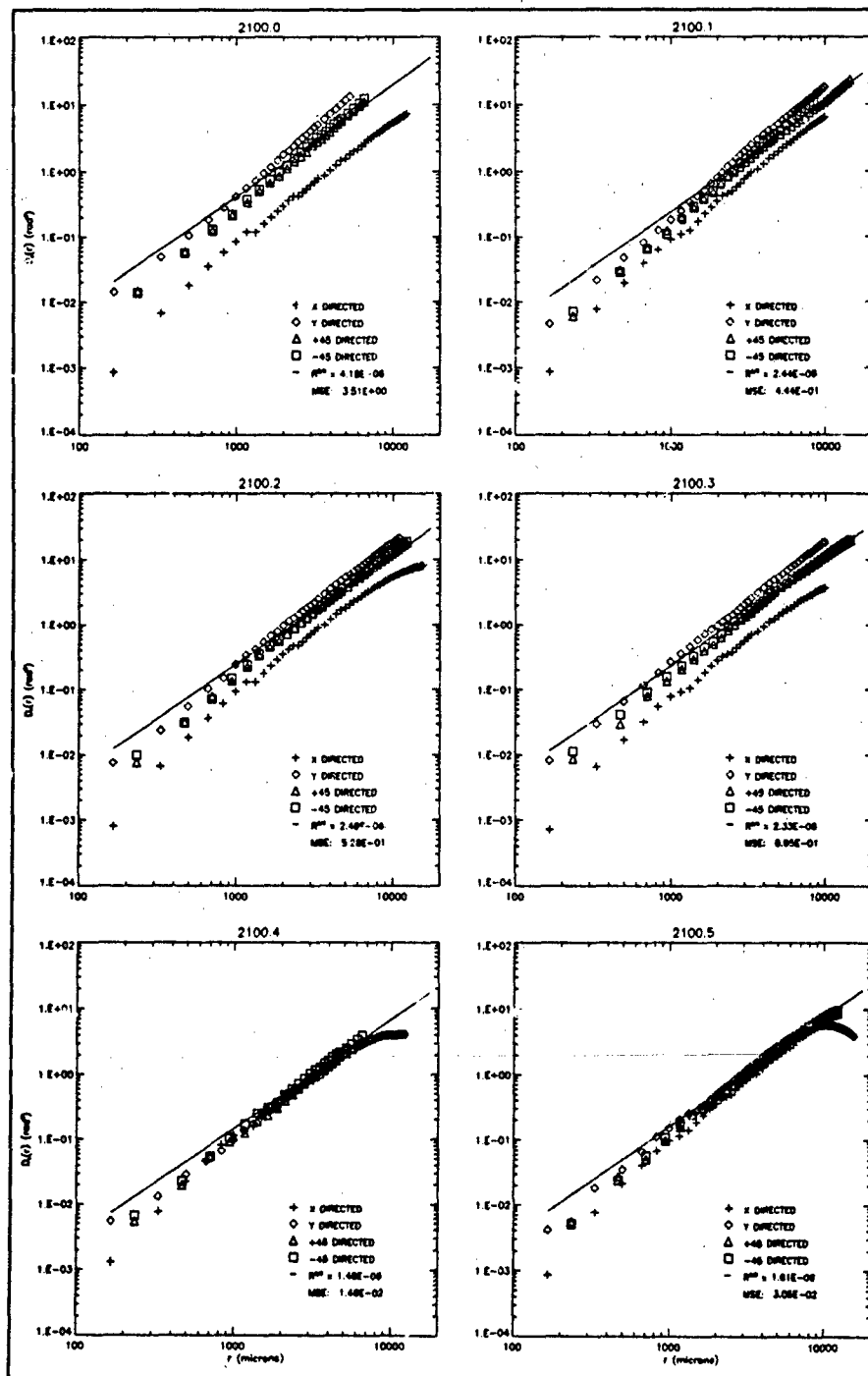


Figure D.23. $\hat{D}_s(r)$ for 2100, locations 0 - 5. The fan voltage is 20 volts; the element voltage is 65 volts; there is one screen in the chamber; the average temperature is 60° C.

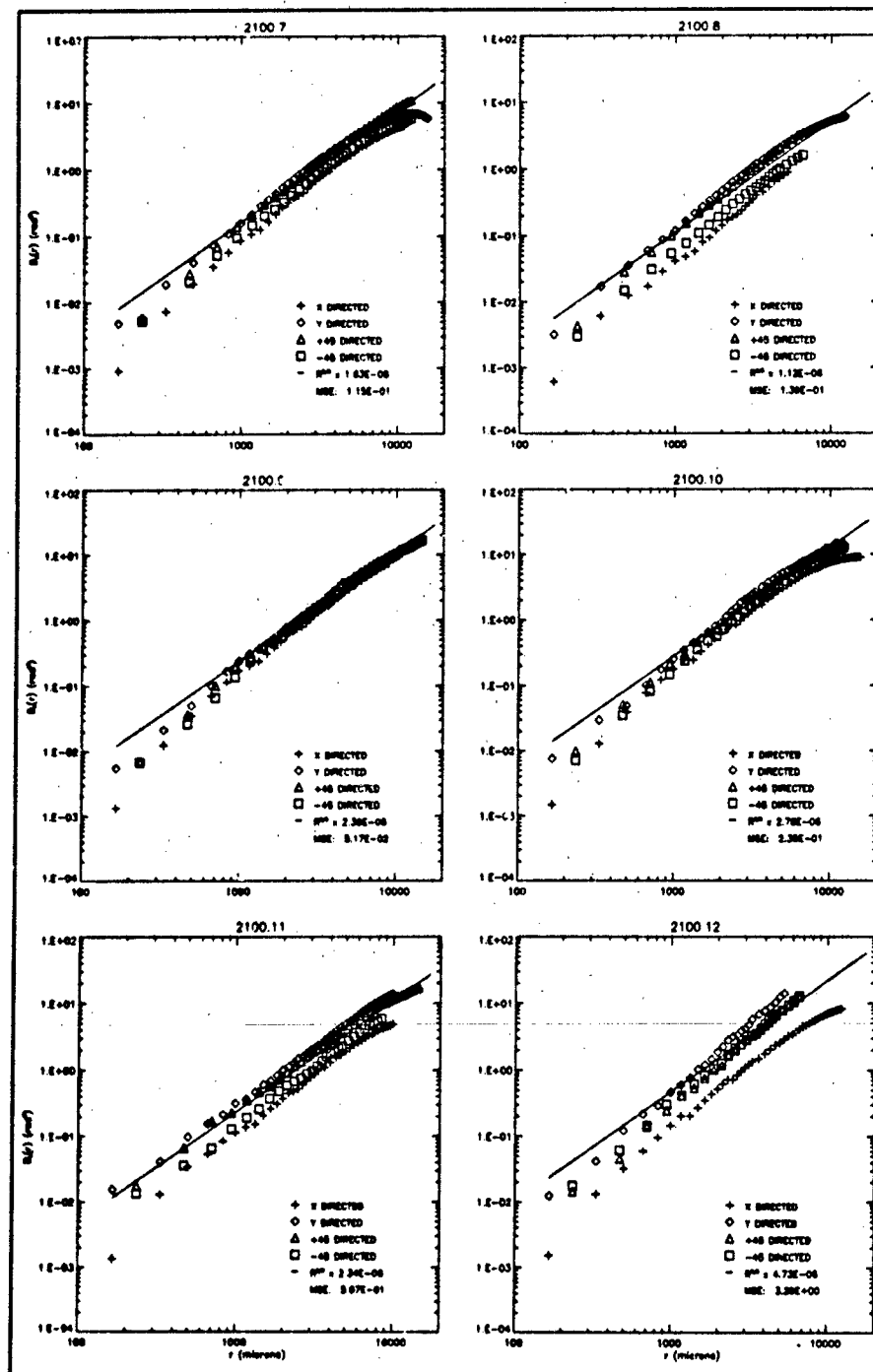


Figure D.24. $\hat{D}_s(r)$ for 2100, locations 7 - 12. The fan voltage is 20 volts; the element voltage is 65 volts; there is one screen in the chamber; the average temperature is 60° C.

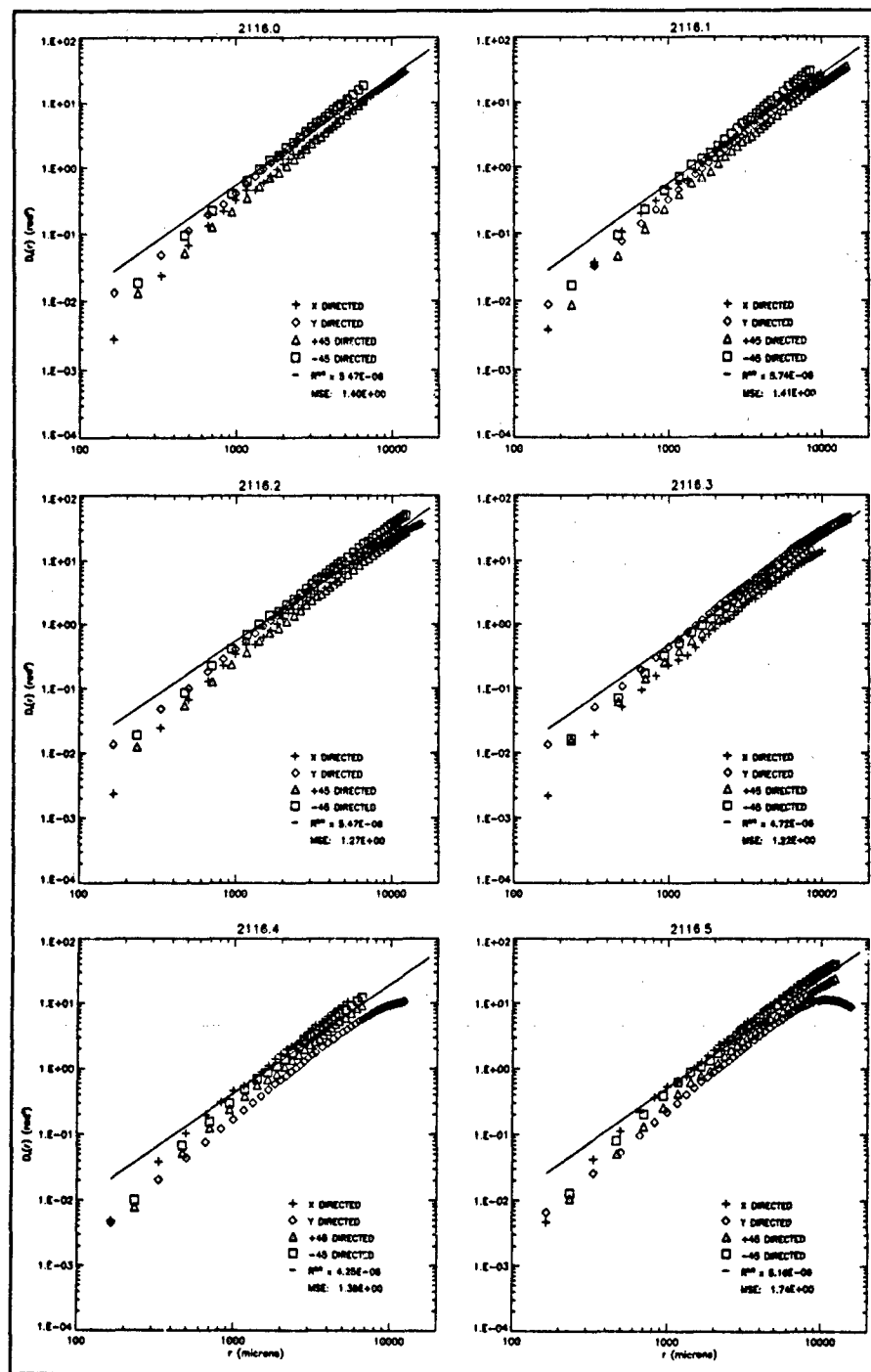


Figure D.25. $\hat{D}_s(r)$ for 2116, locations 0 - 5. The fan voltage is 20 volts; the element voltage is 80 volts; there is one screen in the chamber; the average temperature is 83° C.

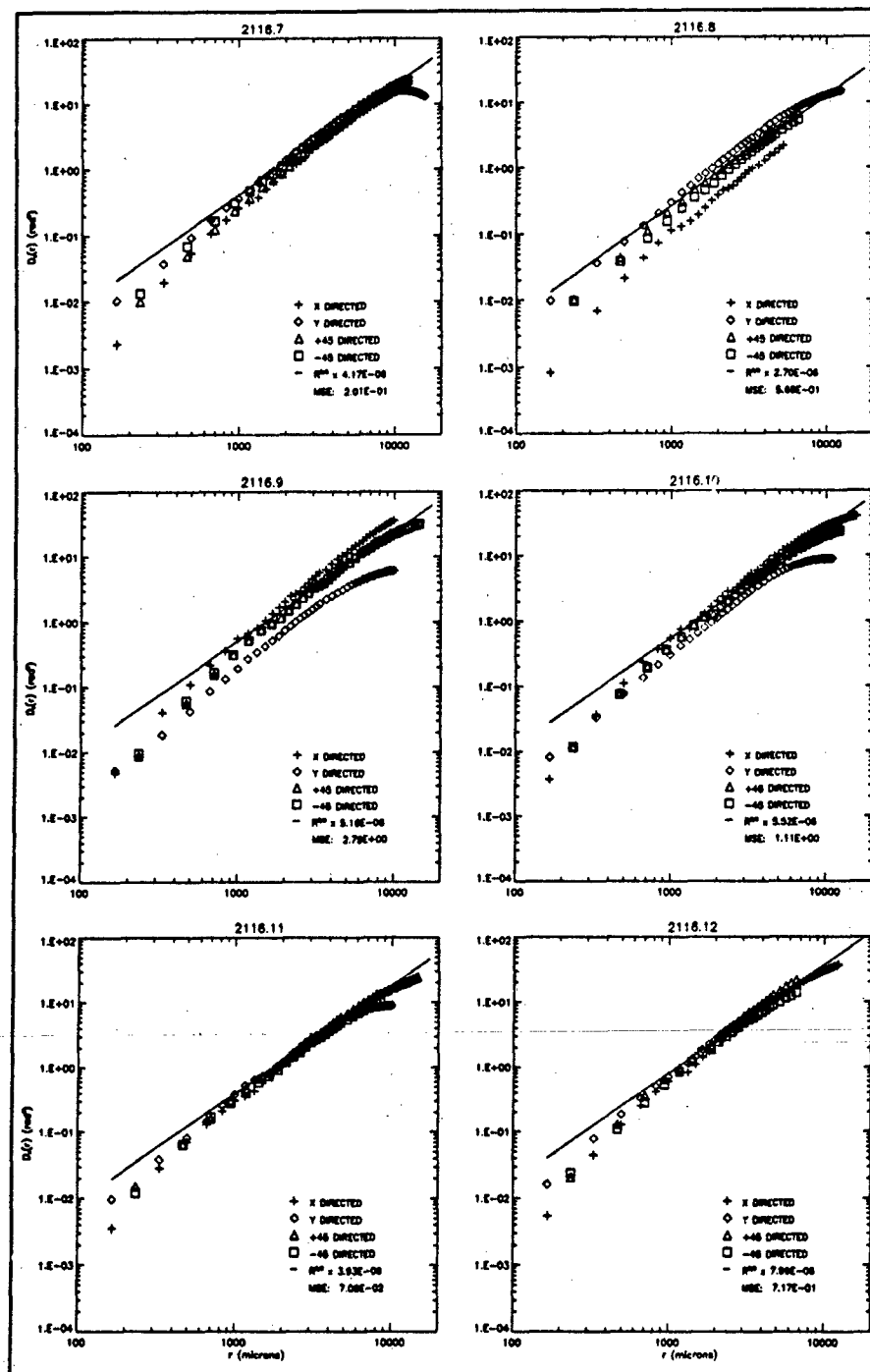


Figure D.26. $\hat{D}_s(r)$ for 2116, locations 7 - 12. The fan voltage is 20 volts; the element voltage is 80 volts; there is one screen in the chamber; the average temperature is 83°C .

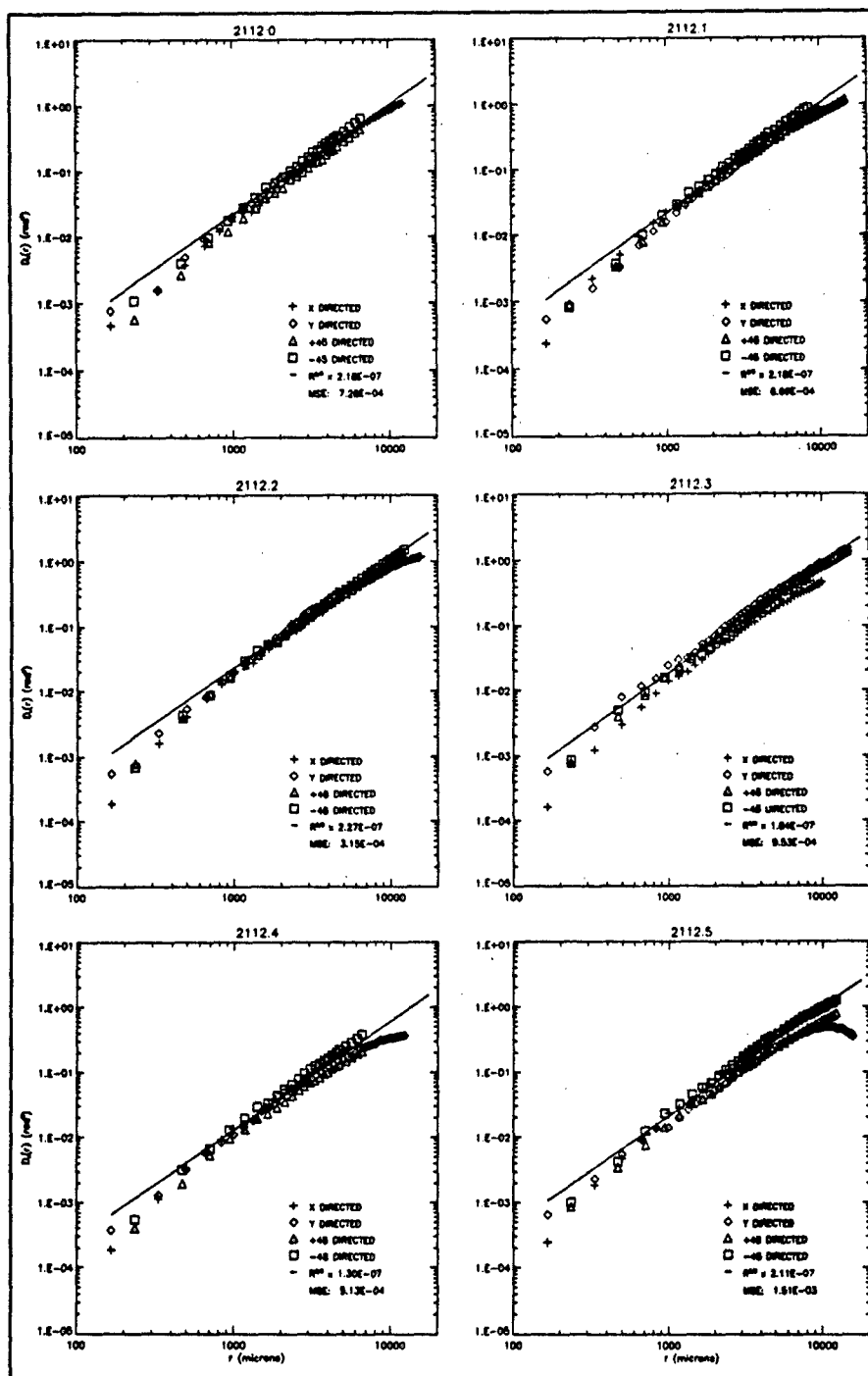


Figure D.27. $\hat{D}_s(r)$ for 2112, locations 0 - 5. The fan voltage is 35 volts; the element voltage is 50 volts; there is no screen in the chamber; the average temperature is 35° C.

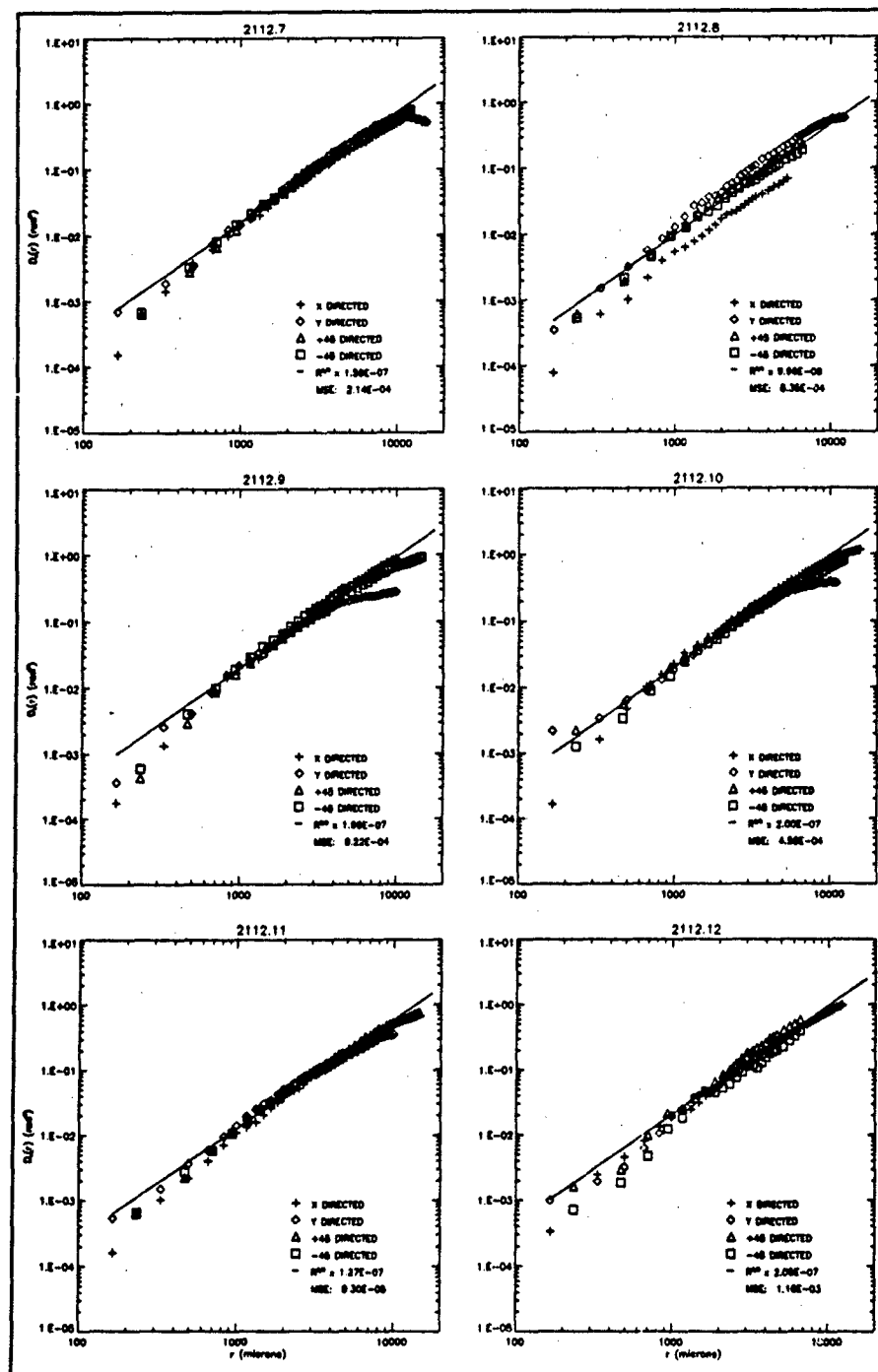


Figure D.28. $\hat{D}_s(r)$ for 2112, locations 7 - 12. The fan voltage is 35 volts; the element voltage is 50 volts; there is no screen in the chamber; the average temperature is 35° C.

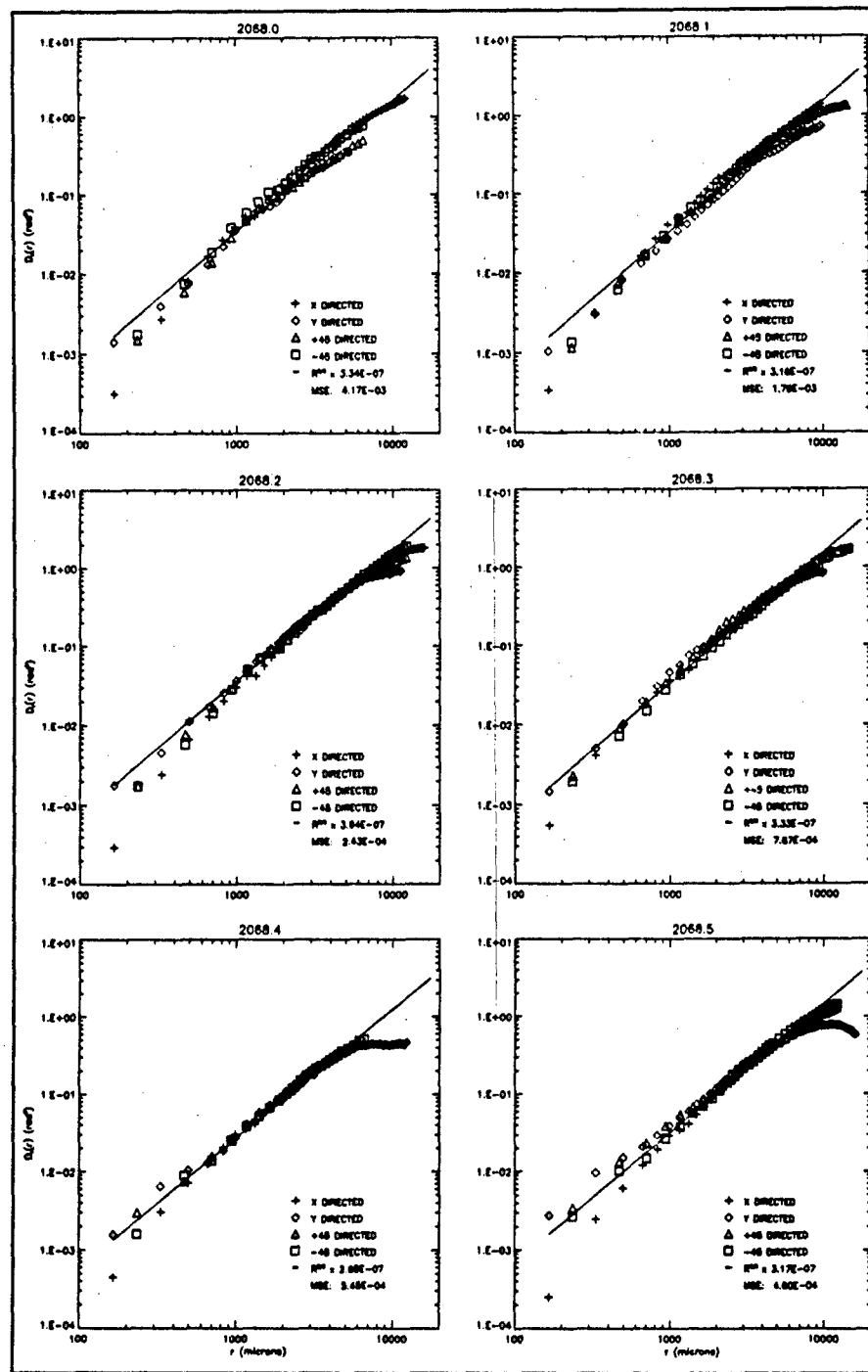


Figure D.29. $\bar{D}_s(r)$ for 2068, locations 0 - 5. The fan voltage is 35 volts; the element voltage is 65 volts; there is no screen in the chamber; the average temperature is 44° C.

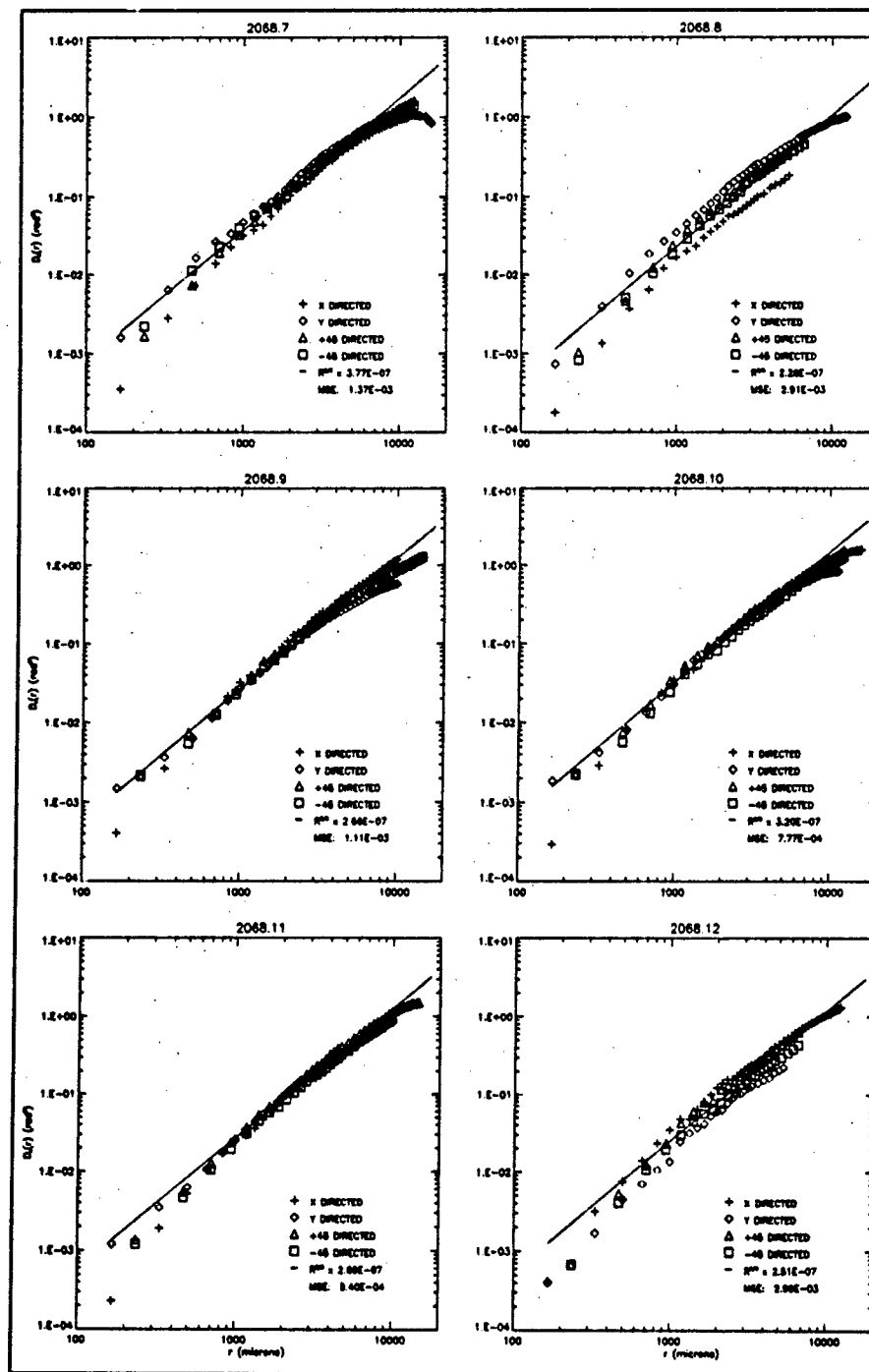


Figure D.30. $\hat{D}_s(r)$ for 2068, locations 7 - 12. The fan voltage is 35 volts; the element voltage is 65 volts; there is no screen in the chamber; the average temperature is 44° C.

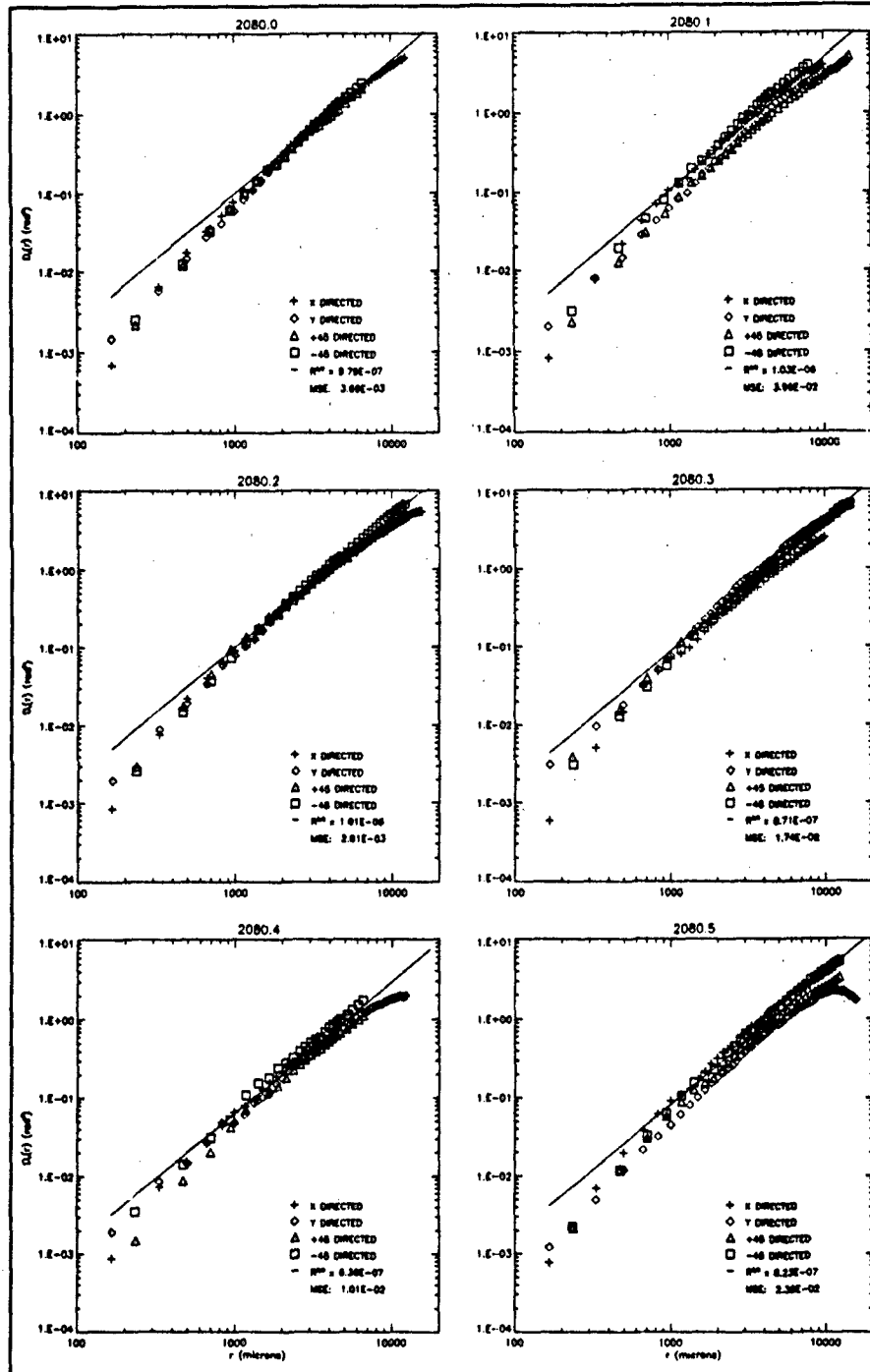


Figure D.31. $\bar{D}_s(r)$ for 2080, locations 0 - 5. The fan voltage is 35 volts; the element voltage is 80 volts; there is no screen in the chamber; the average temperature is 56°C .

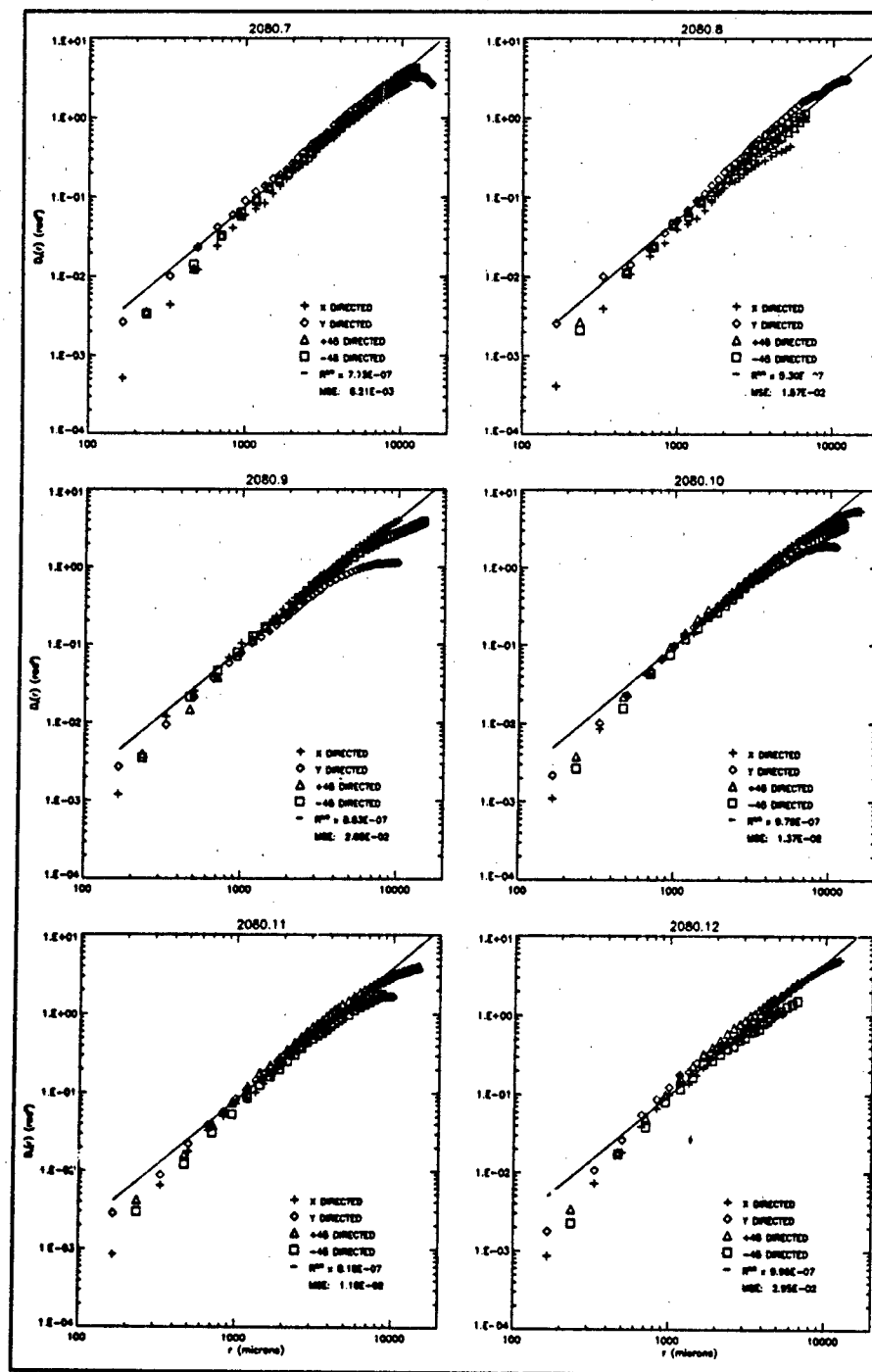


Figure D.32. $\hat{D}_s(r)$ for 2080, locations 7 - 12. The fan voltage is 35 volts; the element voltage is 80 volts; there is no screen in the chamber; the average temperature is 56° C.

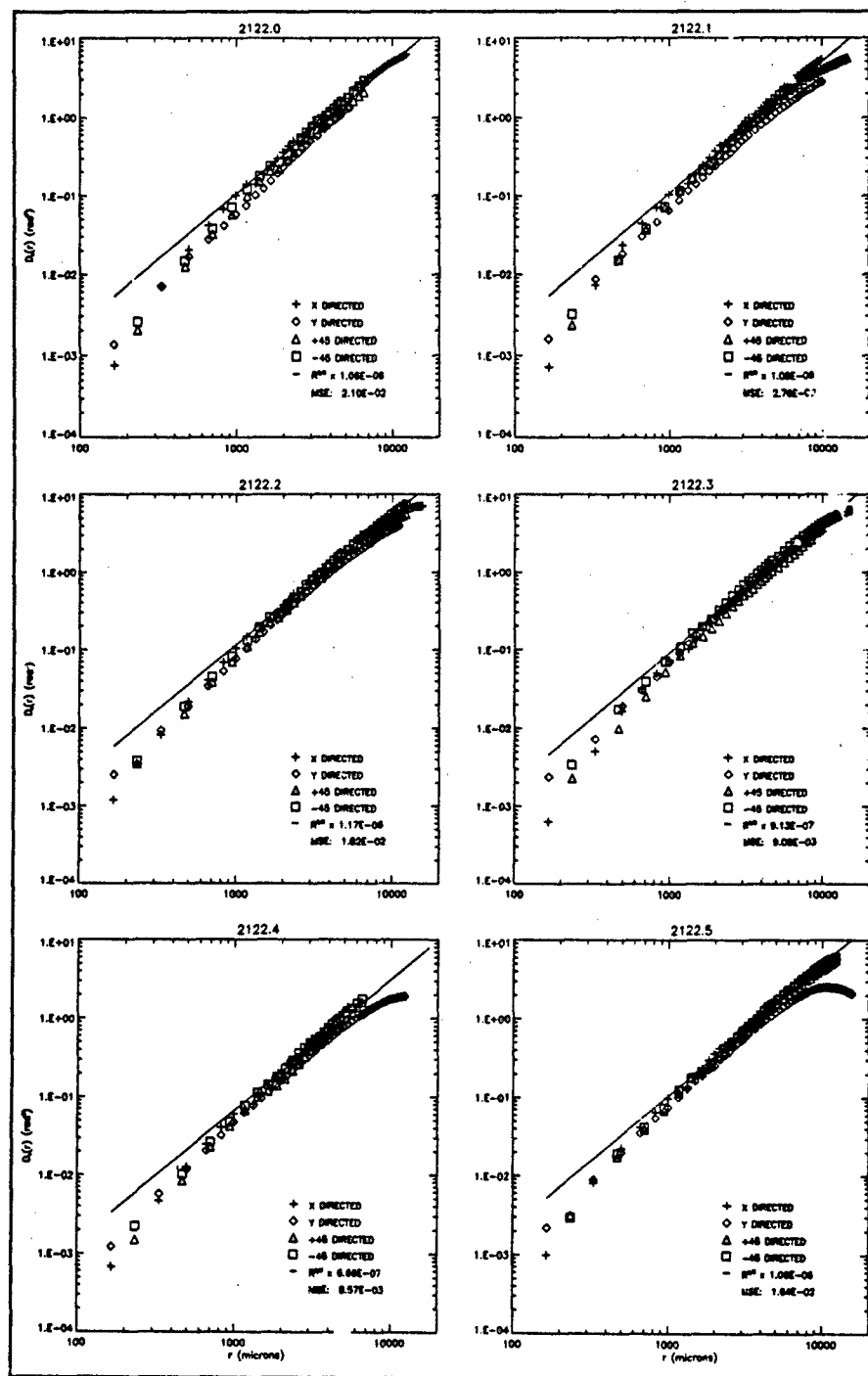


Figure D.33. $\hat{D}_s(r)$ for 2122, locations 0 - 5. The fan voltage is 24 volts; the element voltage is 53 volts; there is one screen in the chamber; the average temperature is 42° C.

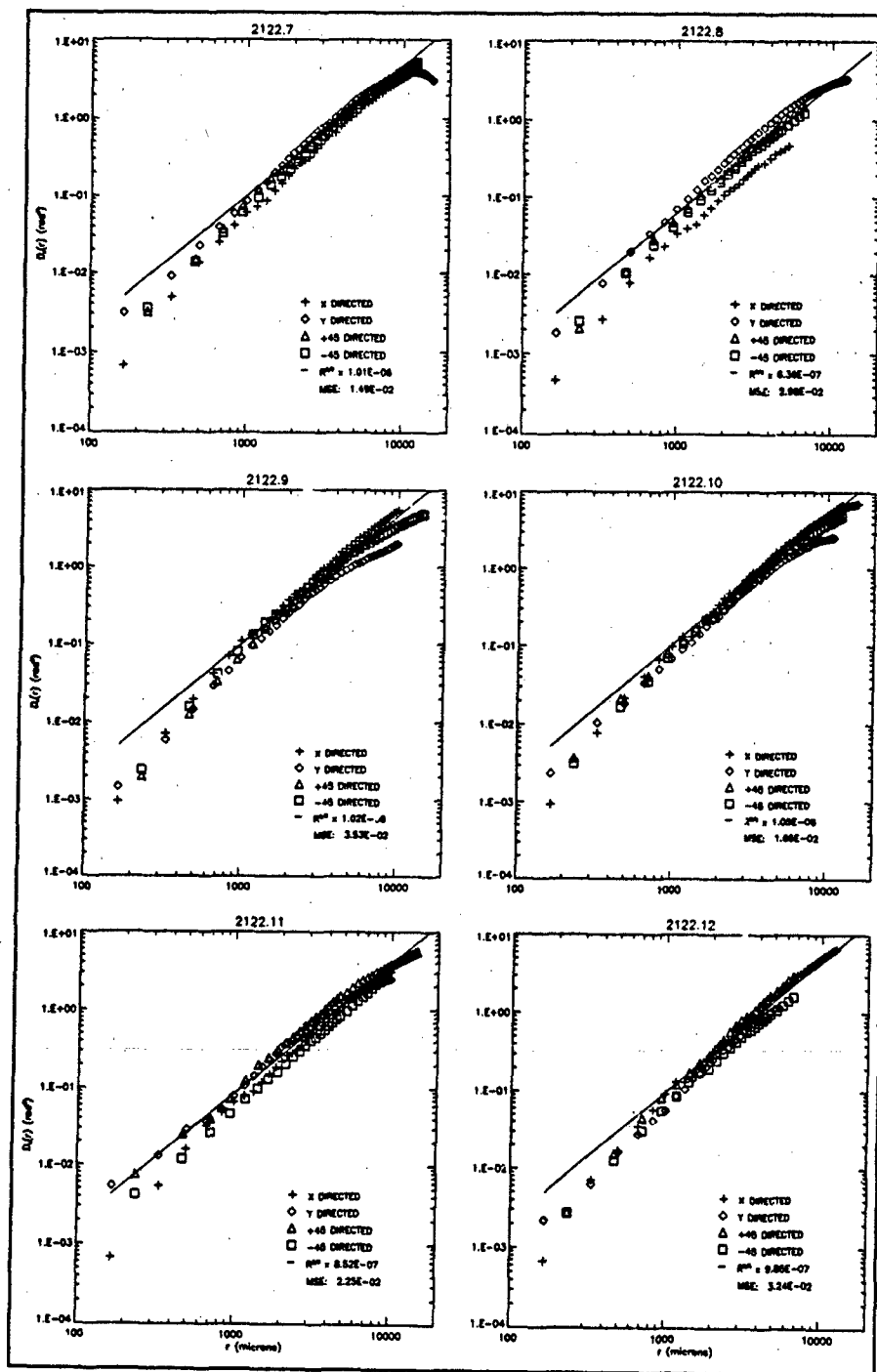


Figure D.34. $\hat{D}_s(r)$ for 2122, locations 7 - 12. The fan voltage is 24 volts; the element voltage is 53 volts; there is one screen in the chamber; the average temperature is 42° C.

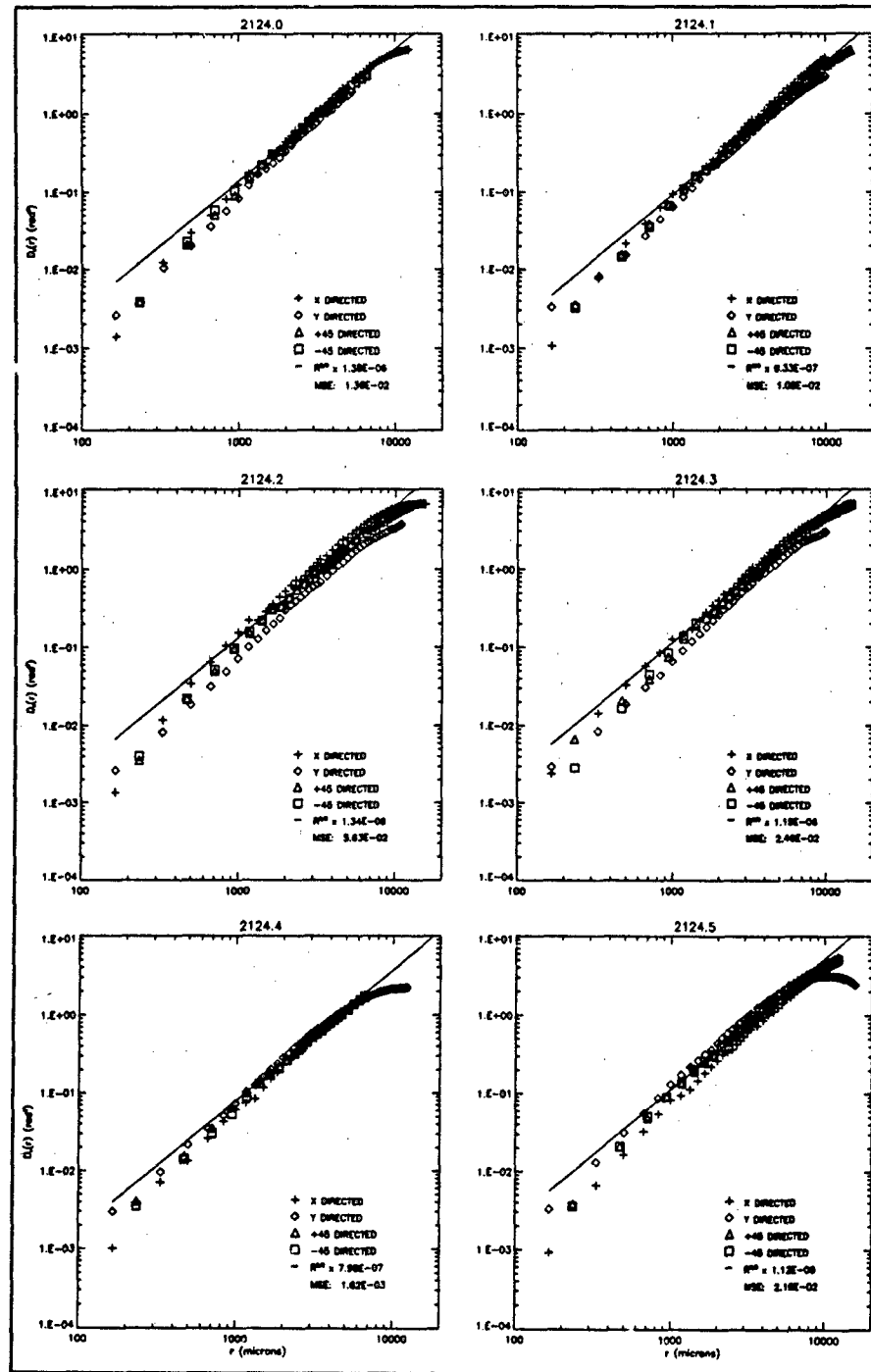


Figure D.35. $\hat{D}_s(r)$ for 2124, locations 0 - 5. The fan voltage is 28 volts; the element voltage is 55 volts; there is one screen in the chamber; the average temperature is 42° C.

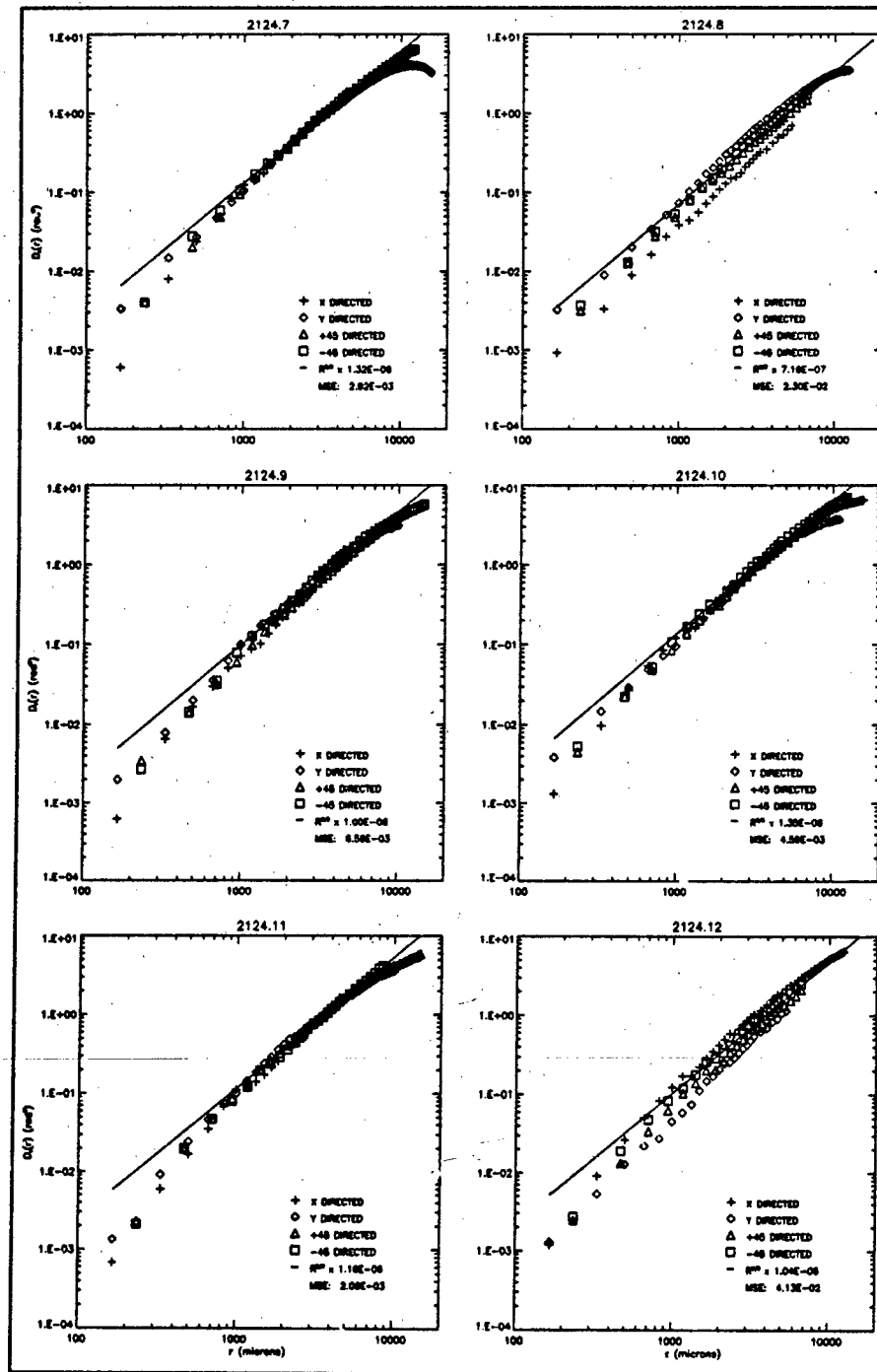


Figure D.36. $\hat{D}_s(r)$ for 2124, locations 7 - 12. The fan voltage is 28 volts; the element voltage is 55 volts; there is one screen in the chamber; the average temperature is 42° C.

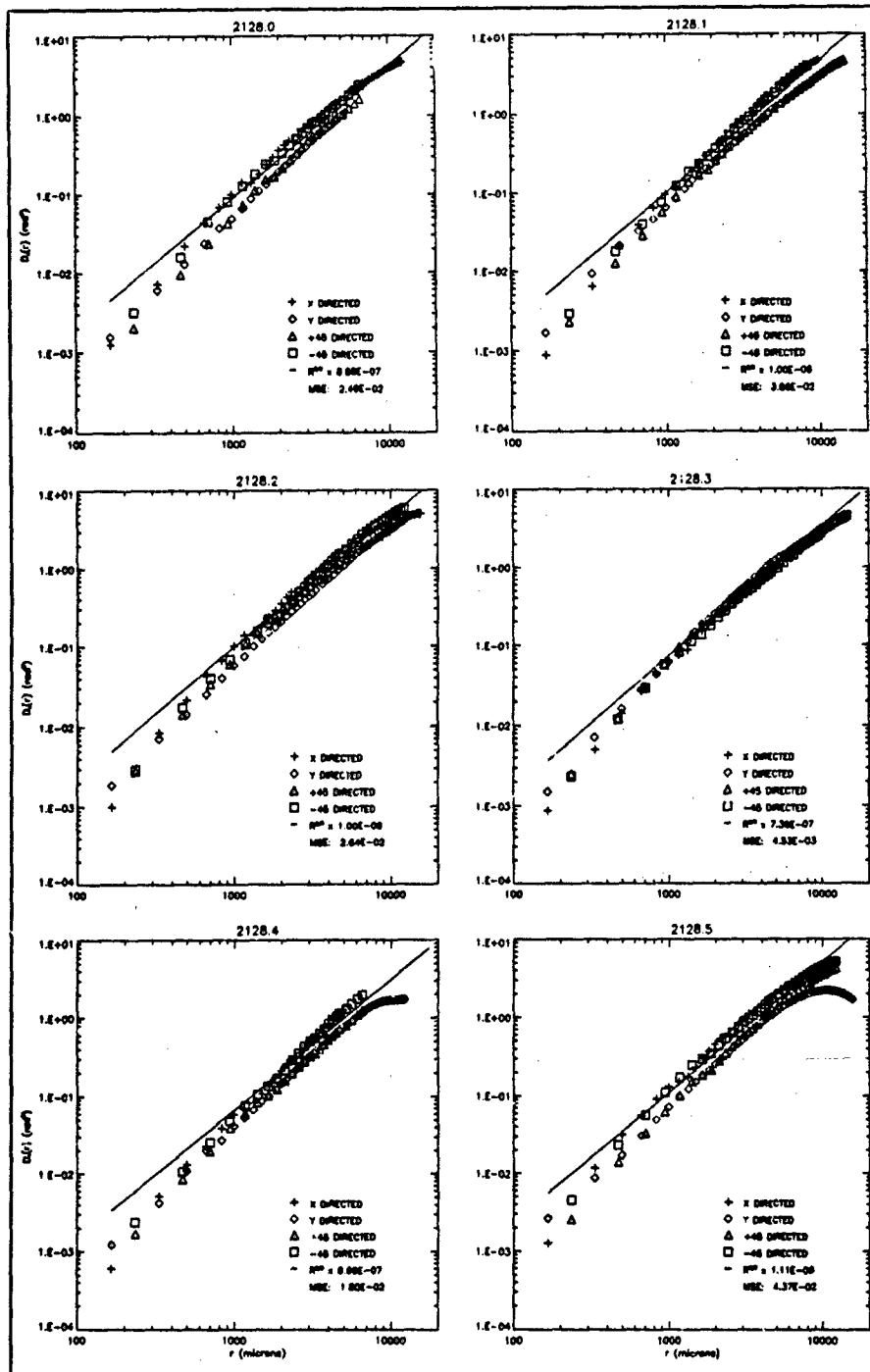


Figure D.37. $D_s(r)$ for 2128, locations 0 - 5. The fan voltage is 32 volts; the element voltage is 58 volts; there is one screen in the chamber; the average temperature is 42° C.

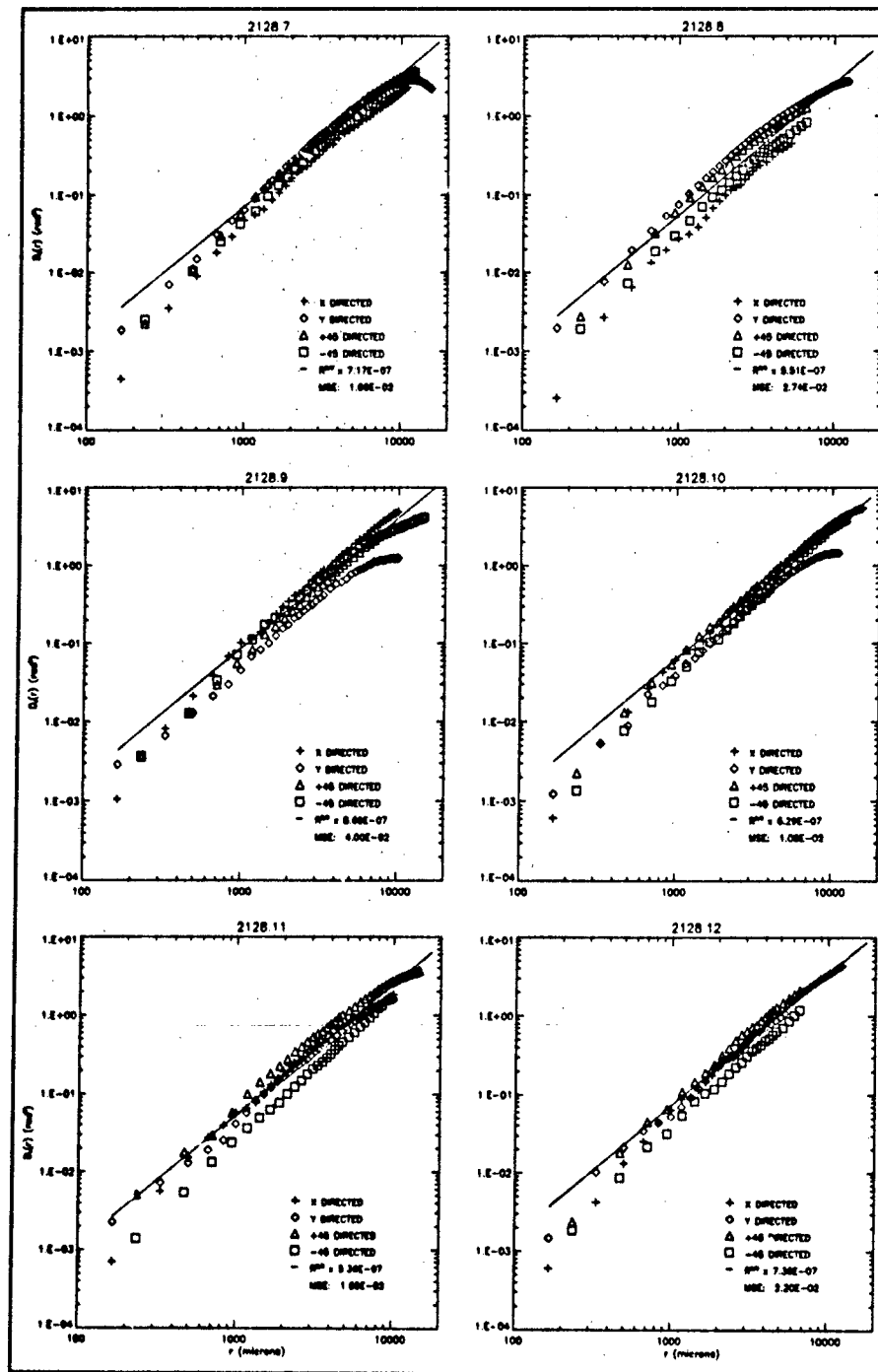


Figure D.38. $\hat{D}_s(r)$ for 2128, locations 7 - 12. The fan voltage is 32 volts; the element voltage is 58 volts; there is one screen in the chamber; the average temperature is 42° C.

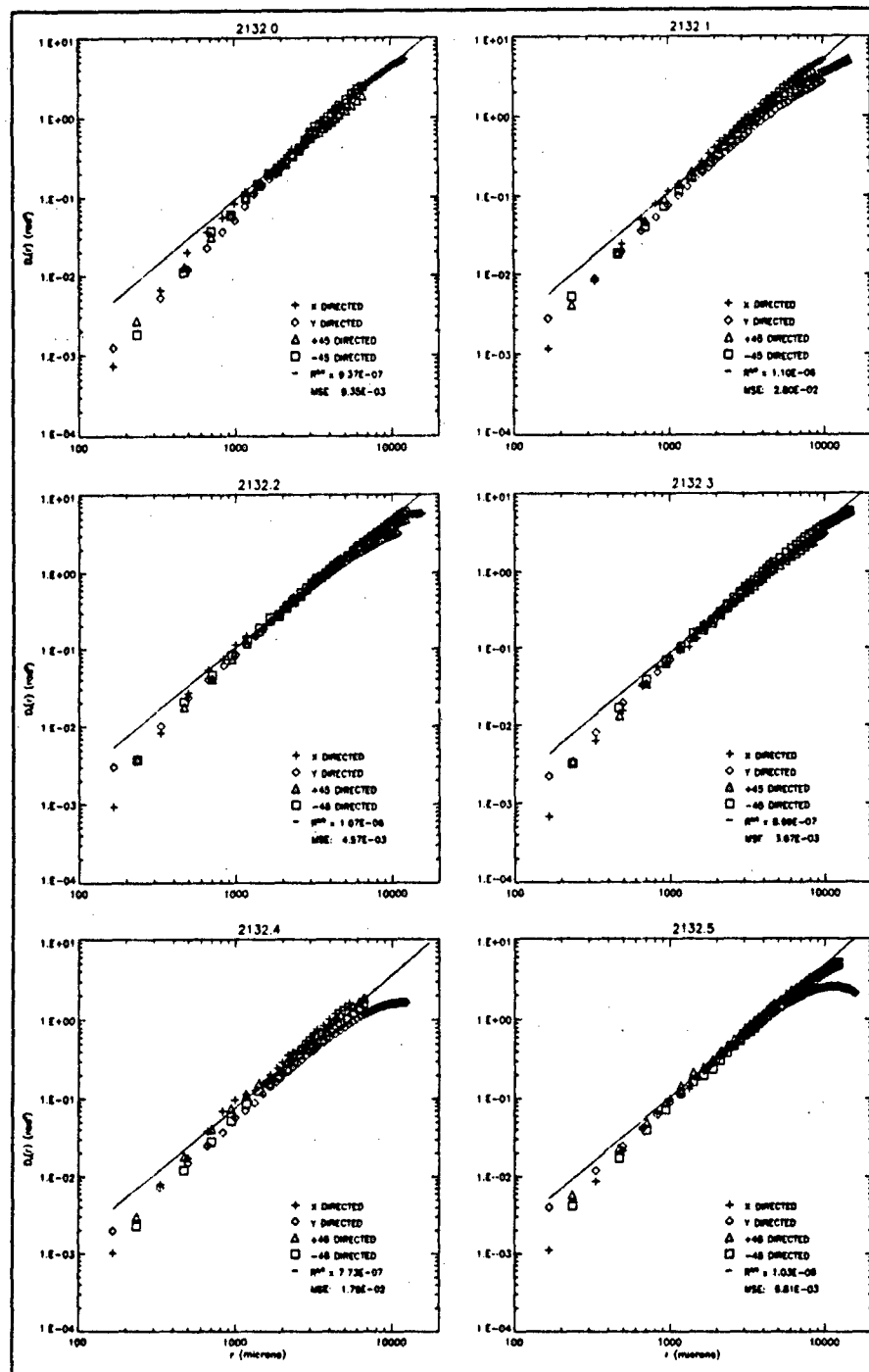


Figure D.39. $\hat{D}_s(r)$ for 2132, locations 0 - 5. The fan voltage is 36 volts; the element voltage is 60 volts; there is one screen in the chamber; the average temperature is 42° C.

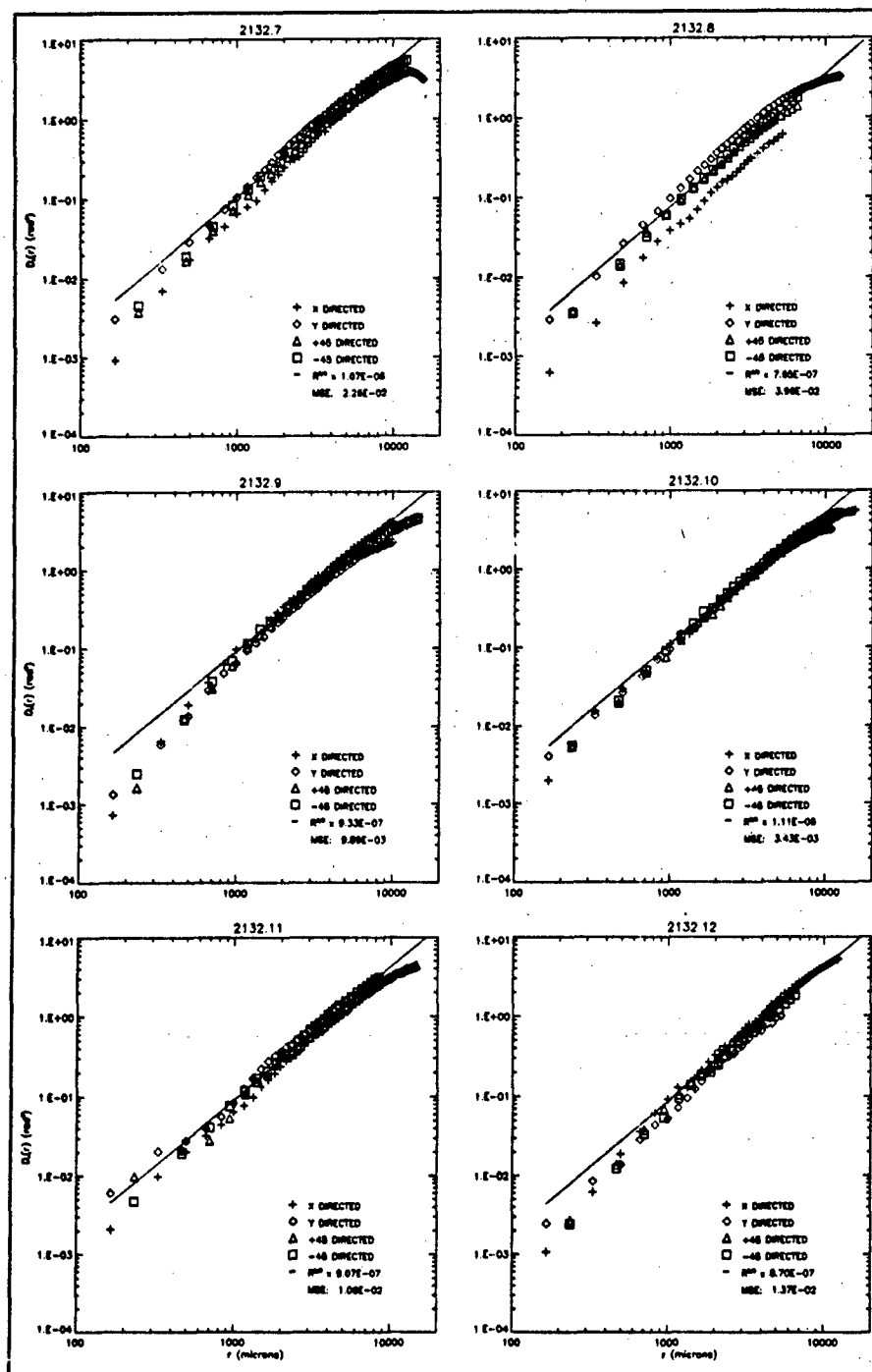


Figure D.40. $\hat{D}_s(r)$ for 2132, locations 7 - 12. The fan voltage is 36 volts; the element voltage is 60 volts; there is one screen in the chamber; the average temperature is 42° C.

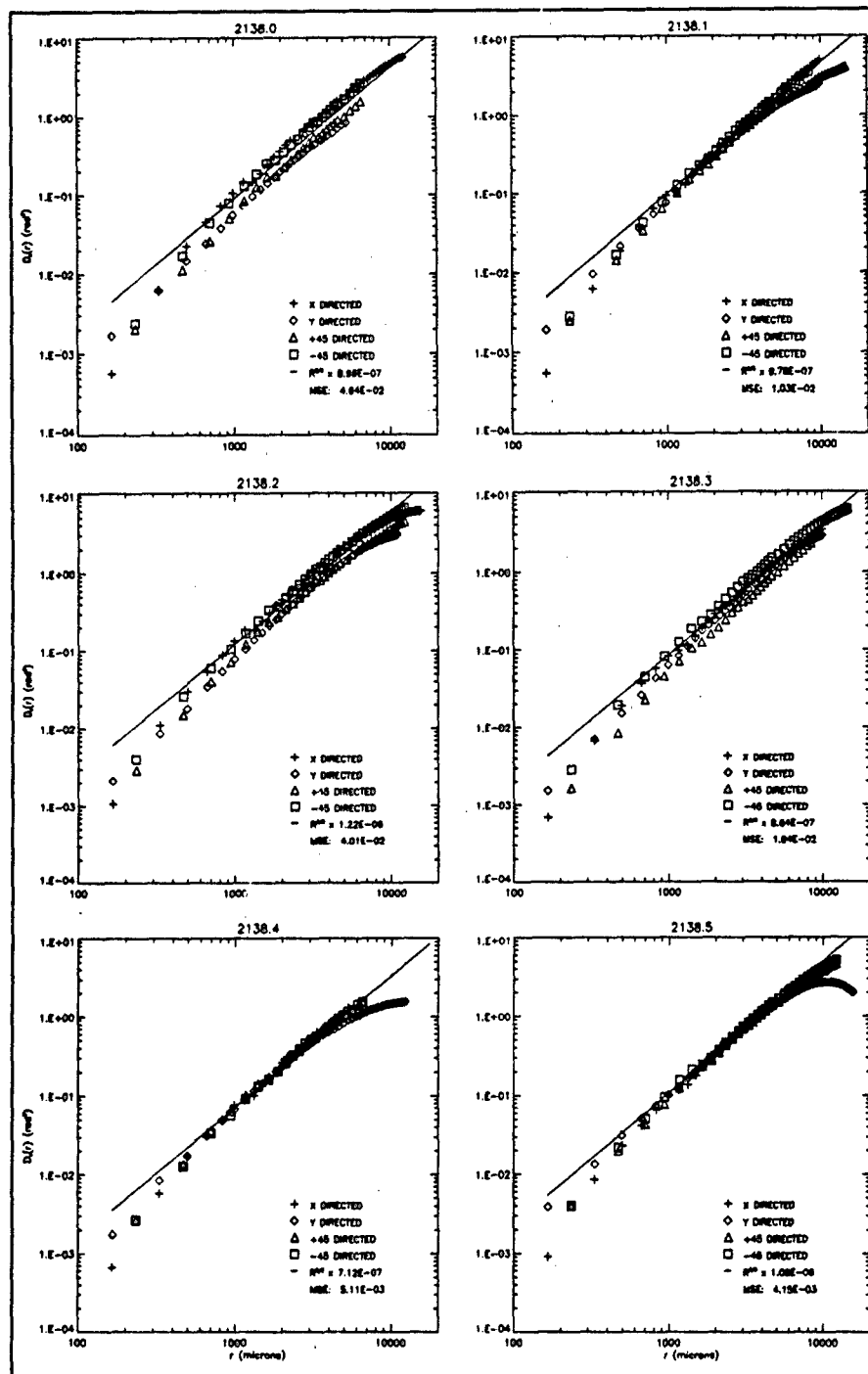


Figure D.41. $\hat{D}_s(r)$ for 2138, locations 0 - 5. The fan voltage is 40 volts; the element voltage is 61 volts; there is one screen in the chamber; the average temperature is 42° C.

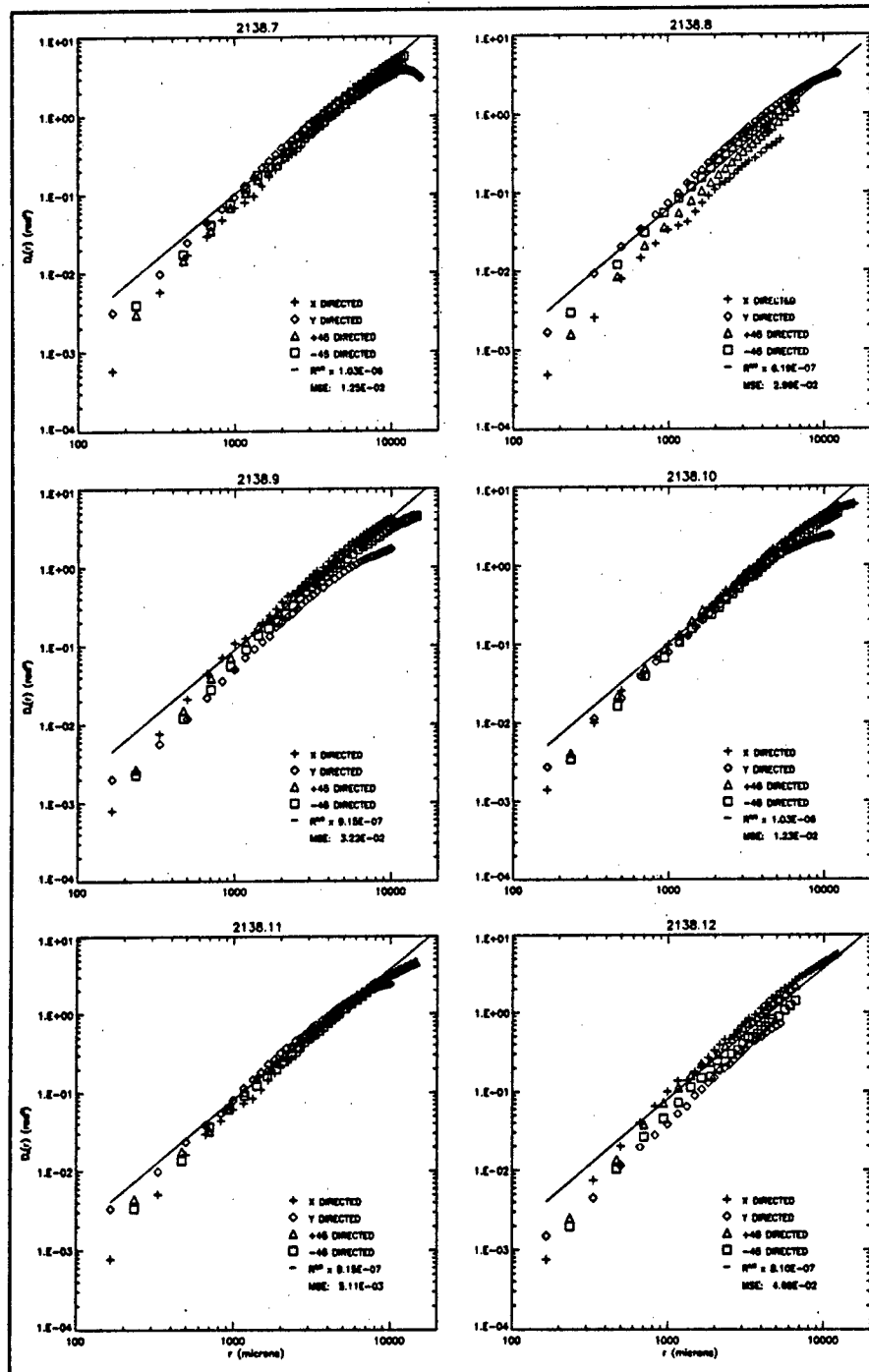


Figure D.42. $\hat{D}_s(r)$ for 2138, locations 7 - 12. The fan voltage is 40 volts; the element voltage is 61 volts; there is one screen in the chamber; the average temperature is 42° C.

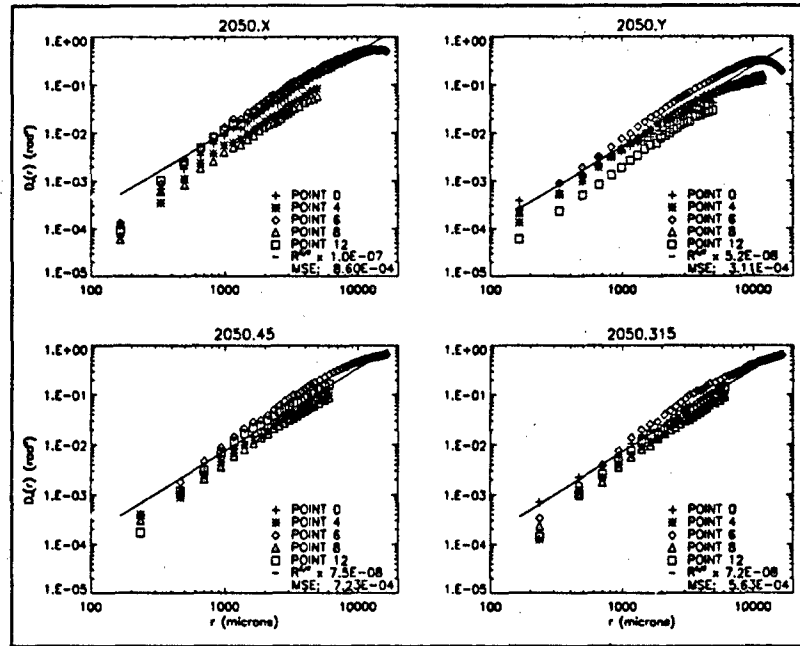


Figure D.43. $\hat{D}_s(r)$ for 2050. The fan voltage is 20 volts; the element voltage is 50 volts; there is no screen in the chamber; the average temperature is 35° C.

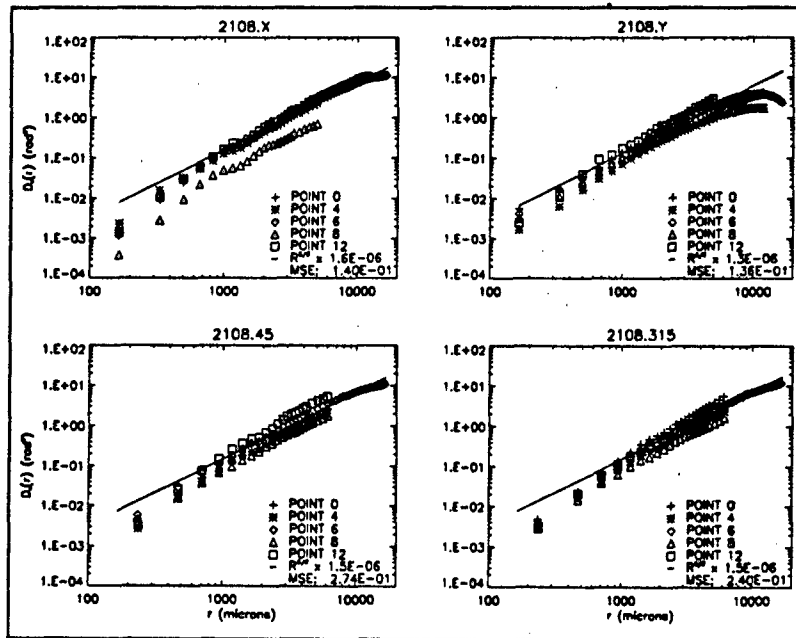


Figure D.44. $\hat{D}_s(r)$ for 2108. The fan voltage is 20 volts; the element voltage is 80 volts; there is no screen in the chamber; the average temperature is 73° C.

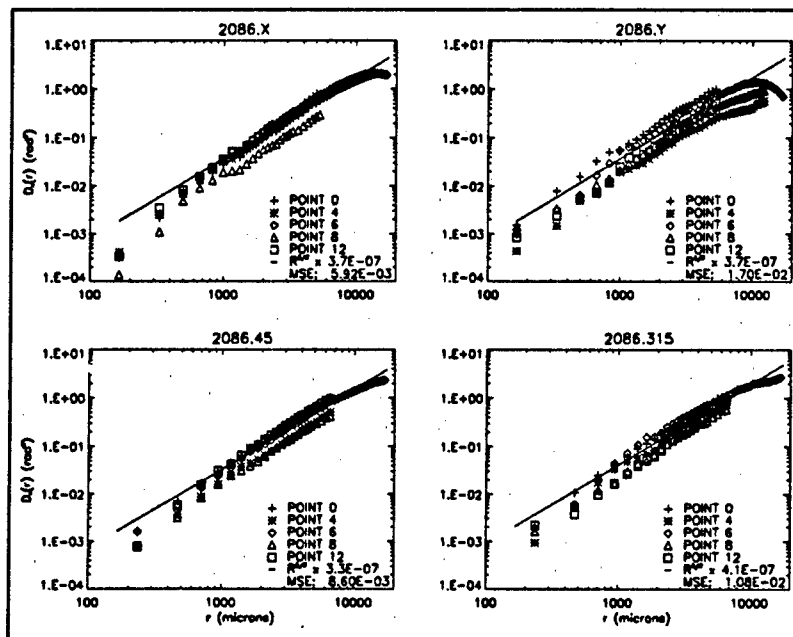


Figure D.45. $\hat{D}_s(r)$ for 2086. The fan voltage is 20 volts; the element voltage is 35 volts; there is one screen in the chamber; the average temperature is 32° C.

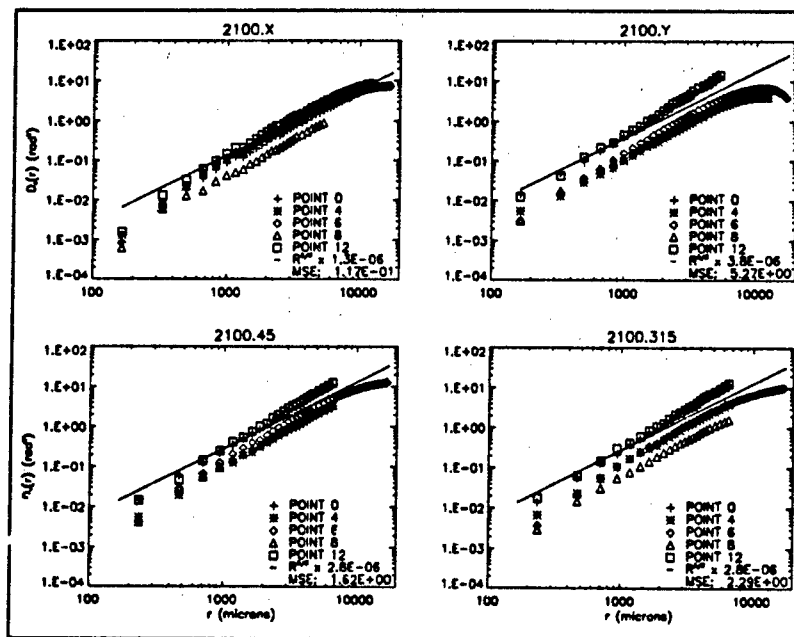


Figure D.46. $\hat{D}_s(r)$ for 2100. The fan voltage is 20 volts; the element voltage is 65 volts; there is one screen in the chamber; the average temperature is 60° C.

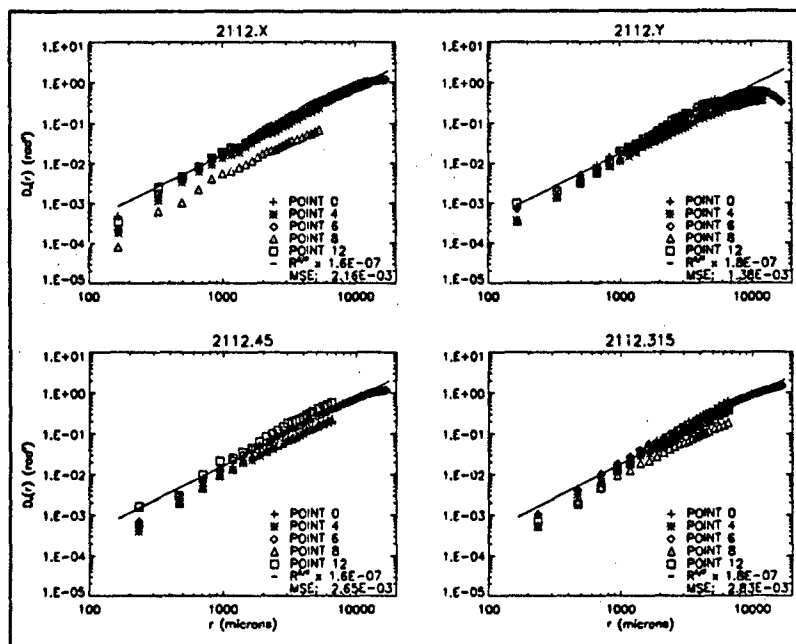


Figure D.47. $\hat{D}_s(r)$ for 2112. The fan voltage is 35 volts; the element voltage is 50 volts; there is no screen in the chamber; the average temperature is 35° C.

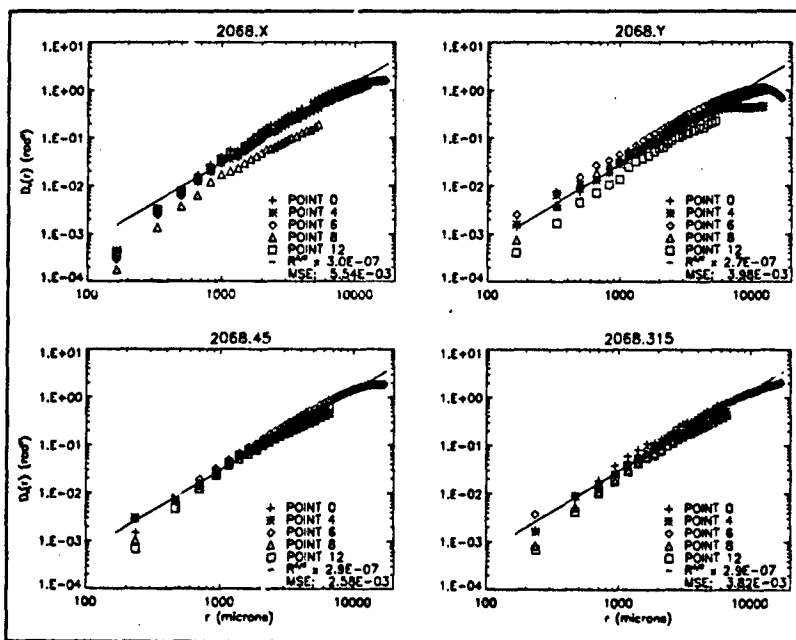


Figure D.48. $\hat{D}_s(r)$ for 2068. The fan voltage is 35 volts; the element voltage is 65 volts; there is no screen in the chamber; the average temperature is 44° C.

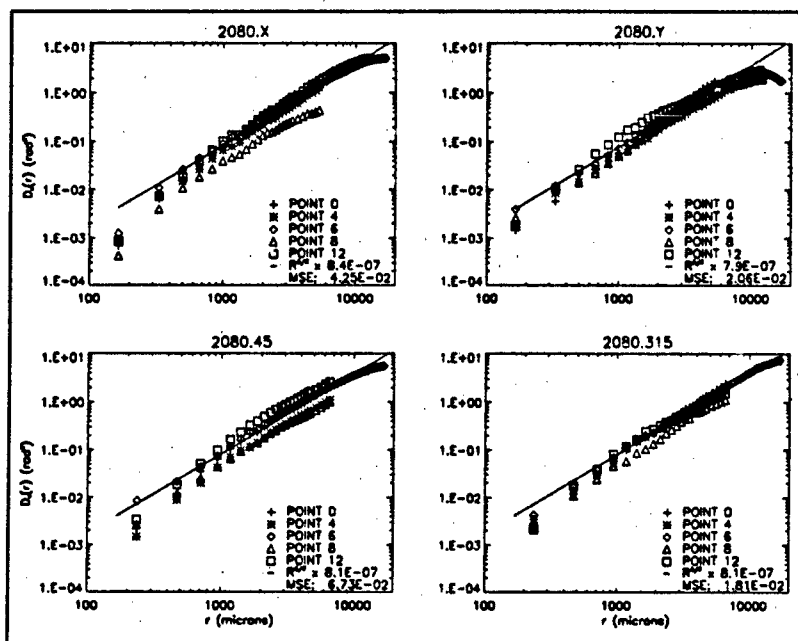


Figure D.49. $\hat{D}_s(r)$ for 2080. The fan voltage is 35 volts; the element voltage is 80 volts; there is no screen in the chamber; the average temperature is 56° C.

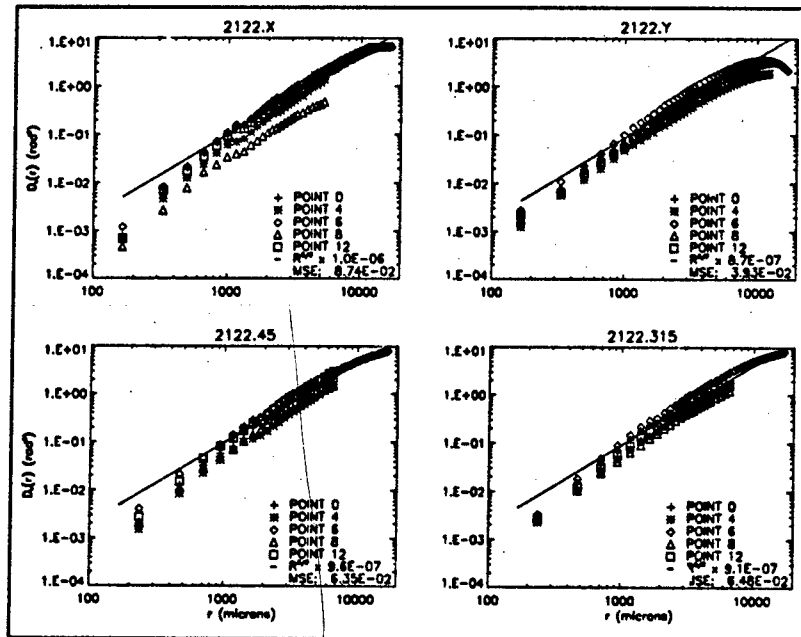


Figure D.50. $\hat{D}_s(r)$ for 2122. The fan voltage is 24 volts; the element voltage is 53 volts; there is one screen in the chamber; the average temperature is 42° C.

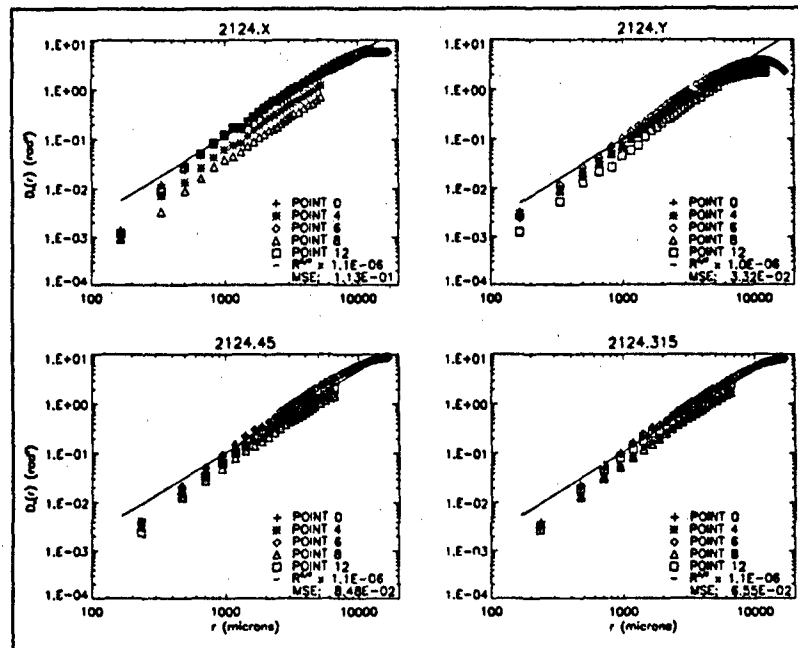


Figure D.51. $\hat{D}_s(r)$ for 2124. The fan voltage is 28 volts; the element voltage is 55 volts; there is one screen in the chamber; the average temperature is 42° C.

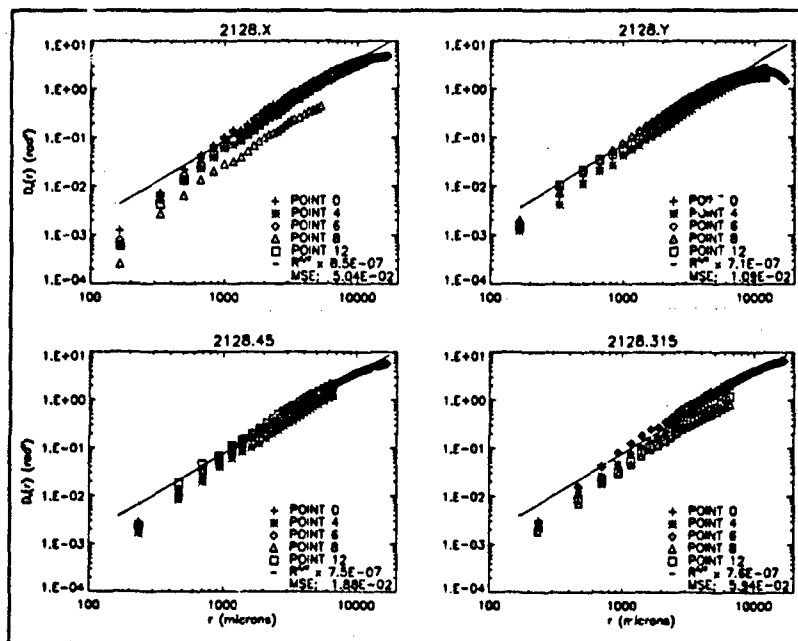


Figure D.52. $\hat{D}_s(r)$ for 2128. The fan voltage is 32 volts; the element voltage is 58 volts; there is one screen in the chamber; the average temperature is 42° C.

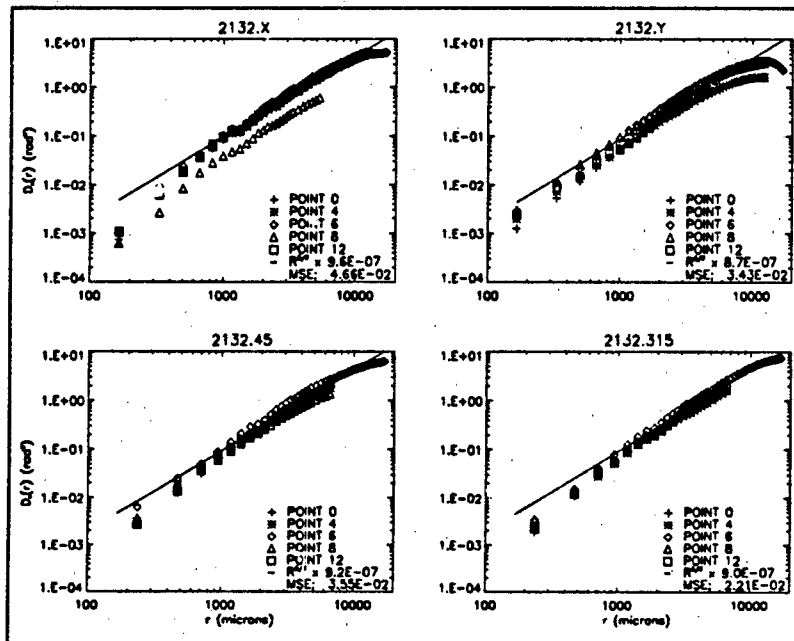


Figure D.53. $\hat{D}_s(r)$ for 2132. The fan voltage is 36 volts; the element voltage is 60 volts; there is one screen in the chamber; the average temperature is 42° C.

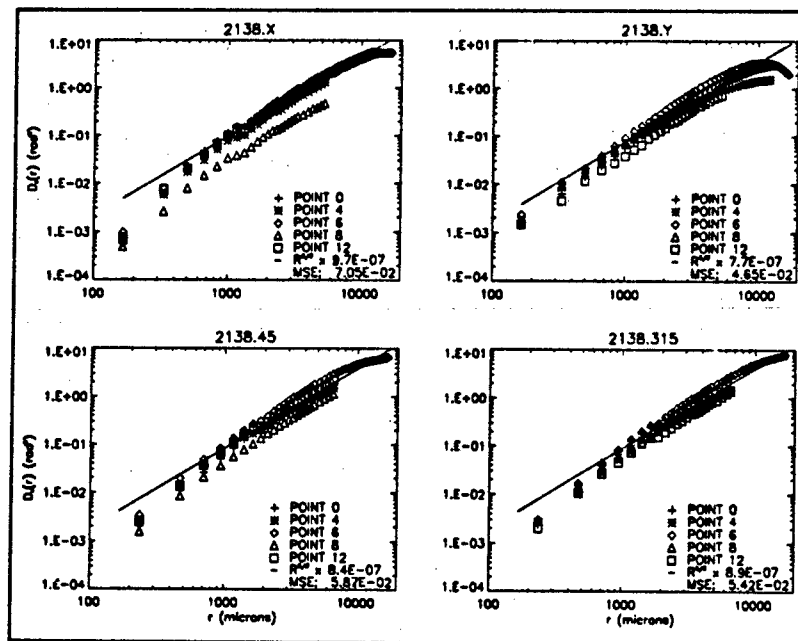


Figure D.54. $\hat{D}_s(r)$ for 2138. The fan voltage is 40 volts; the element voltage is 61 volts; there is one screen in the chamber; the average temperature is 42° C.

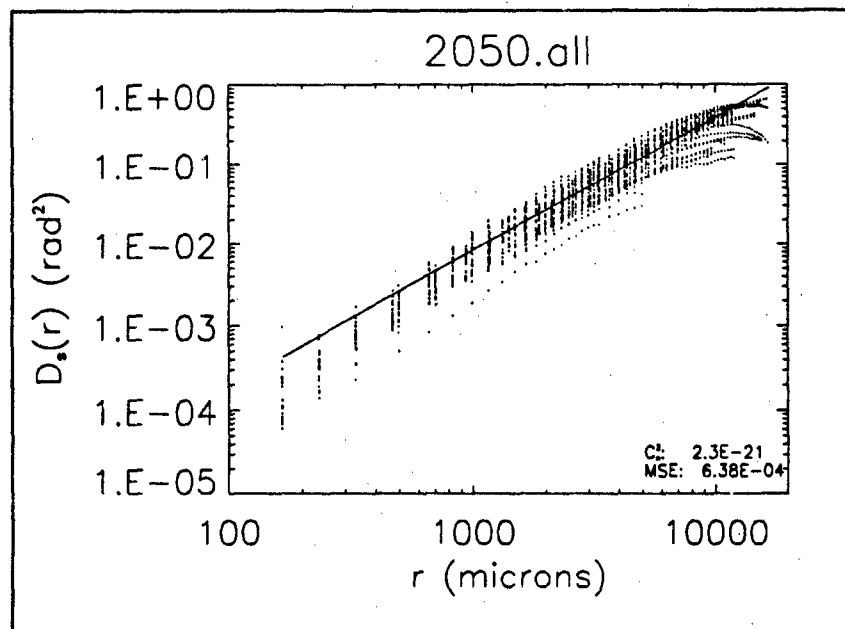


Figure D.55. $\hat{D}_s(r)$ for 2050. The fan voltage is 20 volts; the element voltage is 50 volts; there is no screen in the chamber; the average temperature is 35° C.

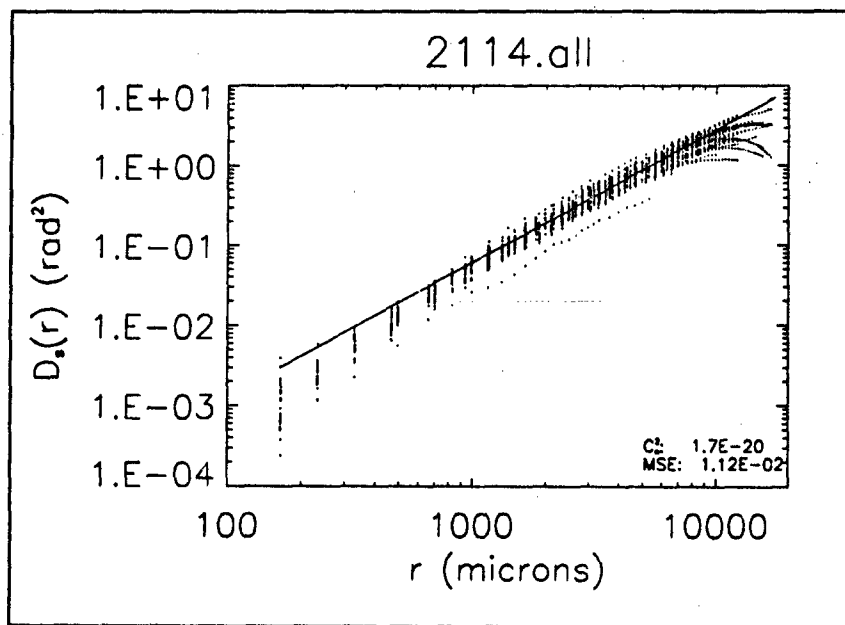


Figure D.56. $\hat{D}_s(r)$ for 2114. The fan voltage is 20 volts; the element voltage is 65 volts; there is no screen in the chamber; the average temperature is 49° C.

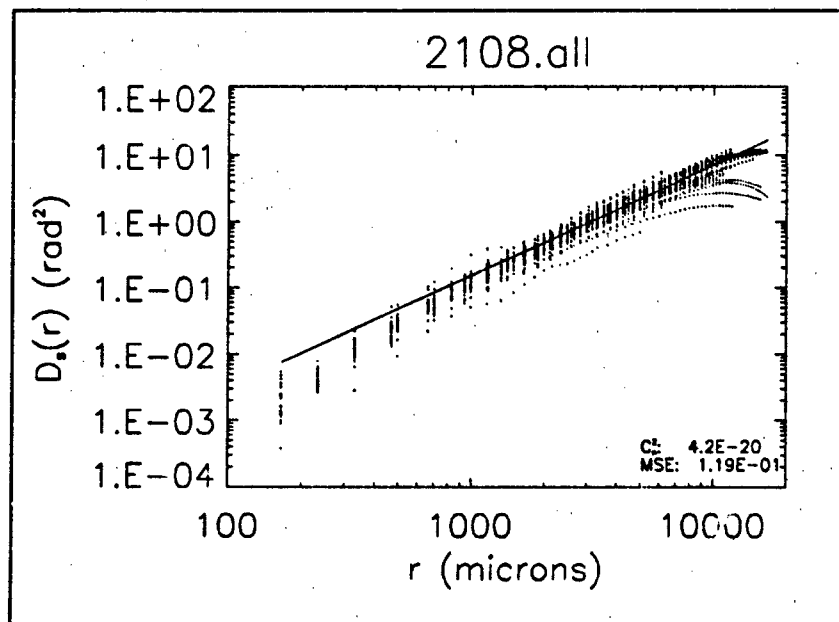


Figure D.57. $\hat{D}_s(r)$ for 2108. The fan voltage is 20 volts; the element voltage is 80 volts; there is no screen in the chamber; the average temperature is 73° C.

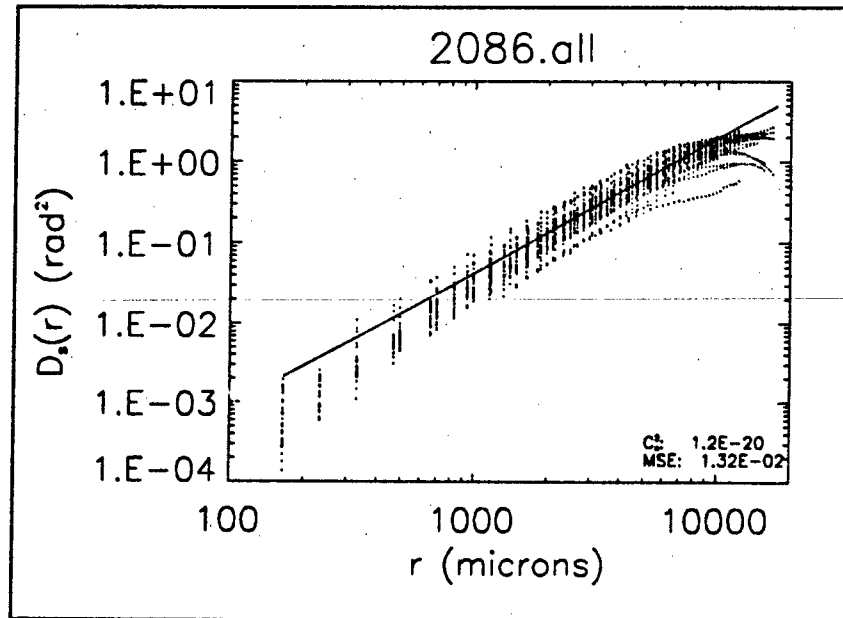


Figure D.58. $\hat{D}_s(r)$ for 2086. The fan voltage is 20 volts; the element voltage is 35 volts; there is one screen in the chamber; the average temperature is 32° C.

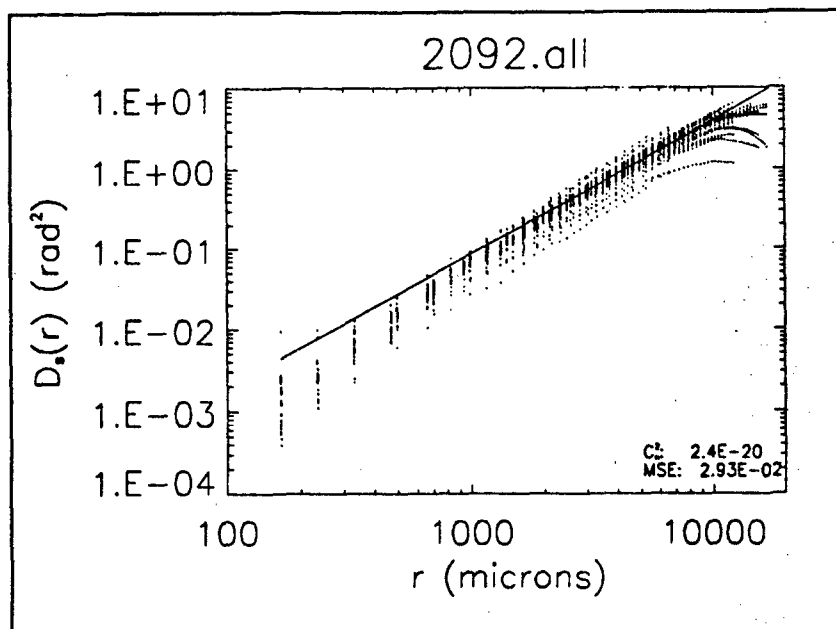


Figure D.59. $\hat{D}_s(r)$ for 2092. The fan voltage is 20 volts; the element voltage is 50 volts; there is one screen in the chamber; the average temperature is 42° C.

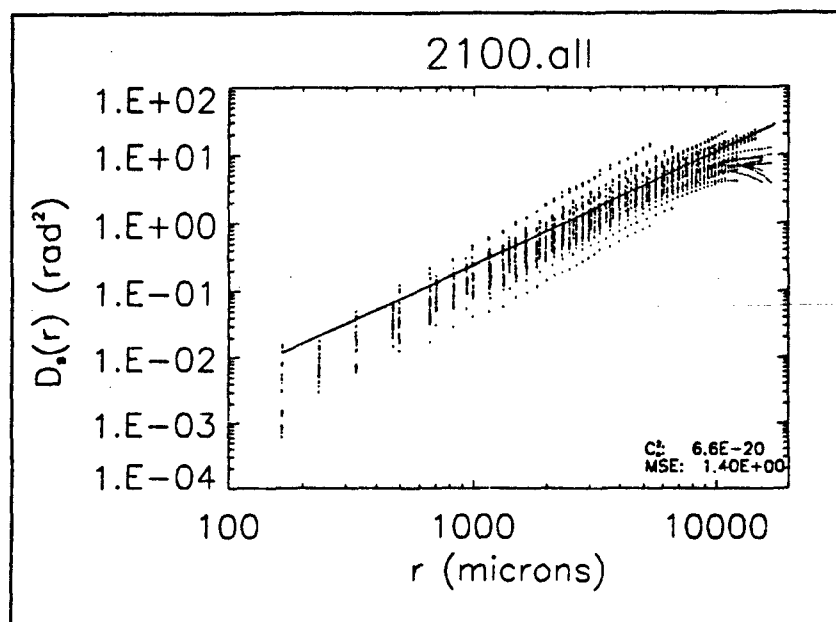


Figure D.60. $\hat{D}_s(r)$ for 2100. The fan voltage is 20 volts; the element voltage is 65 volts; there is one screen in the chamber; the average temperature is 60° C.

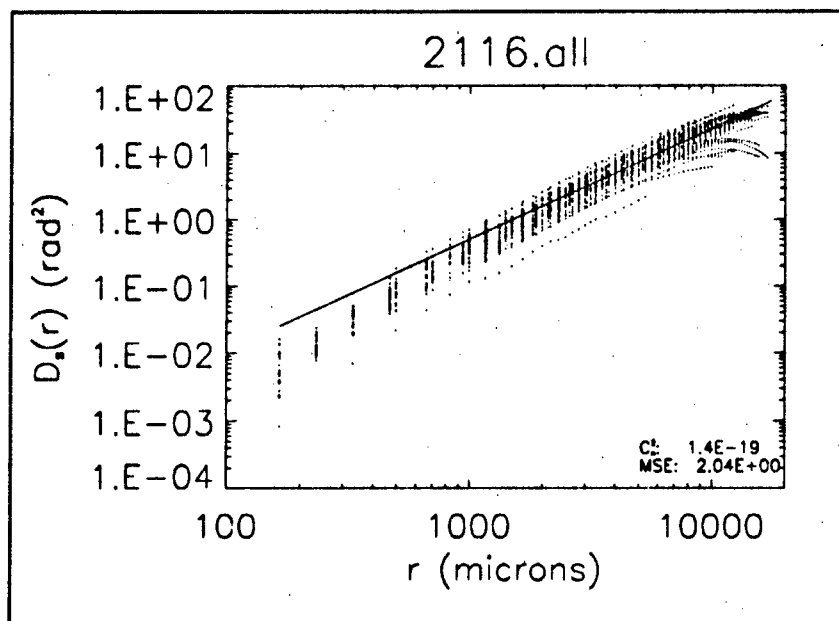


Figure D.61. $\hat{D}_s(r)$ for 2116. The fan voltage is 20 volts; the element voltage is 80 volts; there is one screen in the chamber; the average temperature is 83° C.

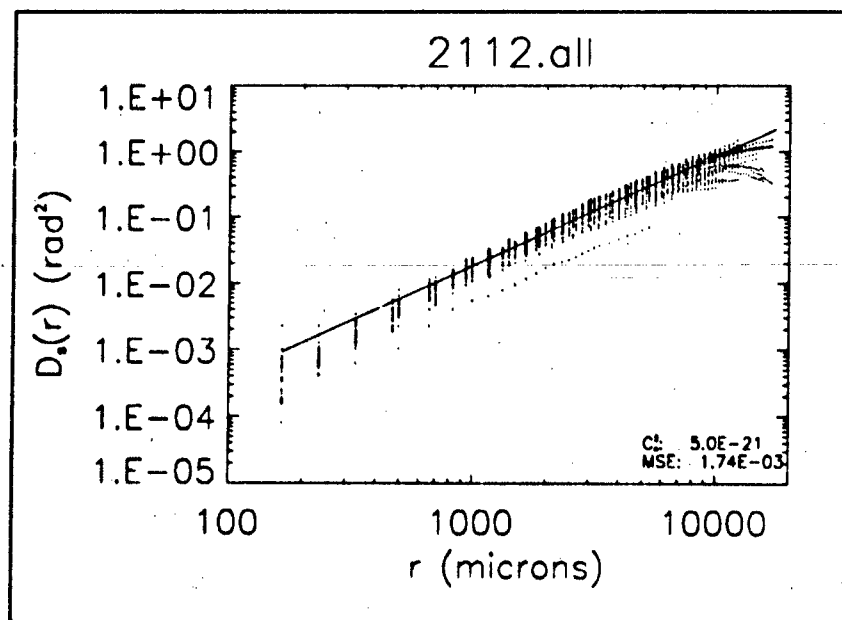


Figure D.62. $\hat{D}_s(r)$ for 2112. The fan voltage is 35 volts; the element voltage is 50 volts; there is no screen in the chamber; the average temperature is 35° C.

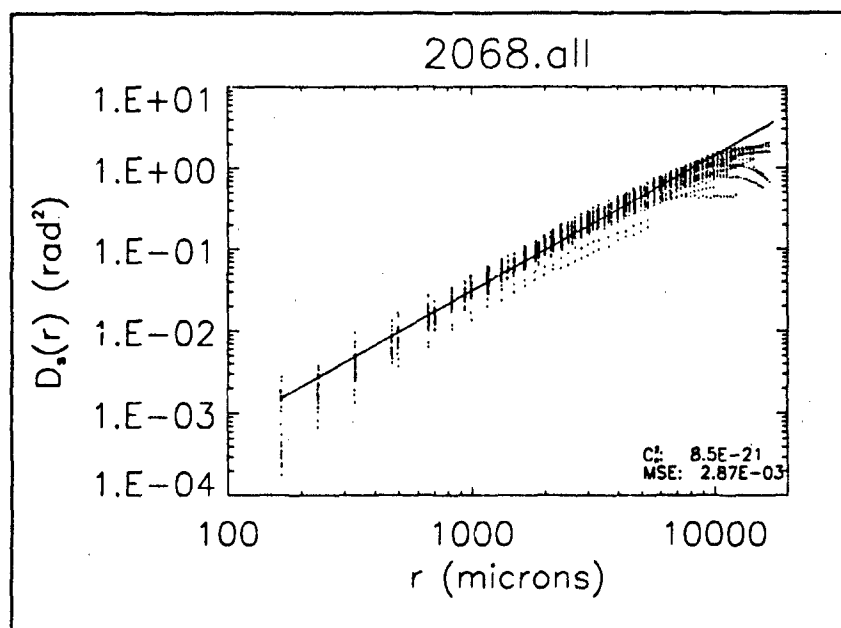


Figure D.63. $\hat{D}_s(r)$ for 2068. The fan voltage is 35 volts; the element voltage is 65 volts; there is no screen in the chamber; the average temperature is 44° C.

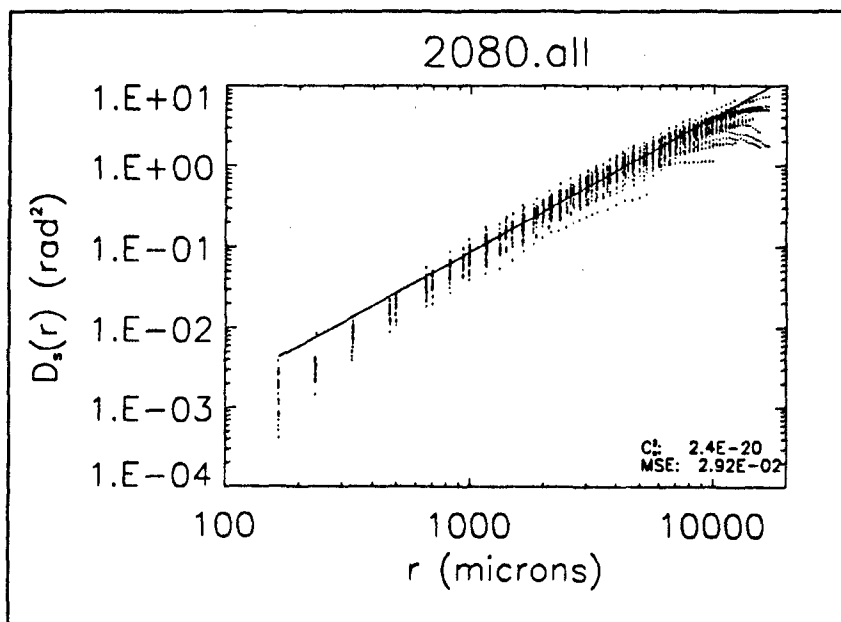


Figure D.64. $\hat{D}_s(r)$ for 2080. The fan voltage is 35 volts; the element voltage is 80 volts; there is no screen in the chamber; the average temperature is 56° C.

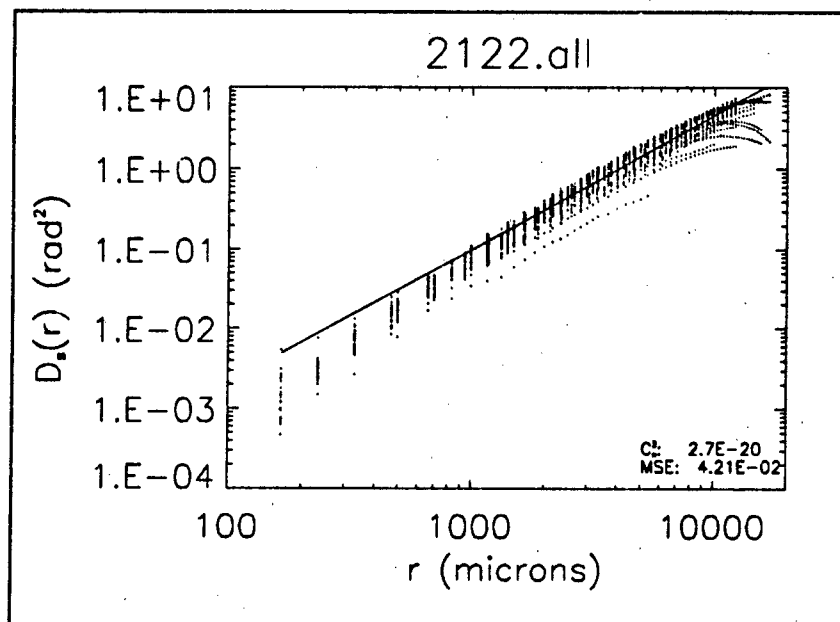


Figure D.65. $\hat{D}_s(r)$ for 2121. The fan voltage is 24 volts; the element voltage is 53 volts; there is one screen in the chamber; the average temperature is 42° C.

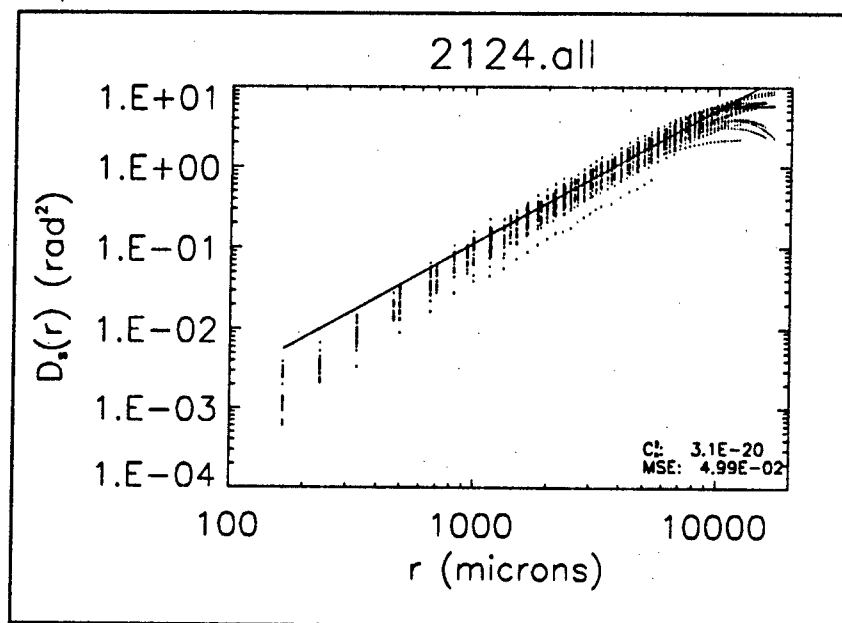


Figure D.66. $\hat{D}_s(r)$ for 2124. The fan voltage is 28 volts; the element voltage is 55 volts; there is one screen in the chamber; the average temperature is 42° C.

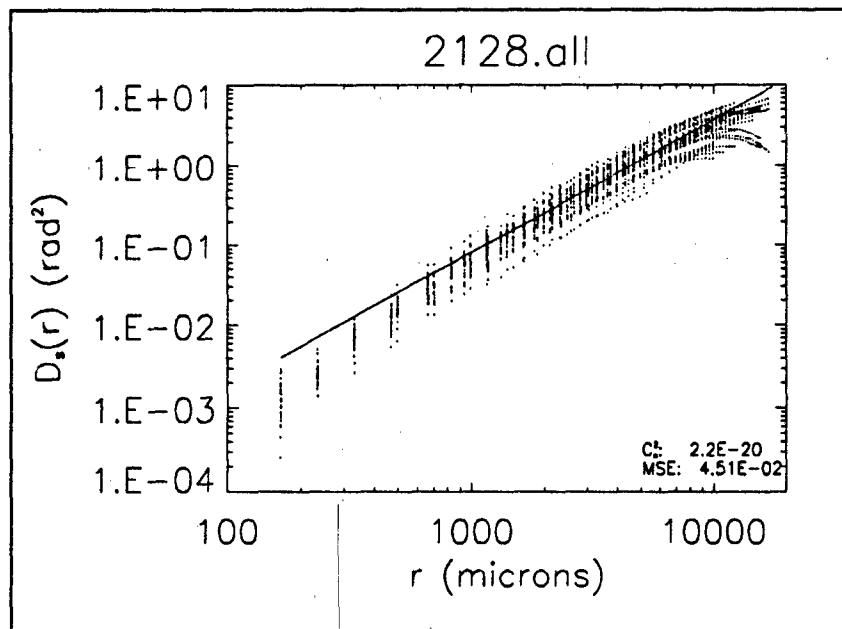


Figure D.67. $\hat{D}_s(r)$ for 2128. The fan voltage is 32 volts; the element voltage is 58 volts; there is one screen in the chamber; the average temperature is 42° C.

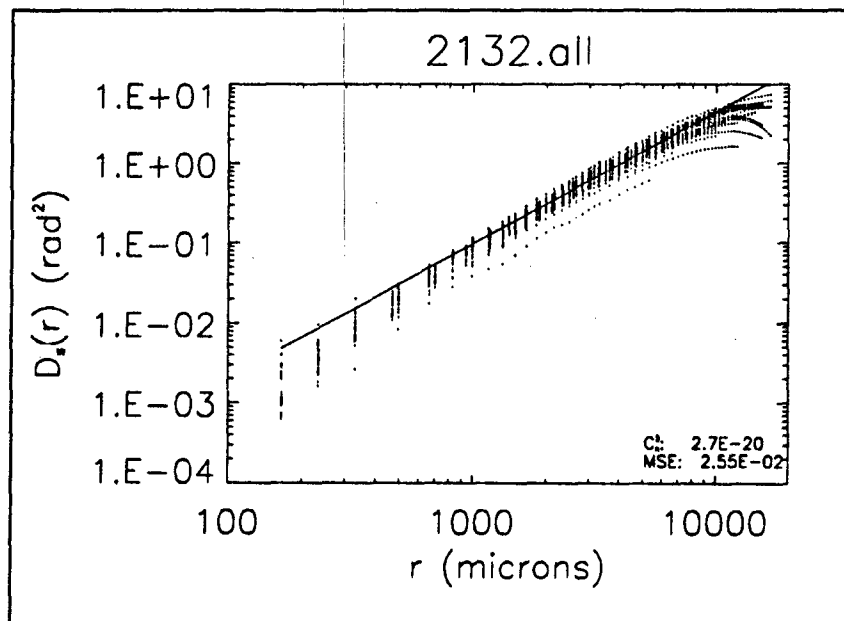


Figure D.68. $\hat{D}_s(r)$ for 2132. The fan voltage is 36 volts; the element voltage is 60 volts; there is one screen in the chamber; the average temperature is 42° C.

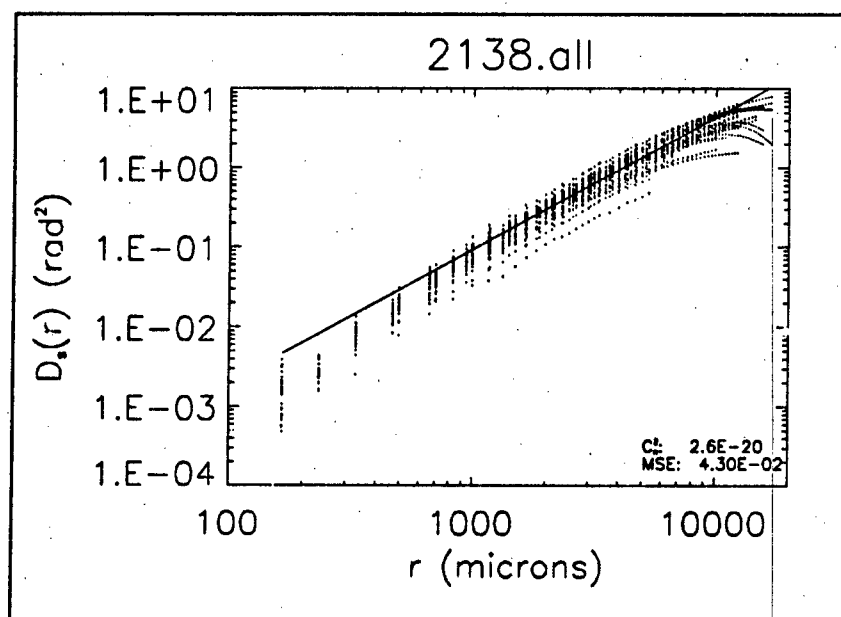


Figure D.69. $\hat{D}_s(r)$ for 2138. The fan voltage is 40 volts; the element voltage is 61 volts; there is one screen in the chamber; the average temperature is 42° C.

Bibliography

1. Ayers, G. R., et al. "Knox-Thompson and triple-correlation imaging through atmospheric turbulence," *J. Opt. Soc. Am. A*, 5:963-985 (1988).
2. Babcock, H. W. "Adaptive optics revisited," *Science* (July 1990).
3. Beavers, W. and others. "Speckle Imaging through the Atmosphere," *The Lincoln Laboratory journal*, 2:207-228 (Summer 1989).
4. Ben-Yosef, N. and E. Goldner. "Sample size influence on optical scintillation analysis. 1: Analytical treatment of higher-order irradiance moments," *Appl. Opt.*, 27:2167-2171 (1988).
5. Bernier, Robert and Arsenault Henri H. "Deconvolution of two-dimensional images with zeros in the transfer function," *Appl. Opt.*, 30:5163-5168 (1991).
6. Bertolotti, M., et al. "Influence of thermal turbulence in a convective ascending stream on phase fluctuations of a laser beam," *Appl. Opt.*, 8:1111-1114 (1969).
7. Bissonnette, L. R. "Atmospheric scintillation of optical and infrared waves: a laboratory simulation," *Appl. Opt.*, 16:2242-2251 (1977).
8. Born, Max and Emil Wolf. *Principles of Optics* (Fourth Edition). New York: Pergamon Press, 1970.
9. Bryngdahl, O. "Applications of Shearing Interferometry." *Progress in Optics 4*, edited by E. Wolf, chapter 2, Amsterdam: North Holland, 1965.
10. Carnevale, M., et al. "Influence of laboratory generated turbulence on phase fluctuations of a laser beam," *Appl. Opt.*, 7:1121-1123 (1968).
11. Duda, R. O. and P. E. Hart. *Pattern Classification and Scene Analysis*. New York: John Wiley & Sons, 1973.
12. Fried, D. L. "Optical resolution through a randomly inhomogeneous medium for very long and very short exposures," *J. Opt. Soc. Am.*, 56:1372-1379 (1966).
13. Fried, D. L. "Least-square fitting a wave front distortion estimate to an array of phase-difference measurements," *J. Opt. Soc. Am.*, 67:370-375 (1977).
14. Gaffard, J. P. and Corinne Boyer. "Adaptive optics for optimization of image resolution," *Appl. Opt.*, 26:3772-3777 (1987).
15. Gamo, H. and A. K. Majumdar. "Atmospheric turbulence chamber for transmission experiment: characterization by thermal method," *Appl. Opt.*, 17:3755-3762 (1978).
16. Gardner, C. S., et al. "Sodium laser guide star technique for adaptive imaging in astronomy." *SPIE proceedings on Active Telescope Systems 1114*. 1989.
17. Gonglewski, J. D., et al. "First astronomical application of postdetection turbulence compensation: images of α Aurigae, ν Ursae Majoris, and α Geminorum using self-referenced speckle holography," *Appl. Opt.*, 29:4527-4529 (1990).
18. Goodman, J. W. *Introduction to Fourier Optics*. New York: McGraw-Hill Book Co., 1968.
19. Goodman, J. W. *Statistical Optics*. New York: John Wiley & Sons, 1985.
20. Hardy, J. H. "Active Optics: A New Technology for the Control of Light," *Proc. IEEE*, 66:651-697 (1978).
21. Hardy, J. H. "Active optics - don't build a telescope without it." *SPIE proceedings on Advanced Technology Optical Telescopes 392*. 252-259. 1982.

22. Hardy, J. W. and others. "Real-Time Atmospheric Compensation," *J. Opt. Soc. Am.*, 67:360-369 (1977).
23. Hardy, John W. and Alan J. MacGovern. "Shearing interferometry: a flexible technique for wavefront measurement." *SPIE proceedings on Interferometric Metrology 816*. 180-195. 1987.
24. Hariharan, P. *Optical Interferometry*. Sydney; Orlando: Academic Press, 1985.
25. Hudgin, R. H. "Optimal wave front estimation," *J. Opt. Soc. Am.*, 67:378-382 (1977).
26. Hudgin, R. H. "Wave front reconstruction for compensated imaging," *J. Opt. Soc. Am.*, 67:375-377 (1977).
27. Hufnagel, Robert E. "Propagation through atmospheric turbulence." *The Infrared Handbook* edited by William L. Wolfe and George J. Zissis, chapter 6, Washington, DC: U.S. Government Printing Office, 1978.
28. Korff, D. "Analysis of a method for obtaining near-diffraction-limited information in the presence of atmospheric turbulence," *J. Opt. Soc. Am.*, 69:971-980 (1973).
29. Labeyrie, A. "Attainment of diffraction-limited resolution in large telescopes by Fourier analyzing speckle patterns in star images," *Astron. Astrophys.*, 6:85-87 (1970).
30. Lee, R. W. and J. C. Harp. "Weak scattering in random media, with applications to remote probing," *Proc. IEEE*, 57:375-406 (1969).
31. Lohmann, A. W., et al. "Speckle masking in astronomy: triple correlation theory and applications," *Appl. Opt.*, 22:4028-4037 (1983).
32. Lohmann, A. W. and B. Wirnitzer. "Triple correlations," *Proc. IEEE*, 72:889-901 (1984).
33. Majumdar, A. K. and H. Gamo. " C_n^2 measurements in a laboratory generated turbulence by thermal and optical methods." *A digest of technical papers presented at the Topical Meeting on Optical Propagation Through Turbulence, Rain, and Fog*. August 1977. Sponsored by the Optical Society of America.
34. Majumdar, A. K. and H. Gamo. "Statistical measurements of irradiance fluctuations of a multipass laser beam propagated through laboratory-simulated atmospheric turbulence," *Appl. Opt.*, 21:2229-2235 (1982).
35. McGlamery, B. L. "Restoration of Turbulence-Degraded Images," *J. Opt. Soc. Am.*, 57:293-297 (1967).
36. Merkle, F. "Adaptive optics," *Physics World* (January 1991).
37. Murty, M. V. R. K. "Lateral Shearing Interferometers." *Optical Shop Testing* edited by D. Malacara, chapter 4, 105-148, New York: John Wiley & Sons, 1978.
38. Parenti, R. R. "Recent Advances in Adaptive Optics Methods and Technology," *SPIE Vol. 1000—Laser Wavefront Control*, 101-109 (1988).
39. Pearson, J. E., et al. "Adaptive Optical Techniques for Wave-Front Correction." *Applied Optics and Optical Engineering VII*, edited by R. R. Shannon and J. C. Wyant, New York: Academic Press, 1979.
40. Primot, J., et al. "Deconvolution from wave-front sensing: a new technique for compensating turbulence-degraded images," *J. Opt. Soc. Am. A*, 7:1589-1608 (1990).
41. Rimmer, M. P. "Method for evaluating lateral shearing interferograms," *Appl. Opt.*, 13:623-629 (1974).
42. Roddier, F. "Triple correlation as a phase closure technique," *Opt. Comm.*, 60:145-148 (1986).

43. Roehrig, J. and M. Okamura P. Ehrensberger. "High speed, large format wavefront sensor employing hexflash phase analysis." *SPIE proceedings on Fringe Pattern Analysis* 1163. 44-50. 1989.
44. Steel, W. H. *Interferometry* (Second Edition). Cambridge: Cambridge University Press, 1983.
45. Tatarski, V. I. *Wave Propagation in a Turbulent Medium*. New York: McGraw-Hill, 1961.
46. Tyler, G. A. and others. *Adaptive Optics Technology and Atmospheric Turbulence Correction, volume I: Technical Descriptions*. Contract F2960182C0104, Placentia, California: The Optical Sciences Company, 1988 (AD-B121063).
47. Weigelt, G. "Speckle imaging and speckle spectroscopy," *SPIE Proc.*, 1130:148-151 (1989).

Vita

Eric Parker Magee received a Bachelor of Science degree in Engineering from Grove City College, Grove City, Pennsylvania, May 1987. Upon graduation, he was commissioned as a lieutenant in the United States Air Force Reserve. After being ordered to active duty in January 1988, he was assigned as an avionics engineer with the Avionics Engineering Directorate, Aeronautical Systems Division, Air Force Systems Command, Wright Patterson Base, Ohio. In June 1991 he began a Master of Science degree in Electrical Engineering at the Air Force Institute of Technology, Wright-Patterson Air Force Base, Ohio. Captain Magee is a member of the Eta Kappa Nu and Tau Beta Pi Engineering Honor Societies.

Permanent address: 50 Warden Street
Union City, PA 16438

VITA-1